The Dissertation Committee for Scott Daniel Sifferman
certifies that this is the approved version of the following dissertation:

Mid-Infrared Type-I Diode Laser Design using Molecular Beam Epitaxy

Committee:

Seth R. Bank, Supervisor

Mikhail A. Belkin

Yaguo Wang

Daniel M. Wasserman

Edward T. Yu

Mid-Infrared Type-I Diode Laser Design using Molecular Beam Epitaxy

by

Scott Daniel Sifferman

Dissertation

Presented to the Faculty of the Graduate School of
The University of Texas at Austin
in Partial Fulfillment
of the Requirements
for the Degree of

Doctor of Philosophy

The University of Texas at Austin
August 2020

This work is dedicated to

my wife and children,

for their love, support, and patience.

Acknowledgments

A great deal of time, effort, patience, and struggle goes into any large undertaking. Moreover it is only with help and support of others that a work such as this one can get over the finish line. Thank you to all who guided, helped, collaborated, and sacrificed along the way.

Professor Seth Bank provided the means for this work to happen. I am grateful to him for allowing me the space and time to work my way through this research. I have appreciate his guidance and direction, especially when I have run into problems or issues that seem insurmountable in the moment. His continued belief in my ability to finish this work has bolstered my confidence in myself as I get ready to move to the next adventure in my career.

Thank you to Professors Mikhail Belkin, Yaguo Wang, Dan Wasserman, and Edward Yu for serving as my dissertation committee. I especially appreciate their responsiveness and availability during this spring and summer now that virtual interactions are the new normal.

I want to give many thanks to the members of the LASE research group. There would be no way to keep the MBEs, Bravo and Echo, operating without their help. I especially want to acknowledge Hari Nair for laying the groundwork and foundation of my research work before me; Erica (Krivoy) Davis for getting me oriented and started within the group, and for her friendship to me and my family since then; Rodolfo Salas for his friendship and collaboration throughout our time together at UT and afterward; Scott Maddox for his MBE insights and techniques that made repeatable and reliable growth so much easier; Kyle McNicholas for his partnership

through the years with maintaining the lab and developing creative ways to repair the MBEs in glovebags to avoid system bakes; Andrew Briggs for his help with device fabrication and process development; and Stephen March for his tireless efforts in the lab and for his help keeping Bravo running. Thank you also to our amazing group admin Christine Wood for making sure all the i's are dotted and t's are crossed, that funding and tuition goes through, and for being all around awesome.

I was fortunate to get to work with other great researchers at the Microelectronics Research Center. Thank you especially to Tanuj Trivedi, Praveen Pasupathy, Seungyong Jung, Leland Nordin, and Sukrith Dev for many productive (and often late-night) conversations, helpful advice, and fruitful interactions I have had with each of you.

I would like to thank each of the MER staff, in particular Joyce Kokes for always pushing that last-minute source material PO through; Jeannie Toll for her help with REU and general university problem solving; James Hitzfelder for giving me the machine shop key with minimal sarcasm and fuss; Jesse James for letting me bug him with late night texts when a tool was acting up; Ricardo Garcia for keeping the cleanroom organized and running; and Jonny Johnson for training me on many tools, his friendly smile, and gracious presence. I am grateful to Terry Mattord for letting me pick his brain for help with diagnosing, debugging, and troubleshooting all things MBE and vacuum-system related.

I also want to acknowledge the contributions and impact of my collaborators on this work: Professor Robert Kudrawiec's group for all of the photoreflectance measurements and analysis; Professor Larry Lee's group for their TEM and ECCI studies; and Professor Juliet Gopinath and Dr. Kenneth Underwood for their work on Auger effects in highly-strained materials.

Thank you to my parents for believing in me, providing opportunities to learn and flourish, and for providing help along the way to allow me to continue my research work.

To my children, thank you for the respite and escape you provided me from the grind of the lab while we read stories, rode bikes, played at the pool, or went to the Thinkery. I have enjoyed watching you grow and learn and start your own schooling while I have been finishing mine.

To my wife, whose sacrifice and support these last eight years while I completed this work, you are without equal. This has not been an easy time of life, and the decision for me to return to graduate school certainly added to the complications. There is no adequate way to truly express how important your role has been in my life to get to this point. None of this would have been possible without your support and effort. I am truly blessed to share this time and our family together with you. Thank you for the love you provide to everyone around you, in particular our children. “Many women have done excellently, but you surpass them all.” (Proverbs 31:29)

Mid-Infrared Type-I Diode Laser Design using Molecular Beam Epitaxy

Scott Daniel Sifferman, Ph.D.
The University of Texas at Austin, 2020

Supervisor: Seth R. Bank

The mid-infrared region of the electromagnetic spectrum, particularly in the wavelength range between 3 and 5 µm, is important for a number of applications in spectroscopy, gas sensing, infrared countermeasures, and communications. Despite these motivations, mid-infrared laser development has lagged behind that of visible and near-infrared technology. This is in part because semiconductor laser sources, while they exist across the mid-infrared, suffer from one or several drawbacks such as high power consumption, high threshold currents, low characteristic temperatures, limited wallplug efficiency, parasitic non-radiative recombination processes, or reduced carrier confinement. The latter impediment, specifically reduced carrier confinement of holes, is endemic to the active regions of GaSb-based type-I quantum-well diode lasers as the optical emission wavelength is extended past 3 µm.

In this work, we present our efforts toward enhancing mid-infrared active regions to extend the emission wavelength of type-I emitters. Through the use of highly-strained, high indium-content quantum wells we demonstrate type-I diode laser operation from aluminum-free active regions up to 3.62 µm, and photoluminescence emission from type-I quantum wells out past 4 µm. Additional studies focused on the effect of using bismuth during the growth of these materials. While

increased compressive strain in the quantum well alloy enables greater hole confinement at longer emission wavelengths, it also leads to material roughening and defect formation that restrict the number of and thickness of strained regions that can be grown before material quality irreparably degrades. We observed that by using bismuth as a surfactant during the growth of highly-strained GaIn(As)Sb alloys, material degradation was suppressed as these materials were grown well beyond classical critical thickness limits. We were also able to leverage the epitaxial growth conditions used for highly-strained, high indium-content quantum wells to incorporate dilute amounts of bismuth, up to 3%, into the quantum well materials. The addition of bismuth to the quantum well alloys modifies the valence band to provide additional hole confinement, leading to brighter emitters with up to 34% higher peak intensity. It also resulted in overall lower materials strain without reducing the emission wavelength or performance. This opens a promising approach to overcome strain-related limitations to laser performance and emission wavelength, allowing for device designs with increased numbers of quantum wells and potentially reducing the effects of gain saturation.

An additional path toward improved mid-infrared devices is to switch the quantum well barrier material from GaSb to a lattice-matched AlGaAsSb alloy. This is the same strategy employed for many other mid-infrared type-I diode lasers, albeit for emission wavelengths less than 3.1 µm. By changing the barrier alloy, the quantum well valence band offset is increased, providing stronger hole confinement. Coupling these barriers with the highly-strained, high indium-content quantum wells results in a 3× improvement in peak photoluminescence and a >30% reduction in emission linewidth for quantum wells operating up to 4.2 µm. Using this coupled approach, we propose a laser diode device designed to operate at 4.1 µm.

Table of Contents

List of Figures

Chapter 1

Introduction

The mid-infrared spectrum (2 to 10 μm) is important for applications ranging from science and technology to security and industrial needs. This region contains a large number of fundamental rotational and vibrational chemical resonances that are important for applications such as medical diagnostics, environmental monitoring, and industrial process control, making this region crucial for spectroscopic, atmospheric, and environmental studies [1]. Figure 1.1 depicts the absorption bands for several of these molecules, including methane (3.3 μm), carbon dioxide (4.2 μm), and carbon monoxide (4.6 μm). The absorption strength at the fundamental resonances can be several orders of magnitude higher than at overtones in the near-infrared [2], [3], allowing for more sensitive detection of trace amounts of gas or chemicals [4]–[6]. The absorption peaks are also less crowded in the mid-infrared compared to their near-infrared and visible overtones, allowing for selective spectroscopic detection of a large number of molecules. Lastly, an atmospheric transmission window between 3.5 and 4 μm, highlighted in Figure 1.2, can be utilized for applications such as free-space optical communications, military countermeasures, and remote explosive detection. These applications demand compact, high-efficiency, room temperature-operable laser sources.

Unfortunately there is a general dearth of photonic materials, devices, and light sources to effectively utilize the mid-infrared. The development of visible and near-infrared laser sources has resulted in a very mature technology, yet the mid-

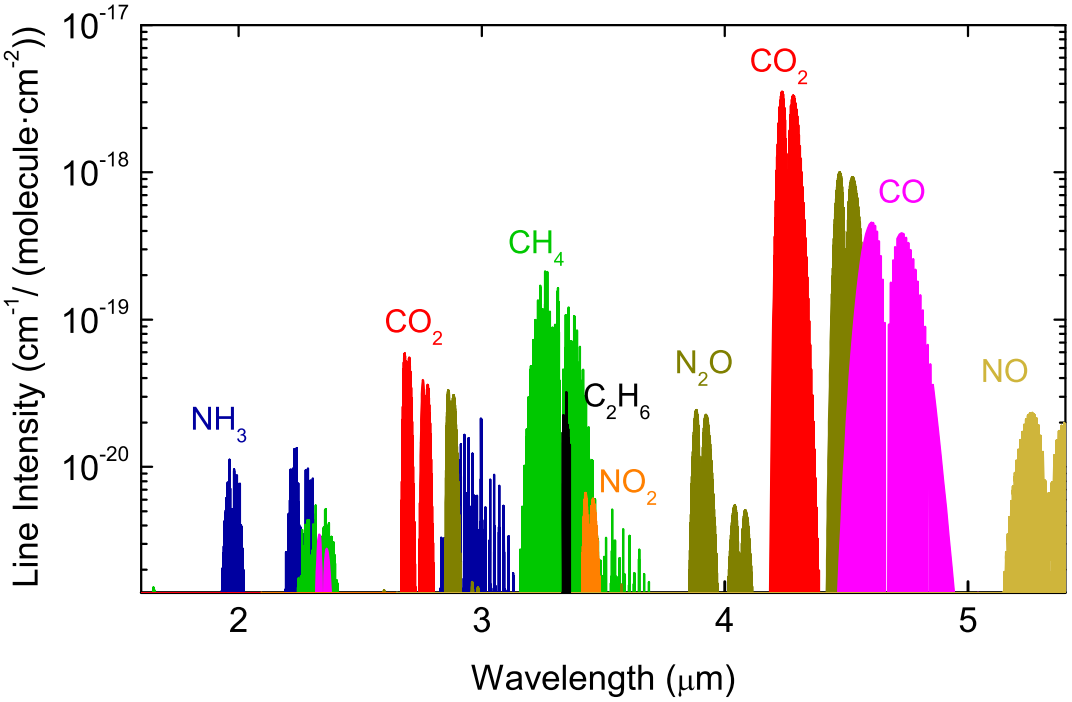

Figure 1.1: Absorption bands for selected gas molecules between 2 and 5 μm from the HITRAN2016 molecular spectroscopic database [3].

infrared region suffers from a relative lack of similar progress. Fundamental physical limitations make such technological advances difficult. Multi-phonon relaxation limits the transparency of many materials in the mid-infrared and is a major source of loss for both lasers and other photonic devices. The comparably small energy gap between the upper and lower laser levels in mid-infrared materials also means that the laser transition is more susceptible to being bypassed by non-radiative emission through multi-phonon relaxation. Materials that do offer low phonon energies and suitable transparencies also often have poor mechanical strength, chemical stability, and thermal conductivity. Additionally, there is a lack of suitable gain media with high quantum efficiency for lasers. These limitations become more pronounced as

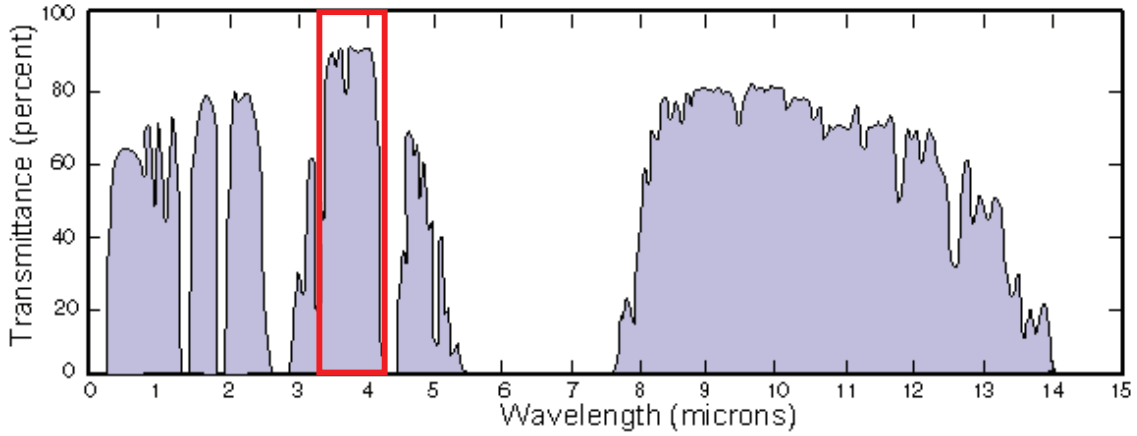

Figure 1.2: Atmospheric transmission measured over a 1 nautical mile path at sea level with the atmospheric transmission window between 3.5 and 4 μm highlighted, adapted from [7].

the laser emission wavelength is increased. They include decreased optical mode confinement in the active region, leading to increased optical mode overlap with cladding layers; increased Auger recombination in the active region associated with either resonant transitions between valance bands or resulting from mismatched electron and hole effective masses; increased free carrier absorption (FCA) both in the active region and cladding layers; and reduced electron mass making confinement energy of the active regions a larger component of total transition energy and reducing differential gain. These difficulties are inherently coupled to the laser material properties so advances in mid-infrared laser performance will be linked to either novel device architectures which can tune material properties in a favorable manner or advances in materials available for laser active regions.

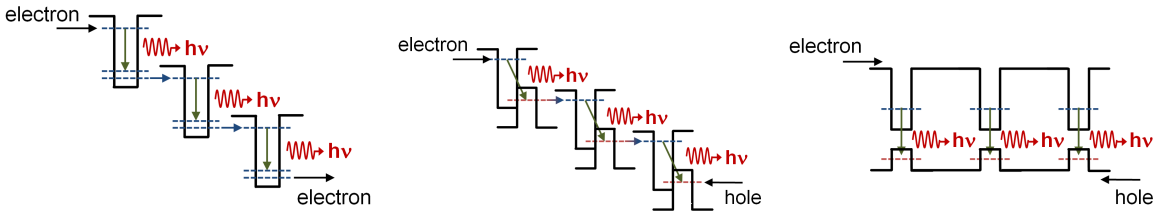

(a) (b) (c)

Figure 1.3: Simplified band diagrams of mid-infrared semiconductor laser active region architectures: (a) quantum cascade laser; (b) interband cascade laser; (c) type-I diode laser

1.1 Semiconductor laser architectures

Mid-infrared semiconductor laser sources can be broadly divided into three main architecture designs: (1) intersubband quantum cascade lasers (QCLs), (2) interband cascade lasers (ICLs), typically with type-II active regions, and (3) diode lasers, typically with type-I active regions. Basic band diagrams for each approach are illustrated in Figure 1.3. State-of-the-art performance data of devices operating at room temperature between 2 and 5 µm are summarized in Figure 1.4 for each class. The next several sections give a brief overview of the design, advantages, and drawbacks of these different approaches to semiconductor mid-infrared laser device design.

1.1.1 Quantum cascade lasers

The first QCL was reported in 1994 and emitted at 4.2 µm [30]. QCLs have been demonstrated with high output powers, tunability, and continuous wave (CW) operation above room temperature [31]–[38]. Two features of QCLs differentiate them from interband devices. First, the emission wavelength is set via the device structure design, the composition and spacing of the quantum well (QW) layers and barriers, but not by the material band gap as with interband devices [39]. This al-

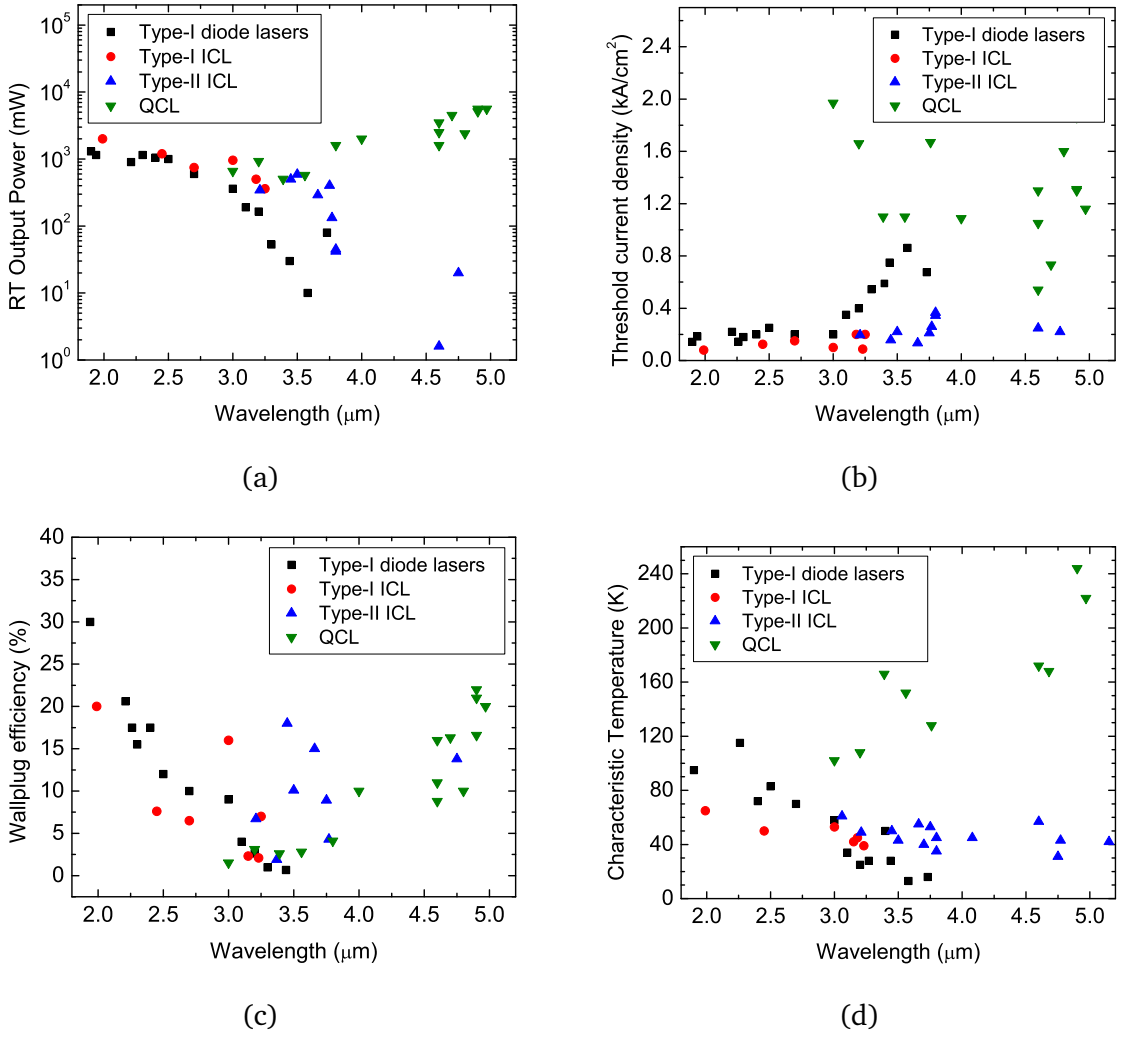

Figure 1.4: State-of-the-art performance of mid-infrared semiconductor lasers versus lasing wavelength at room temperature for (a) output power, (b) threshold current density, (c) wallplug efficiency, and (d) characteristic temperature of threshold current (adapted from [8]. Additional data from [9]–[29]).

lows for QCL fabrication in well-developed substrate systems such as InP and GaAs. The second feature is that QCLs are unipolar devices, with electrons being the only involved carrier. This allows each injected electron to undergo multiple lasing transitions in multiple cascades of QWs, resulting in high output powers (5.1 W CW, 120

W pulsed) and wallplug efficiencies (53% at 40 K, 21% at room temperature) [33], [40], [41]. These devices also demonstrate good threshold current temperature stability as they are immune to Auger recombination effects due to their intersubband design. QCLs do suffer from much higher power consumption at threshold as a result of short upper state lifetimes, which potentially limits their utility in portable applications.

1.1.2 Interband cascade lasers

Interband cascade lasers were first proposed in 1994 by Yang et al. [42], and soon after were demonstrated with both type-I and type-II active regions [43]. Type-II device development and performance advanced faster due to the reduced Auger recombination rates arising from the spatial separation of electrons and holes in the staggered type-II band alignments [44]. ICLs also adapt well to cascaded designs like QCLs, although employing band-to-band optical transitions instead of intraband transitions [45]–[47]. Recent progress of these devices has led to more robust devices. As recent as 2004 CW ICLs were limited to cryogenic operation [48], but now operate at room temperature over much of the 3–5 µm range [47], [49]–[53]. However, device performance and stability over operating temperature continues to be mediocre, with relatively low characteristic temperatures of threshold current, T_0, indicative of significant Auger recombination effects at long wavelengths.

1.1.3 Type-I diode lasers

Type-I diode lasers grown on GaSb exhibit high powers with high wall plug efficiencies up to $\sim$3 µm, [54]–[58]. Threshold current densities at room temperature are even comparable to near-infrared devices [55], [57], [59]–[62]. As the emission

wavelength of type-I diode lasers is increased past 3 µm, however, several obstacles arise that limit the development of efficient, reliable sources. These include Auger recombination due to insufficient spin-orbit splitting, FCA, and shrinking valence band offsets. Both Auger recombination [63], [64] and FCA [65], [66], primarily by holes, become much more pronounced at longer wavelengths, hampering efficient mid-infrared type-I diode laser sources. However, the more direct challenge that has hindered device development at longer wavelengths is that the typical GaInAsSb QW alloy begins to have a very low valence band offset to the barrier material, usually AlGaAsSb, as the alloy composition is configured for longer wavelength emission. Thus hole confinement in the QW region is diminished, which allows barrier states to become populated and reduces internal efficiency. These problems have limited output power and power efficiency, increased threshold currents, and reduced the characteristic temperature of threshold current for diode lasers operating beyond 3 µm. Type-I lasers operating with AlGaAsSb barriers are reported up to 3.1 µm [67]. For longer wavelengths, indium is added to the barrier alloy to form AlGaInAsSb. The quinary barrier material has been employed to extend the operation wavelength of type-I diode lasers from 3 µm out to 3.73 µm [68], [69].

1.2 Organization of dissertation

In the following chapters, we will present on our work toward developing mid-infrared materials for type-I QW diode lasers and discuss several paths toward future devices operating at wavelengths up to and beyond 4 µm. Chapter 2 will review methods and techniques to grow, characterize, and test the materials and devices studied in this dissertation. Chapters 3, 4, and 5 will present the research results of this dissertation.

Chapter 3 summarizes our work toward mid-infrared diode lasers reaching longer emission wavelengths using highly-strained quantum wells. The growth of highly-strained materials and the inherent challenges will be reviewed. Our development of highly-strained, high-indium containing mid-infrared alloys has opened up the potential for laser active region design to wavelengths beyond 4 µm. Quantum well diode lasers with GaSb barriers and operating at 210 K emitted at 3.62 µm, a record long wavelength for laser devices with an aluminum-free active region. By adding aluminum to the active region/waveguide, room-temperature type-I emission can be extended further, to 4.2 µm. We present our design for a proposed future laser device structure operating at 4.1 µm.

Chapters 4 and 5 present our work on the use of bismuth during the growth of laser active regions to improve the optical quality of highly-strained materials. In Chapter 4, we discuss bismuth used as a surfactant species to augment the growth and quality of highly-strained materials, namely how bismuth used during growth allows us to improve the optical quality of strained materials grown beyond classical critical thickness limitations. Chapter 5 will cover our work on adding bismuth to our mid-infrared quantum well alloys and the results of these dilute bismide materials. Lastly, this dissertation will conclude with a look forward to future work in these materials for further improvements in mid-infrared laser operation and performance.

Chapter 2

Epitaxial Growth and Characterization of III-V Semiconductors

This chapter describes the primary tool used in this dissertation, namely molecular beam epitaxy (MBE), as well as characterization methods used to investigate the properties of the semiconductor materials studied. The next section gives a brief overview of MBE, with emphasis on specific aspects pertinent to epitaxial growth of the materials discussed in this dissertation. Following that are descriptions of several of the principal characterization methods used to perform analysis on those materials.

2.1 Molecular beam epitaxy

Molecular beam epitaxy (MBE) was developed by Arthur and Cho at Bell Laboratories in the late 1960s and early 1970s [70], [71]. It was originally used to study the interaction of gallium and arsenic molecular beams incident on a heated GaAs substrate [72]. This was followed by epitaxial growth demonstrated via molecular beams for GaAs, GaP, and GaAsP [73]. The development of the room-temperature operating GaAs/AlGaAs semiconductor laser led to great interest in III-V compound semiconductors. These had been originally grown using liquid phase epitaxy, but MBE soon proved to be the preferred choice.

MBE is an ultra-high-vacuum (UHV) crystal growing technique that uses epitaxial (layer-by-layer) deposition to make compound materials with great precision

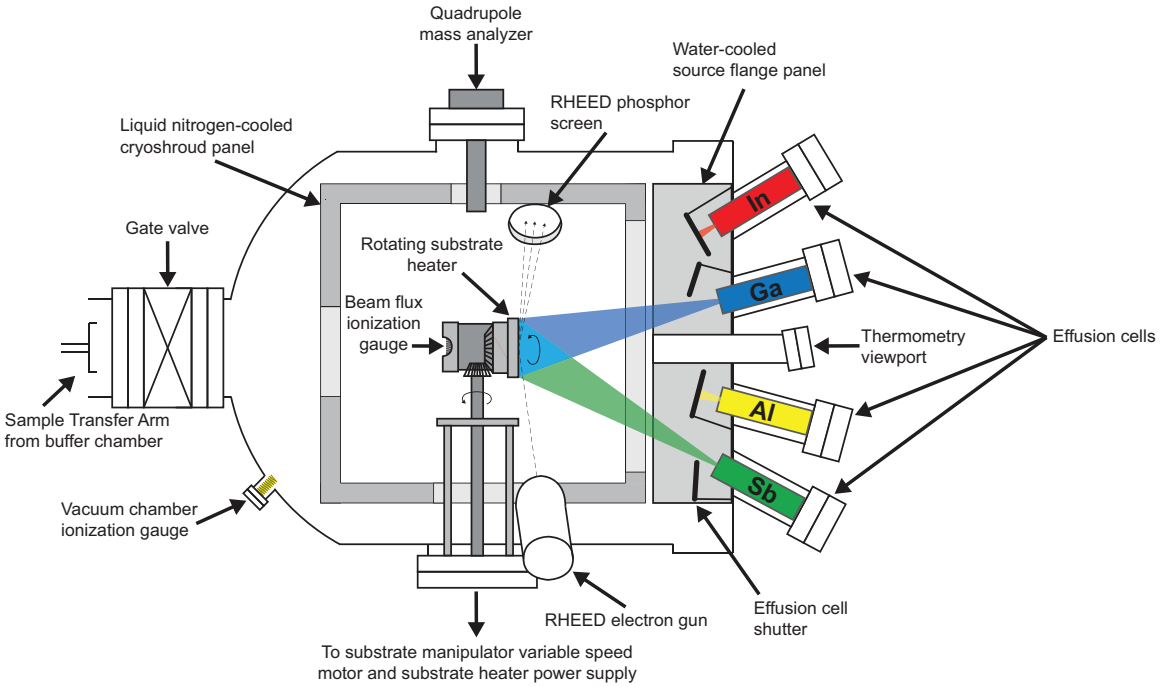

Figure 2.1: Schematic cross-section representation of a Gen. II molecular beam epitaxy system with various components annotated.

and purity. MBE can produce high-quality layers with very abrupt interfaces and good control of thickness, doping, and composition. These materials are layered one on top of the other to form semiconductor devices such as transistors, photodetectors, and lasers. A typical MBE system is kept at a base pressure of 10^{-11} to 10^{-10} Torr. At pressures this low, the mean free path of particles is meters-long. The UHV environment creates a mostly decoupled system for growing compound semiconductors. Figure 2.1 shows a cross-sectional top view of a typical MBE growth chamber, with key components annotated. Not depicted in this image are the associated vacuum pumps, such as turbomolecular pumps and cryo pumps, that connect to the chamber and are used to create and maintain the UHV environment.

Samples grown by MBE are mounted onto a heated substrate manipulator within the vacuum chamber. The substrate manipulator is surrounded by a liquid nitrogen-cooled cryoshroud panel. Residual gases within the MBE chamber that come into contact with the cryoshroud adsorb onto its surface. This helps to locally reduce the background concentration of these residual gases in the vicinity of the substrate manipulator. The substrate manipulator is equipped with gearing to allow for sample rotation, which helps promote sample uniformity during growth. During growth, the substrate manipulator is oriented toward a set of quasi-Knudsen cells containing ultra-pure source material (typical purities >99.9999%) heated until the material evaporates or sublimates. The cells are arrayed around a cylindrical flange and tilted to aim at the substrate manipulator. The resultant elemental or molecular beams from the heated source material are directed out of the cell toward a heated seed crystal substrate, where the beams overlap. The substrate provides a crystalline template for ordered epitaxial growth of layers composed of the incident material beams. The substrate temperature is controlled in order to promote or inhibit surface migration and desorption of the impinging atoms before they find energetically favorable lattice sites to incorporate. Individual pneumatically-actuated shutters are placed in front of each cell and are used to either block or pass the molecular beam toward the substrate. The actuators are computer-controlled for precision shuttering timing, allowing for abrupt heterointerfaces and well-controlled alloy compositions and thicknesses. The growth rate and composition of epitaxial layers is also governed by the flux of the molecular beams, which is a function of the temperature of the source material. PID control loops maintain stable cell temperatures and fluxes during operation for controlled, repeatable growth. The flux can be inferred from calibrated measurements of the beam equivalent pressure (BEP) using a retractable

beam flux ionization gauge on the opposite side of the substrate manipulator. This gauge can be rotated into the path of the molecular beams to sample the BEPs from the associated cells prior to growth. The growth rate of III-V semiconductor materials grown by MBE is typically $\sim$1 µm/hour.

The MBE system is composed of three vacuum chambers with their associated vacuum pumps and telemetry electronics. The three chambers are the previously-described growth chamber, the load lock, and the buffer or transition chamber. Samples are introduced into and removed from the vacuum environment through the load lock. The load lock on the system used for this dissertation is pumped on by a turbomolecular pump backed by a tri-scroll dry pump. Following whenever the load lock is vented and opened to atmosphere, the chamber and its contents must be baked using a heater lamp while under vacuum provided by the turbomolecular pump. This bake acts to remove water and volatile materials such as oils or organics that entered the chamber when vacuum integrity was broken.

The buffer chamber is used for sample preparation prior to growth and sample storage. The buffer of the MBE system used in this dissertation is also equipped with an atomic hydrogen cleaning station; however this component was not utilized in the present research. The buffer chamber on this system also acts as a transition tube to a second MBE system, allowing in-vacuum sample transfer between systems.

All samples presented in this dissertation were grown using a Varian Gen II solid source molecular beam epitaxy system. Dual-zone thermal effusion cells supplied gallium, indium, and bismuth. Aluminum was also supplied by a thermal effusion cell that was operated in cold lip mode to limit aluminum creep in the pBN crucible. Dimeric arsenic and antimony were supplied by dual-zone valved cracker cells. As_4 and Sb_4 are sublimated from bulk source charges. A heated conductance

zone thermally "cracks" the tetramers into more reactive As_2 and Sb_2 molecules for growth. A valve controls the exit aperture and hence the molecular flux. The valve position can be changed with much faster timing than the cell temperatures, allowing for better precision control of the resultant V flux. Dopants beryllium and gallium telluride were supplied from tilted crucible cells designed to operate out of deep-lying upward-looking ports below the MBE source flange.

2.1.1 Group-III limited growth

Upon arriving at the growth surface, incident atoms and molecules can adsorb, migrate about the surface, interact with other atoms, incorporate into the growing film, or desorb. Typical III-V materials grown via MBE are grown in what is termed the "group-III limited" regime. The group-III species (Al, Ga, In) have a unity or near-unity sticking coefficient, meaning that nearly every atom that reaches the substrate surface will incorporate into the growing film. Conversely, the group-V species (including As, Sb, Bi) are much more volatile, with non-unity sticking coefficients at typical MBE growth temperatures. As such, the group-Vs must be supplied in excess to prevent the growth surface of the epitaxial films from becoming group-III rich and forming metallic droplets. Excess group-V atoms that do not incorporate into the growing film will desorb, and ultimately be pumped out of the growth chamber. Thus the growth rate of the films is set by the flux of group-III materials incident on the growth surface.

The growth rate and group-III atomic flux are, in fact, proportional to each other, scaled by the number of group-III atoms in the unit cell (4, for zincblende III-V materials) and inversely scaled by the unit cell volume. For homoepitaxy and lattice-matched heteroepitaxy, the volume is the cube of the substrate lattice parameter. For

strained-materials epitaxy, such as the optical emitters presented in this work, the out-of-plane lattice parameter is no longer equal to the in-plane lattice parameter, which is itself equal to the substrate lattice parameter for coherently-strained films. The layer out-of-plane lattice parameter $a_\perp$ is given by

$$a_\perp = a\left(1 - 2\frac{c_{21}}{c_{11}}\left(\frac{a_\parallel}{a} - 1\right)\right) \tag{2.1}$$

where $a_\parallel$ is the substrate lattice parameter, a is the layer bulk lattice parameter and c_{21} and c_{11} are the elastic constants of the layer alloy. With the in-plane lattice parameter, $a_\parallel$, and the out-of-plane lattice constant, $a_\perp$, both measured in angstroms, the group-III atomic flux, J_{III}, as a function of material growth rate is

$$J_{III}\left[\frac{atoms}{nm^2 - s}\right] = \frac{400}{{a_\parallel}^2 a_\perp}\left(GR\left[\frac{\text{Å}}{s}\right]\right) = \frac{200}{{a_\parallel}^2}\left(GR\left[\frac{ML}{s}\right]\right) \tag{2.2}$$

where the growth rate, GR, has units of Å/s or ML/s. The growth rate in Å/s can be converted to monolayers/s by dividing by 2 ML/$a_\perp$.

The group-III alloy composition is easily changed by adjusting the relevant group-III flux ratios. The total group-III atomic flux, J_{tot} is equal to the sum of the individual group-III species fluxes, and the alloy ratios are equal to the flux ratios. Thus

$$J_{tot} = J_A + J_B + J_C + \ldots \tag{2.3}$$

and

$$frac\ A = \frac{J_A}{J_{tot}}; frac\ B = \frac{J_B}{J_{tot}}; frac\ C = \frac{J_C}{J_{tot}}; etc. \tag{2.4}$$

2.1.2 Mixed group-V growth and calibration

Unlike the group-III species, the group-V elements do not have unity sticking coefficients, and therefore must be supplied in excess to maintain stoichiometric growth. For monopnictide semiconductors, such as AlGaAs and GaInAs, this presents little issue. The growth rate is limited by the group-III flux, and the alloy is set by adjusting the relative group-III fluxes. A suitable arsenic overpressure is selected and growth can proceed with little incident. However for mixed-V alloys, such as AlGaAsSb and GaInAsSb, the group-V species compete with one another for available anion vacancies. Complicating matters, III-As bonds are more energetically favorable than III-Sb bonds leading to an exchange reaction of As for Sb that occurs near the growth surface, making alloy compositions sensitive to the group-V flux ratio, substrate temperature, and growth rate [74], [75].

For the low growth temperatures used for the samples presented in this work, the volatility as well as the adatom mobility of the group-V species is reduced. This results in lower group-V volatility and therefore less group V needs to be supplied to main stoichiometric growth. The V/III flux ratio is also reduced in order to avoid group-V precipitate formation, which results in reduced material optical quality.

One additional growth consideration for the work in this dissertation was the valve backlash of the antimony cell used in this work. As shown in Figure 2.2, there was a consistent repeatable directional dependence on the measured cell flux, varying up to 2.4×. Care was taken when sampling BEPs and planning growth layers to ensure that the direction the valve was to travel (open to close or close to open) was consistent for similar layers.

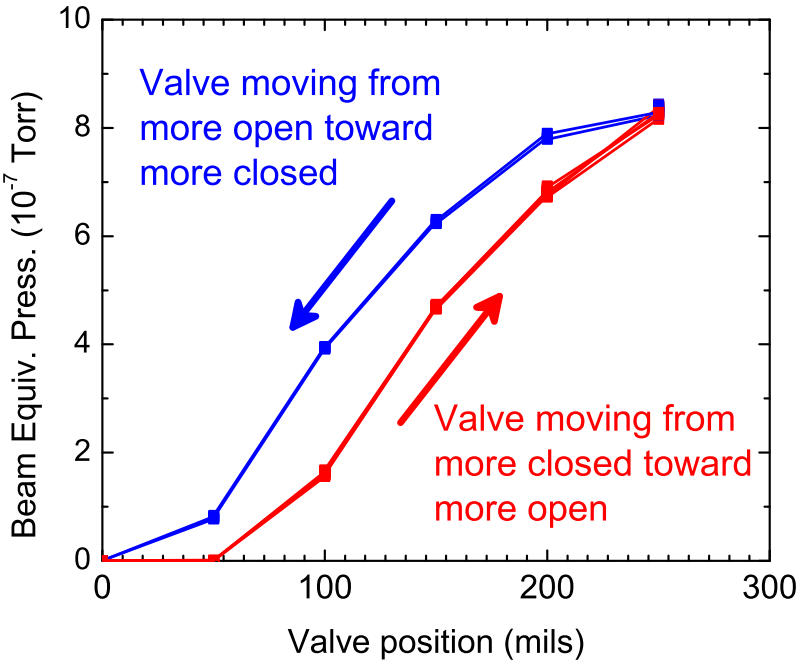

Figure 2.2: Backlash in the Sb valved cracker cell valve position. The Sb flux output is dependent on the direction the valve travels. While repeatable and reliable, it necessitates foreplanning of the direction of the valve movement for each material layer to properly supply Sb for low-temperature, and hence low-V-overpressure, growths.

2.1.3 Reflection high-energy electron diffraction (RHEED)

Due to the UHV conditions of MBE operation, electron- and ion-based *in situ* diagnostic and characterization techniques can be used. The most common technique is reflection high energy electron diffraction (RHEED). The low penetration depth of the electron beam makes RHEED very sensitive to surface effects. It is also non-destructive and is therefore a useful tool to gather information on the surface quality during growth. A beam of electrons is emitted from an electron gun with energies of 10 to 30 keV. This beam is incident on the substrate surface at shallow grazing angles of 1 to 3°. The electrons diffract off of the substrate surface toward

a viewport with a phosphor screen. The impinging electrons create photoluminescence on the screen that can be imaged using a camera out-of-vacuum and examined by the MBE operator to monitor the sample during growth.

The RHEED image informs on the composition of the surface, the growth temperature, group-V overpressure, and the surface roughness. Under typical III-V growth conditions arsenic-stable surfaces exhibit a 2x4 reconstruction pattern while antimonide-stable surfaces have a 1x3 reconstruction [76], [77]. At various substrate temperatures and group-V overpressures, different RHEED reconstruction patterns also emerge, such as the c(4x4) at lower GaAs growth temperatures. Smooth flat surfaces lead to streaky RHEED patterns, while rough surfaces or 3D features result in spotty patterns. RHEED diffraction from very rough or amorphous surfaces appears hazy, ring-like, and often dim. During thermal deoxidation at the start of growth, the hazy RHEED from the oxide layer gradually gives way to spotty bright RHEED as the oxide desorbs and the raw III-V surface becomes exposed.

RHEED can also be used to monitor the semiconductor growth rate *in situ* [78]–[80]. If the substrate is held in a fixed position, the intensity of the specular RHEED spot, the zeroth order diffraction, oscillates with a period equal to the time for one monolayer of deposition. The intensity is high when the surface is smooth. As deposition progresses, the surface becomes more rough up to one-half of a monolayer of coverage and the specular intensity concurrently drops to a minimum. The intensity then increases back to maximum as the monolayer completes and the surface becomes smooth again. The oscillation can be plotted out over time in order to extract the monolayer growth rate. This is useful as a first order measure of growth rate, that can then be later fine-tuned using an *ex situ* technique such as X-ray diffraction.

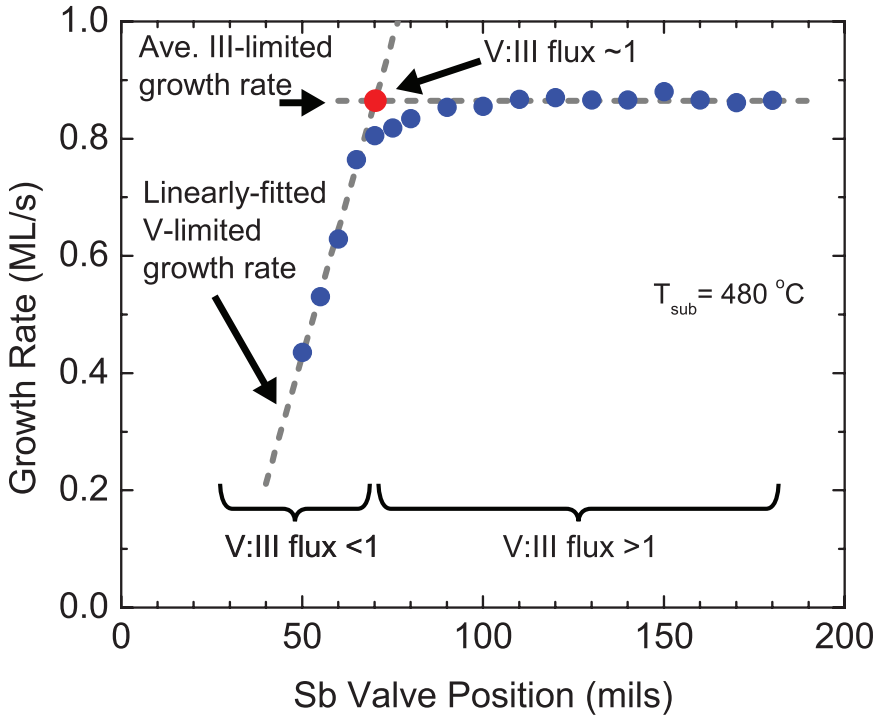

Figure 2.3: An example of III-V growth rate calibration as a function of incident V flux, measured by RHEED oscillations. For V:III flux ratios greater than unity, the growth rate is limited by the supply of III atoms. As the V flux is reduced, i.e. when the valve position is lowered, eventually the supply of V atoms limits the growth rate when the V:III ratio is less than 1. The intercept point between the two growth regimes is where the V:III flux ratio is ∼1.

When the group-V species is supplied in excess, the oscillation period represents the arrival rate of the group-III species. The opposite is true if the group-V flux is less than the group-III flux. For low growth temperatures, such as is used in the growth of the highly-strained and dilute bismide materials in this work, the group-V excess is reduced compared with typical growth temperatures. This is to inhibit group-V precipitate formation due to the reduced volatility at low temperature. It is useful to know where the crossover point occurs between group-III-limited growth and group-V limited growth. By varying the valve position for a fixed group-III cell

temperature (flux), the growth rate as a function of valve position can be mapped out. As depicted in Figure 2.3, in the group-III-limited regime, the measured RHEED oscillations and growth rate are stable with valve position. In the group-V-limited regime, the growth rate becomes a linear function of the valve position/group-V flux. The intercept of these regimes is the unity flux ratio point. Correlating this point with the measured group-V BEP gives a measurement of the group-V flux. Other fluxes can be determined in the same manner or by calculating the proportional change in BEP referenced to the calibrated point.

2.1.4 Substrate temperature measurement

Accurate measurement of the substrate temperature during semiconductor growth is critical for successful growth of the materials discussed in this dissertation. A thermocouple located near the back of the substrate holder is used to give feedback to the substrate temperature controller. However, the actual measured substrate temperature varies from the measured thermocouple temperature by up to 150 °C, so accurate monitoring and calibration of thermocouple settings is important.

The actual substrate temperature was measured using a k-Space Associates BandiT temperature measurement system. The BandiT system can measure temperature using band edge thermometry, optical pyrometry, and/or blackbody emission, and is able to accurately and reliably measure temperatures down to ∼300 °C. This is important as Nair [81] found that low growth temperatures of ∼350 °C are necessary to kinetically limit adatom mobility in order to grow highly-strained materials and limit indium surface segregation.

In band edge thermometry, the light absorption edge of the substrate is monitored. This edge is directly proportional to the band gap of the substrate material

and is temperature dependent. By monitoring the shift of the absorption edge, and hence the band gap of the substrate material, an accurate absolute wafer temperature can be measured.

The BandiT system can also measure temperature by performing a non-linear least squares fit of the blackbody thermal radiation curve to Planck's law. Unlike optical pyrometry, which uses an absolute signal level over a fixed small wavelength range, the temperature measurement using blackbody emission is affected by the shape of the measured spectra, not the amplitude. Blackbody temperature measurement is very useful for small band gap materials, such as GaSb and InAs, where band edge thermometry does not yield accurate temperature measurements, and was the main temperature measurement method used in this work.

2.2 Characterization Methods

2.2.1 X-Ray diffraction and reciprocal space mapping

X-ray diffraction (XRD) is a non-destructive, highly effective method for structural characterization of materials. It is particularly useful for studying crystalline materials such as semiconductors, as the periodic arrangement of atoms and planes in the crystal lattice creates distinct constructive interference patterns. High-resolution X-ray diffraction (HR-XRD) systems condition the incident X-ray beam so that it is low divergence and highly monochromatic. The incident beam is diffracted from a sample and collected by a detector. By using a calibrated precision goniometer, the angular orientations of the X-ray source and detector relative to the sample are well known and angularly-resolved diffraction patterns of X-ray intensity can be measured. The resulting scans are used to determine layer thicknesses, alloy compositions, superlattice periodicity, and crystalline strains and relaxation. Additional

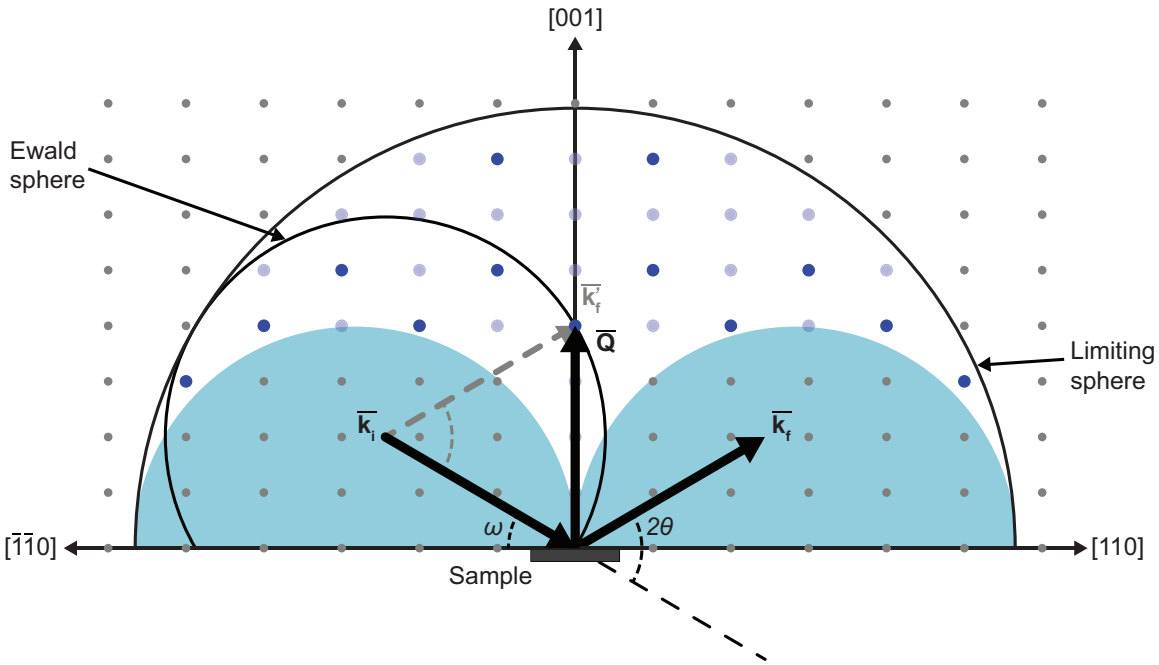

Figure 2.4: The reciprocal lattice of GaSb showing the X-ray diffraction conditions arranged to measure at the (004) reciprocal lattice point. The larger dots within the limiting sphere represent reciprocal lattice points accessible by a diffractometer using the Cu Kα_1 X-ray line, while the smaller points are inaccessible. Further diffraction selection rules for cubic zincblende materials limit the available reciprocal lattice points with constructive diffraction, indicated by the dark blue large dots.

information about crystal lattice constants can be determined from two-dimensional X-ray diffraction measurements using reciprocal space mapping (RSM). The HR-XRD and RSM measurements presented in this work were performed on a Philips Panalytical X'pert diffractometer and a Rigaku Smartlab diffractometer.

A common HR-XRD measurement is the coupled ω-2θ scan. The incident beam angle is rotated through the angle ω while the detector angle, or scattering angle, 2θ is rotated at twice the rate, so that $2\Delta\omega = \Delta 2\theta$. Diffraction patterns result from interference of scattered X-rays off of the atomic planes in the examined sample. The scattering plane is spanned by the incoming wavevector $\overline{k_i}$ and the outgoing

wavevector $\overline{\mathbf{k_f}}$. The angle between these two vectors is the scattering angle 2θ. The resultant scattering vector $\overline{\mathbf{Q}}$ gives the momentum transfer due to the scattering process. Figure 2.4 shows the GaSb reciprocal lattice and the geometry of a coupled ω-2θ measurement of the diffraction peak arising due to the (004) crystal plane using the copper Kα_1 X-ray line (λ=1.54056 Å).

Symmetric coupled scans are typically used to measure the scattering vector $\overline{\mathbf{Q}}$ along the [001] reciprocal axis. In these scans, the $\overline{\mathbf{Q}}$ vector is parallel to and probes the crystal planes in the growth direction. Symmetric scans for zincblende materials are taken about the (004) reciprocal lattice point because it is the only reciprocal lattice point on the [001] axis that exhibits a constructive diffraction peak due to diffraction selection rules. Despite this limited measurement range for the zincblende materials, structural characteristics including composition, layer thicknesses, and coherent strain can be determined using symmetric coupled scans.

A limitation of symmetric coupled scans along the [001] axis is that they only give information from the crystal planes in the growth direction. While these scans can show evidence of strain relaxation, they cannot be used to quantify it. To do this, 2D reciprocal space maps are taken around an off-axis diffraction peak, such as the (224) reciprocal lattice point. The ω angle is stepped and a coupled ω-2θ scan is taken at each step to map out a 2D reciprocal area. Each couple scan measures along a radius from the reciprocal coordinate origin, and the array of these radii form a truncated circular sector over the scan region. In off-axis reciprocal space mappings, coherently-strained layers are aligned at the same in-plane reciprocal lattice point, while layers that are relaxing shift toward the native lattice constant of the bulk material.

2.2.2 Photoluminescence

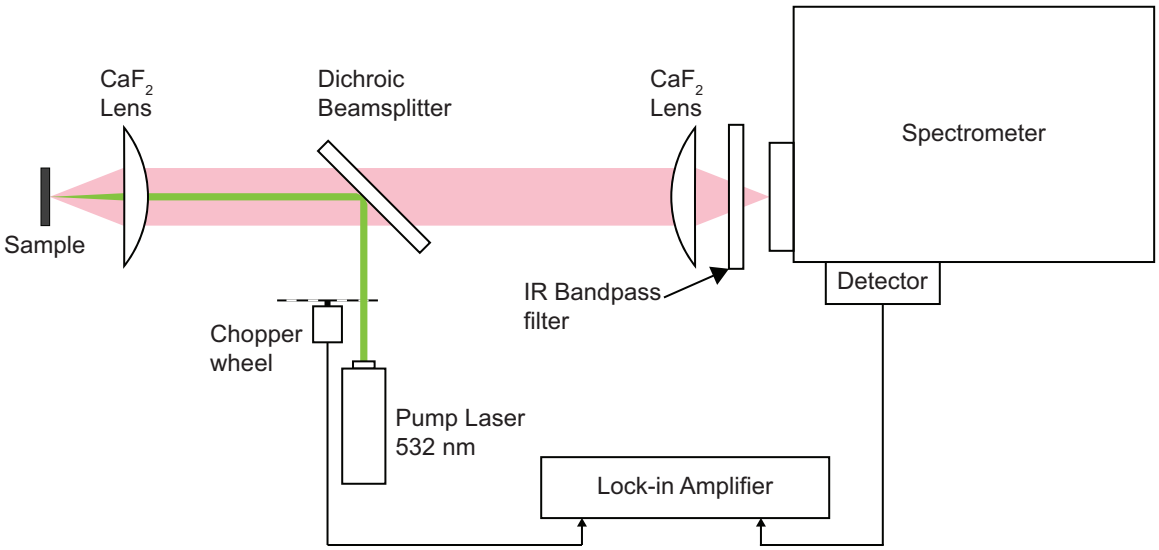

Figure 2.5: Schematic diagram of the custom colinear optical test bench used for spectrally resolved measurements in this work. The schematic depicts the test bench measuring photoluminescence.

Photoluminescence (PL) is the emission of light from matter following photon absorption and excitation. PL spectroscopy is very useful as a non-destructive optical characterization technique used to measure the band gap and material optical quality of semiconductor materials. A semiconductor sample is optically excited by a laser with photon energy greater than the semiconductor band gap. The photons are absorbed by the semiconductor, generating electron-hole pairs. This process happens within a few absorption lengths from the semiconductor surface, although the specific length depends on the semiconductor material and the incident photon wavelength. The generated electron-hole pairs spontaneously relax quickly ($<$1 ps) to the conductance and valence band edges through phonon emission, diffuse through the semiconductor, and recombine either radiatively or non-radiatively. The light generated by the electron-hole pairs that radiatively recombine is collected for

analysis, usually by collecting the emission spectrum through a spectrometer. The spectrum of the emitted light provides insight into the electronic band gap of the semiconductor as well as the optical quality of the grown specimen. Materials with fewer defects or other non-radiative recombination centers exhibit stronger luminescence amplitudes. A more thorough treatment is given by Gfroerer [82].

The PL data presented in this dissertation were measured using a custom colinear PL test bench, schematically illustrated in Figure 2.5. Semiconductor samples were optically excited using a frequency-doubled neodymium-doped yttrium aluminum garnet (Nd:YAG) solid-state diode-pumped laser emitting at 532 nm and intensity-modulated using a chopper wheel. The excitation intensity could be reduced if necessary through the use of neutral-density filters. Mirrors and CaF_2 optics were used to direct the laser light to the semiconductor sample as well as to collect the emitted PL. A dichroic beamsplitter and a bandpass optical filter were used to separate reflected laser light before the PL emission was dispersed through a 0.5-m grating spectrometer to a detector. A lock-in amplifier connected to the detector and the chopper wheel signal were used for homodyne detection in order to maximize the signal-to-noise ratio of the measured PL. Mid-infrared spectral measurements were collected using a liquid-nitrogen-cooled InSb detector with a 5.5 μm cutoff and with the PL test bench purged with a nitrogen ambient to minimize atmospheric absorption features due to water and carbon dioxide.

2.2.3 Photoreflectance spectroscopy

Photoreflectance (PR) spectroscopy is a contactless modulation spectroscopy technique that measures the change in sample reflectivity in response to intensity-modulated incident light. The change in reflectivity arises due to differential changes

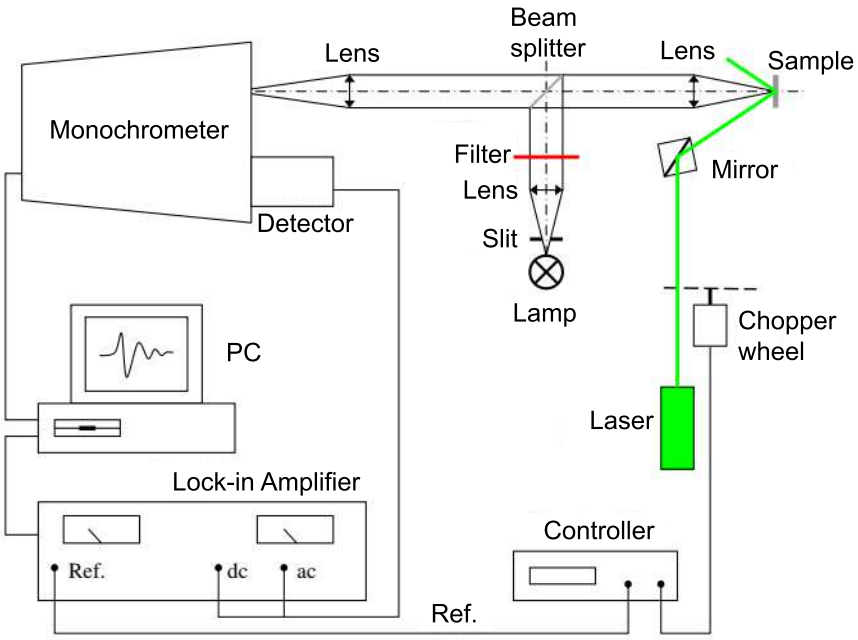

Figure 2.6: Schematic diagram of a photoreflectance experimental test bench using the bright configuration, after [83].

in the dielectric function as the internal electric field is modulated by the incident pump light. These changes are due to optical transitions that manifest as derivative-like features at critical points in the reflectance spectrum at the photon energies of interband transitions. A useful aspect of this measurement is that it can be used to probe for the existence of higher ordered electronic transitions in materials, yielding more information about potential band alignments of heterostructures such as quantum wells.

A schematic representation of a PR setup is given in Figure 2.6 [83]. A pump laser is intensity modulated by a chopper wheel and incident on a semiconductor sample. The absorbed light creates electron-hole pairs that screen the internal elec-

tric fields located at already-present space-charge regions in the material at interfaces and free surfaces. This field modulation causes perturbations in the dielectric function that appear in the reflectance spectrum. A probe light source samples the modulated reflectivity ΔR. The PR measurements presented in this work were measured by Professor Robert Kudrawiec's research group at Wrocław University of Science and Technology in Wrocław, Poland.

Chapter 3

Mid-infrared Lasers using Highly-Strained Materials

The first semiconductors lasers were demonstrated in 1962 [84], [85]. These devices were designed using homojunctions and were inherently inefficient. Without carrier confinement, injected carriers are free to diffuse throughout the junction and dilute the gain. Additionally, without optical confinement or guiding of the optical mode, overlap with the gain region is poor. Due to the high optical and electrical losses these devices only worked with extremely high threshold current densities on the order of 100 kA/cm^2 and needed substantial cooling in order to operate even in pulsed mode. The double heterostructure laser was proposed a year later, in 1963 [86], [87], and first demonstrated in 1966 using GaAsP [88]. In 1968, the first room-temperature continuous wave (cw) semiconductor laser was realized using a GaAs/AlGaAs double heterostructure [89]. The double heterostructure design brought laser threshold current density down to $\sim$1 kA/cm^2. With improved crystal growing techniques, namely molecular beam epitaxy and metal-organic chemical vapor deposition, the quantum well laser was demonstrated in 1975 [90]. By 1981, MBE–grown quantum well lasers exhibited threshold current densities as low as 160 A/cm^2 [91].

Due to concern for relaxation, threading dislocations, and other defects, the first semiconductor lasers were grown with lattice-matched or nearly lattice-matched layers. In 1986, two groups independently proposed that purposefully adding strain in the emitting region would offer performance advantages for lasers [63], [64].

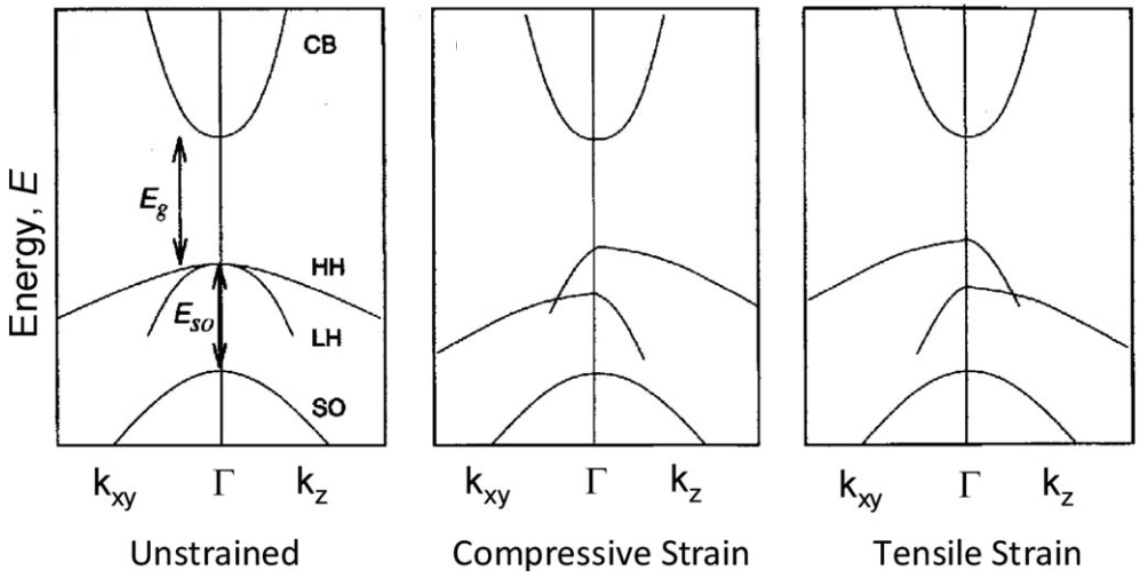

(a) (b) (c)

Figure 3.1: Simple illustration [92] of the band structure of a semiconductor near the center of the Brillouin zone. CB - conduction band; HH - heavy hole valence band; LH - light hole valence band; SO - split-off band; E_g - band gap energy; E_{SO} - split-off energy. (a) The unstrained semiconductor has a valence band degeneracy at zone center where the HH and LH bands overlap. Adding strain breaks that degeneracy. Specifically (b) compressive strain lifts the (out-of-plane) heavy hole band, whereas (c) tensile strain lifts the (out-of-plane) light hole band.

This was subsequently confirmed, with both compressive and tensile strains offering performance advantages over unstrained devices [93]. The strained quantum well lasers had low threshold current density and record cw output power. More importantly, adding strain did not result in reduced material optical quality. Unstrained, III-V materials have degenerate heavy hole and light hole valence bands at the center of the Brillouin zone, as illustrated in Figure 3.1a. Straining the semiconductor lattice breaks that degeneracy. For a compressively strained layer, as depicted in Figure

3.1b, the heavy-hole band moves up in energy relative to the light-hole band; the opposite occurs for tensile strain (Figure 3.1c). For a compressively strained layer, at the top of the valence band, the in-plane hole effective mass becomes lighter than the effective mass in the growth direction; the opposite is true for the case of tensile strain. Specifically for compressively strained materials the heavy hole band is lifted above the light hole band, lowering the density of states near zone center and reducing the carrier density needed to reach laser threshold, leading to lower threshold current. Combining compressive strain with quantum confined regions as strained QWs reduces the threshold carrier density by several orders of magnitude. Incorporating strain within the emitting layers enhances a number of laser performance metrics in addition to reduced threshold current densities, such as increased differential quantum efficiency, output powers, and operational bandwidth; and decreased linewidth and chirp. There is also more freedom in active region alloy design. Lattice-matched and nearly lattice-matched laser active regions and quantum wells are limited to those alloys with a similar lattice parameter to the several available substrates such as GaAs, InP, and GaSb. Using strained alloys opens up the alloy design space, giving access to more wavelengths and band offsets.

This chapter will detail investigations into highly-strained GaInAsSb materials for type-I diode laser active regions. By leveraging the extra valence band offset afforded by compressive QW strains well above 2%, type-I QW emission has been extended out past 4 μm. A type-I diode laser with the longest emission wavelength from an aluminum-free active region will be discussed, along with a proposed laser design for future development to push the emission wavelength of type-I diode lasers out to ~4.1 μm.

3.1 Extending the emission wavelength in mid-infrared emitters

The quaternary alloy GaInAsSb is the standard QW material used in GaSb-based mid-infrared devices. Watt-level output powers have been demonstrated in GaInAsSb/AlGaAsSb lasers emitting at room temperature up to about 2.5 μm [54], [94] and outputs of hundreds of milliwatts exist from 2.5 to past 3 μm [95], [96]. These devices typically employ barrier layers consisting of alloys of AlGaAsSb or AlGaInAsSb lattice-matched to GaSb. Type-I GaSb-based lasers with AlGaAsSb barriers have been demonstrated out to 3.1 μm [97]. These devices exhibit excellent operating characteristics including low operating voltage, low threshold current, and high stability over operating temperature (Figure 1.4).

3.1.1 Alloy design for longer wavelengths

The typical approach used to extend emission to longer wavelengths in GaInAsSb is illustrated in Figure 3.2. In order to increase the emission wavelength, the indium fraction is increased in the alloy, decreasing the band gap of the material (Figure 3.2a). The additional indium also adds compressive strain to the alloy, which is a mixed blessing. Compressive strain helps improve the valence band offset and hole confinement in the QW; however, too much strain leads to strain relaxation and material degradation. The increase of strain with increased indium is rapid, with only a 15% increase in indium content increasing the strain by 1%. At the same time, the band gap shift in GaInSb alloys equals only 150 meV per percent strain increase [98]. Increasing the indium content too much pushes strained layers past the relaxation limit where roughening occurs and misfit dislocations begin to form, both of which degrade luminescence efficiency and hinder laser devices. To avoid these outcomes, the QW number must either be reduced, hampering laser performance

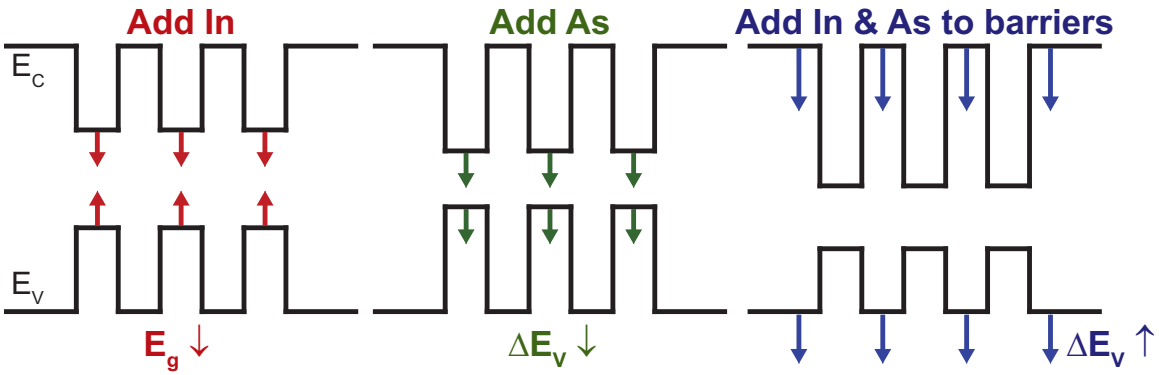

Figure 3.2: Illustration of a typical approach to extending the laser emission wavelength in GaSb-based type-I QW diode lasers. (a) Increasing the indium content of GaInAsSb QWs decreases the band gap and increases the compressive strain in the QWs. In order to mitigate strain limitations, (b) the arsenic content of the QWs must also be increased. This has the undesired consequence of reducing the valence band offset, thereby reducing the hole confinement in the QWs. (c) By adding indium and increasing the arsenic content in the AlGaAsSb barrier layers, the conduction and valence band offsets are able to be independently tuned, allowing sufficient confinement for holes while avoiding uneven electron distribution in the conduction band.

due to gain saturation, or the QW strain must be mitigated. By increasing the QW arsenic fraction the compressive strain in the QW decreases while having a much slighter effect on wavelength than the change in indium content (see Figure 3.2b). The drawback of this approach is that the increase in both QW indium and arsenic content has the effect of making the overall alloy more InAs-like, meaning a lowered valence band edge and a band alignment that tends toward type-II in these alloys [68]. The lowered valence band results in a reduced barrier for hole confinement in the QW, hampering laser performance beyond 3 μm [99].

While the lowered valence band due to increasing the arsenic content is detrimental in the QW, it is potentially beneficial in the barrier material, as lowered bar-

rier valence bands would improve the offset to the QW. In order to maintain lattice matching in the barriers, the increased arsenic is countered with an increase in aluminum content. However, the increased barrier aluminum content provides a larger increase to the conduction band offset, potentially leading to non-uniform carrier injection in multi-QW active regions, as well as a reduction in the refractive index contrast between the waveguide/active region and the cladding, typically $Al_{0.9}Ga_{0.1}As_{0.076}Sb_{0.924}$, which reduces the optical confinement allowing the optical mode to leak into the doped cladding layers and increasing losses to to free carrier absorption.

To counter this, many groups alter the barrier material by adding indium and arsenic to form a complex lattice-matched AlGaInAsSb alloy (Figure 3.2c) [69], [99], [100]. This creates the advantage of independent tuning of the conduction and valence band offsets of the barriers to the QWs, at the expense of increased growth complexity and calibration. In many cases undesirable pauses during crystal growth are necessary to allow for tuning of the individual element sources for different layer alloy compositions. By combining the steps illustrated in Figure 1.3—increased QW indium to reduce the band gap, increased QW arsenic content to mitigate strain, and adding aluminum, indium, and arsenic to the barrier alloy—the emission wavelength of type-I diode lasers has been extended as long as 3.73 µm [69].

3.2 High-strain, high-indium content quantum wells

High performing lasers operating between 2 and 4 µm are summarized in Figure 3.3, organized by QW indium content, QW compressive strain, and QW barrier type. This survey of reported devices highlights that laser emission wavelength is strongly tied to the QW indium content. It also illustrates the device design shift

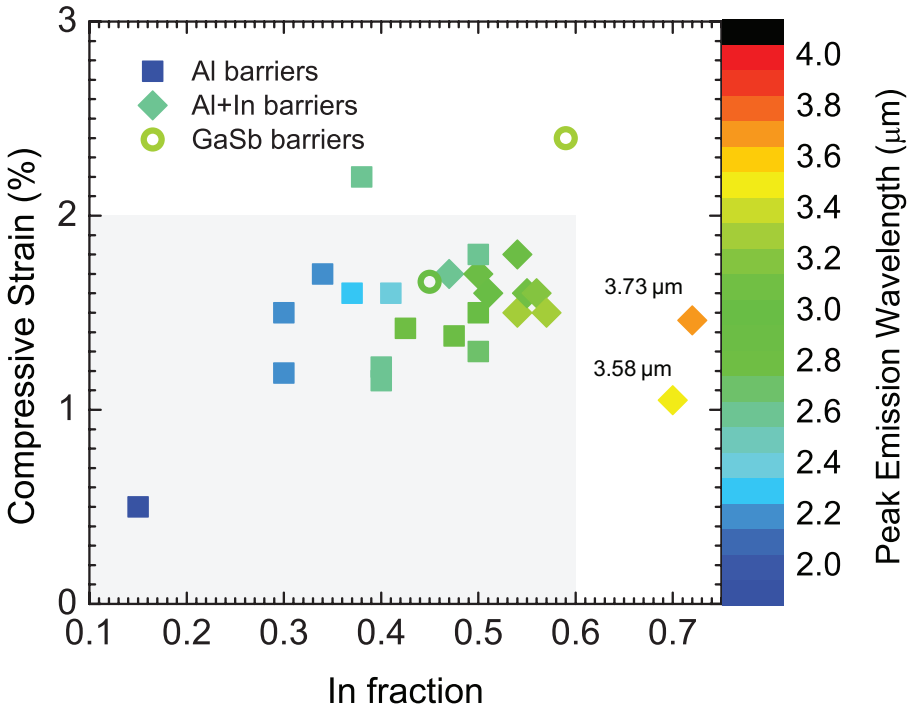

Figure 3.3: Summary of the emission wavelength of QW diode lasers operating between 2 to 4 µm, as a function of the QW indium content and strain. The lasers are further classified by QW barrier type, with squares indicating AlGaAsSb barriers, diamonds indicating AlGaInAsSb barriers, and open circles indicating GaSb barriers. The light gray box highlights a "design space" within which most literature devices fall. Most reported devices limit QW indium content to <60% and QW compressive strains to <2%. Notably, the only two reported devices emitting longer than 3.5 µm have QW indium fractions >60%. Data from [9], [54], [56], [61], [67]–[69], [94], [95], [97], [101]–[108]

from AlGaAsSb QW barriers to AlGaInAsSb QW barriers that occurs at QW indium fractions of ∼0.5. From this figure we can deduce that in order to push the emission wavelength past 3.5 µm in GaInAsSb QWs, the QW indium fraction needs to exceed 0.6, as the only two reported devices operating longer than 3.5 µm are also the only devices having QW indium content greater than 60% [69], [108]. Additionally, since most devices have maximum QW compressive strains under 2%, the high arsenic content necessary to maintain these strain levels as the QW indium content

is increased further limits wavelength extension as the QW valence band offsets and hole confinement diminish.

While increasing the QW compressive strain can improve the valence band offset, allowing for better hole confinement and lower lasing thresholds, most reported work has restricted QW strain to less than 2% in order to avoid strain relaxation in the QW region [69], [97], [103]. Alternatively, if strain is allowed to increase by limiting the QW arsenic content, the QW indium content can be further increased while maintaining type-I band alignments, even with aluminum-free barriers. Nair demonstrated that strains well beyond 2% can be reached through lower MBE substrate growth temperatures [8], [81]. QW test samples grown at 410 °C [81], [97] exhibited increased photoluminescence (PL) at strains up to ∼2.1%. At higher strains PL rapidly degraded and high-resolution X-ray diffraction (HR-XRD) measurements indicated the onset of strain relaxation. By reducing the substrate temperature to 350 °C, Nair achieved improved QW structural and optical quality, increasing strains up to 2.45% while maintaining bright luminescence. HR-XRD measurements of the QW samples with diminished PL and grown at 410 °C exhibited decreased layer fringe resolution, indicating reduced interface quality between the QW and the upper barrier material. This points to indium surface segregation during the growth of highly strained materials as a likely explanation for the degraded optical quality [109]. By reducing the substrate temperature during growth, the indium surface segregation can be kinetically suppressed increasing the indium incorporation in the QWs and maintaining higher structural quality of the grown structures.

By limiting or avoiding aluminum in the barriers, the refractive index contrast between waveguide and cladding is also higher, providing better optical mode con-

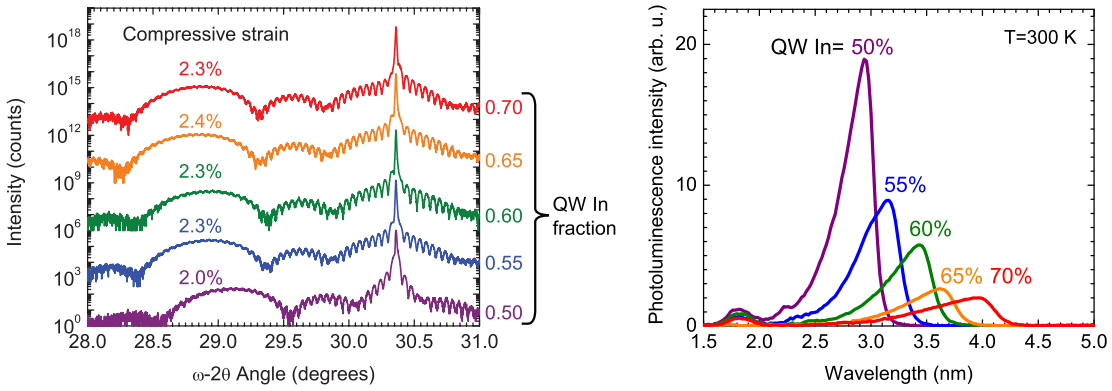

(a) (b)

Figure 3.4: (a) HR-XRD diffraction patterns of highly-strained QWs show the QWs maintaining coherent strains of up to 2.4% as the QW indium fraction is swept from 0.5 to 0.7. (b) At the same time, the peak photoluminescence of these QWs spans the spectral range between 3 μm and 4 μm.

finement within the active region which leads to higher differential gain and lower losses due to absorption in the cladding [100]. Utilizing this approach with highly-strained GaInAsSb QWs, Nair demonstrated room temperature laser emission at 3.4 μm from an aluminum-free active region using $Ga_{0.41}In_{0.59}As_{0.19}Sb_{0.81}$/GaSb QWs with 2.4% compressive strain. The calculated valence band offset of the QWs in this device is 76 meV.

Expanding on Nair's work, we examined the effect of indium content and quantum-well strain on the material quality and emission wavelength of GaSb-based quantum wells. GaInAsSb/GaSb QWs were grown at 350 °C on GaSb substrates. A 200-nm GaSb buffer was grown on the thermally oxidized substrate. The first 100 nm of the buffer was grown at 475 °C, and then the substrate temperature was ramped down to and stabilized at 350 °C during the second 100 nm. The substrate temperature was held at 350 °C for the QW growth and for the growth of the 100-nm

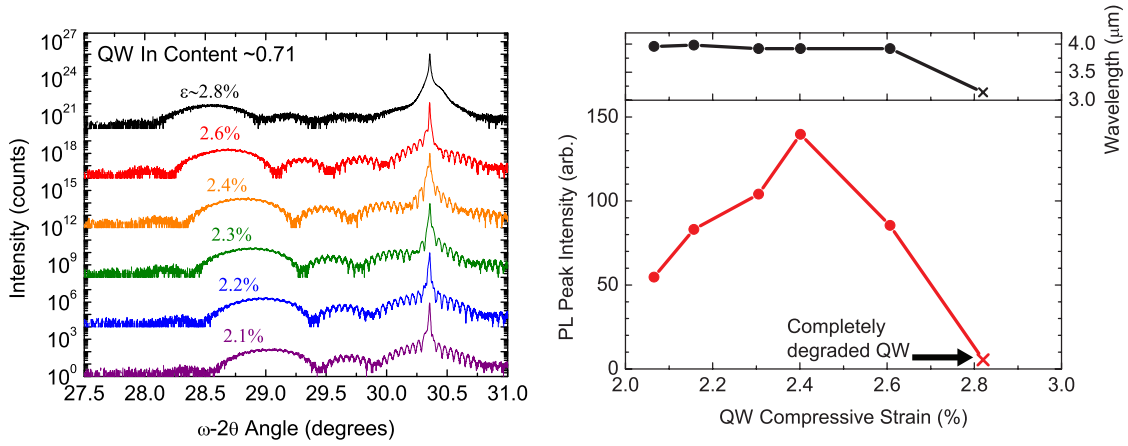

(a) (b)

Figure 3.5: For fixed indium content, the QW strain can be tuned by adjusting the As:Sb ratio, with lower As content resulting in higher strains. (a) HR-XRD diffraction scans show coherent QW strain with strong Pendellösung fringes visible up to 2.6% compressive strain. Those fringes are wiped out at 2.9% strain, indicative of degraded heterointerfaces. (b) (upper) Peak emission wavelength stayed constant as strain was tuned up to 2.6%, and (lower) peak photoluminescence intensity increased with increasing strain up to 2.4% before starting to decline at 2.6% strain. At 2.9% strain, there was no photoluminescence observed.

GaSb capping layer in order to prevent indium segregation or outdiffusion from the QW [109].

Maximum QW compressive strain was held to ∼2.4% by increasing the QW arsenic content as the indium content was increased. HR-XRD scans, in Figure 3.4a, showed good structural integrity and heterointerface quality of the QWs as the indium content was swept from 0.5 to 0.7. The strong Pendellösung fringes indicate that indium segregation was successfully suppressed. The increased QW indium content also red-shifted the PL emission spectra (Figure 3.4b), with the emission peak spanning from 3 μm to 4 μm, confirming the dependency of emission wavelength on the indium content of the QW.

In order to understand the upper bounds of achievable QW strains, another set of QWs was prepared with fixed indium content and various arsenic content in order to measure performance over a range of compressive strains. QWs with indium content ∼0.71 were grown under similar conditions to the previous set with the arsenic content being swept to adjust the QW compressive strain. Again, strong Pendellösung fringes and well-formed QW layer peaks were seen in HR-XRD scans (Figure 3.5a), up to ∼2.6% strain. Peak PL intensity was maximal at a compressive strain of 2.4% (Figure 3.5b, lower), while the peak emission wavelength varied only slightly as the arsenic content was changed (Figure 3.5b, upper). At 2.9% compressive strain, however, the structural integrity was lost as indicated by the lack of layer thickness fringes shown in Figure 3.5a as well as severely degraded QW emission.

While QW PL emission was demonstrated out to 4 µm, at the highest indium contents the PL linewidth broadened significantly (Figure 3.6), along with steady declines in PL intensity. Despite maintaining high strains, the QW arsenic content was also being increased along with the indium in order to limit strains to ∼2.4%. Band structure calculations indicate that the valence band offset is ∼10 meV at the highest indium concentrations, offering poor hole confinement.

QWs were also grown with 72% QW indium content, having either GaSb barriers or lattice-matched $Al_{0.3}Ga_{0.7}As_{0.03}Sb_{0.97}$ barriers. The QW with GaSb barriers had a weak PL peak at ∼4.2 µm. However the linewidths remained very broad and calculated valence band offsets were low. Moreover, while the previous QWs exhibited an exponential trend to the peak PL emission with valence band offset (Figure 3.7), the PL from the QW with 72% indium was severely quenched and was well below the fit line. While the effect due to low valence band offsets was delayed by using high strains greater than 2%, by ∼70% QW indium content it

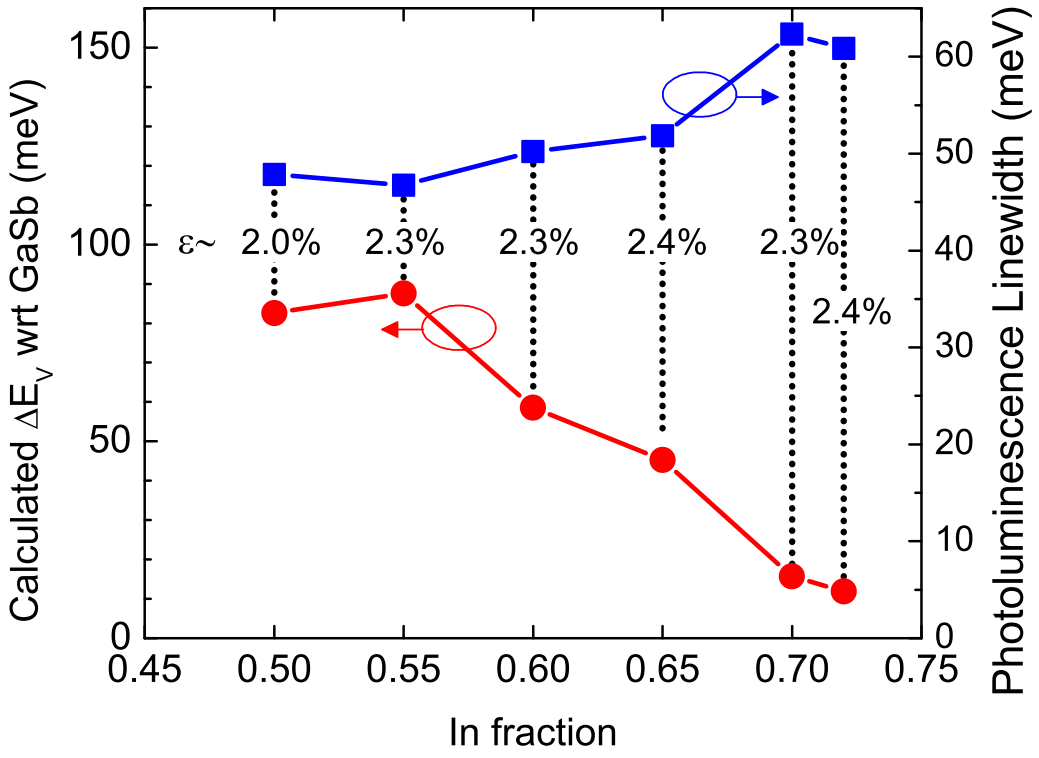

Figure 3.6: Calculated valence band offset (red, left axis) and measured PL emission linewidth (blue, right axis) across a range of QW indium concentrations for QW compressive strains ~2.3%.

has reemerged. Comparative PL measurements, shown in Figure 3.8, of these QWs with and without aluminum barriers show that type-I alignments are restored by using moderate aluminum-containing barriers. The additional carrier confinement afforded by the aluminum barriers manifested in greater than 3× PL peak intensity improvement, while the spectral linewidth narrowed over 30% from 53 meV to 42 meV, on the order of the QWs with lower indium content and aluminum-free barriers.

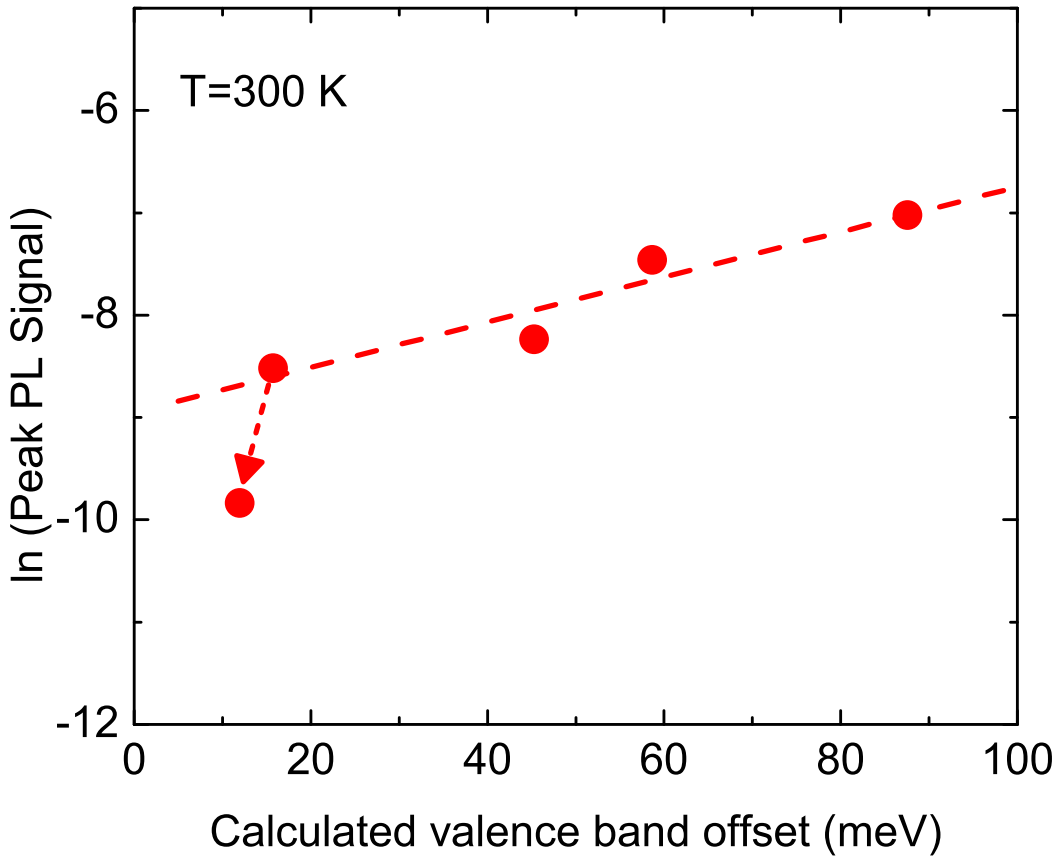

Figure 3.7: The peak photoluminescence intensity for ∼2.3% compressively-strained GaInAsSB quantum wells follows an exponential fit with the calculated valence band offset for quantum well fractional indium concentrations up to 0.7. At higher indium concentrations, the intensity rolls off sharply, indicative of the transition toward type-II band alignments.

3.3 Type-I diode laser emitting at 3.62 µm

A laser diode structure was grown using a multi-QW active region. The laser structure was grown on a 2-inch Te-doped GaSb substrate. Following thermal deoxidation of the wafer at 550 °C under an Sb_2 overpressure, the substrate was ramped to 475 °C. Growth was initiated with 100-nm of Te-doped (2×10^{18} cm^{-3}) grown at

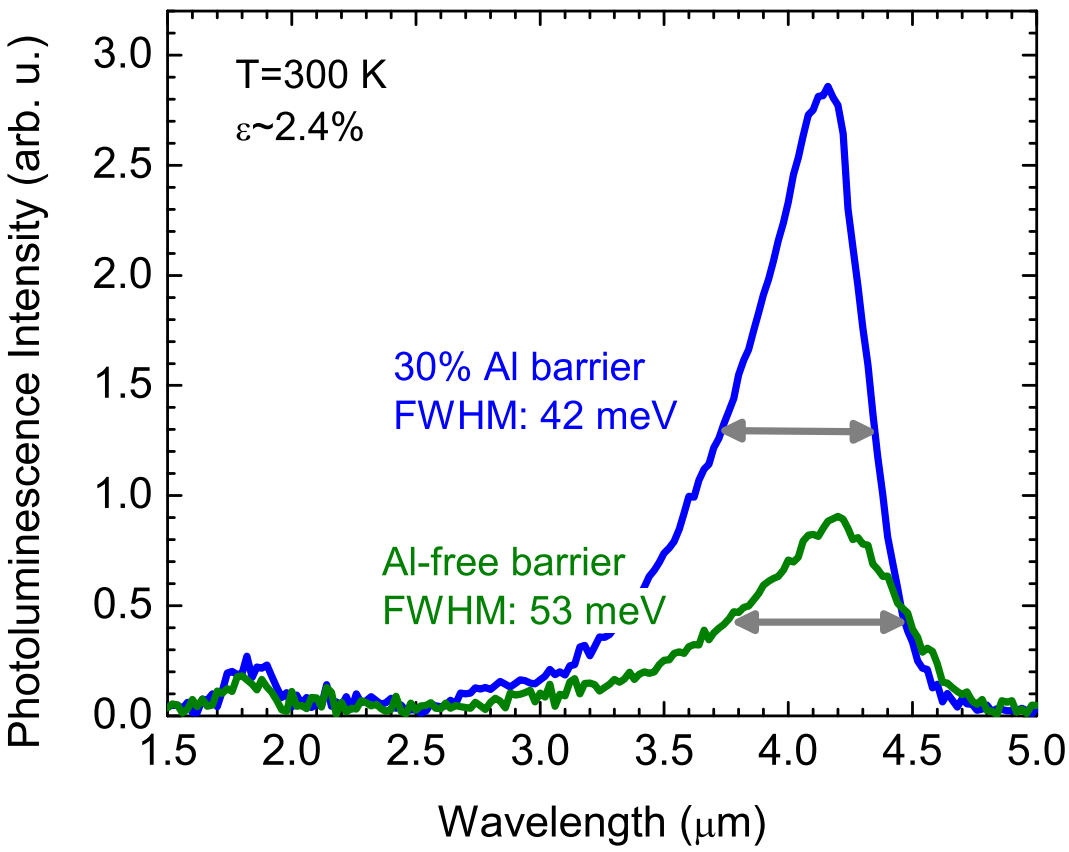

Figure 3.8: GaInAsSb QW with 0.72 fractional indium content and 2.4% compressive strain, with and without lattice-matched $Al_{0.3}Ga_{0.7}As_{0.03}Sb_{0.97}$ barriers. Adding aluminum-containing QW barriers increased peak PL intensity by >3×and narrowed the linewidth by >30%, indicating restored type-I QW band alignments.

475 °C. The substrate was then ramped to 350 °C during a second 100-nm Te-doped GaSb layer. The remainder of the laser structure was grown at 350 °C. The bottom cladding was 1.8 µm Te-doped $Al_{0.5}Ga_{0.5}As_{0.04}Sb_{0.96}$. The first 1.3 µm was doped to 1×10^{18} cm^{-3}, while the 0.5 µm nearest the waveguide was doped to 2×10^{17} cm^{-3} in order to minimize free carrier absorption due to holes. The active region was made of 4 highly-strained $Ga_{0.34}In_{0.66}As_{0.28}Sb_{0.72}$ 10-nm QWs separated by 20

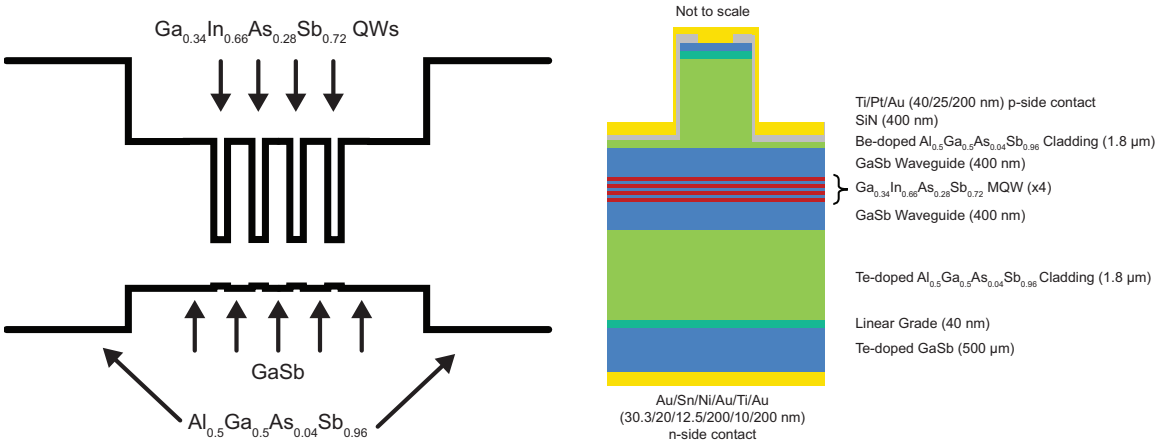

(a) (b)

Figure 3.9: (a) Calculated energy band diagram of a laser structure with 4 $Ga_{0.34}In_{0.66}As_{0.28}Sb_{0.72}$ QWs, GaSb QW barriers/laser waveguide, and claddings of lattice-matched $Al_{0.5}Ga_{0.5}As_{0.04}Sb_{0.96}$. (b) An edge-view of a fabricated laser device with annotated layers and materials.

nm of GaSb. 400-nm GaSb layers were grown below and above the active region, forming a 900-nm waveguide/active region. The top cladding was 1.8 μm Be-doped $Al_{0.5}Ga_{0.5}As_{0.04}Sb_{0.96}$. The first 0.5 μm was doped to 2×10^{17} cm^{-3}, while the next 1.3 μm was doped to 8×10^{17} cm^{-3}. The top contact layer was a 100-nm thick GaSb layer doped with Te to 5×10^{18} cm^{-3}. Highly doped 40-nm thick graded band gap layers were inserted between the buffer and the bottom cladding, and the top cladding and the top contact to reduce the current barrier. Except for the buffer the entire structure was grown at 350 °C in order to minimize thermal annealing of the highly-strained quantum wells as well as to utilize the same calibrations for similar top and bottom layers.

Samples were fabricated into ridge-waveguide edge emitting laser devices, as shown in Figure 3.9b. Following the fabrication procedure in Appendix A, first 400-nm of silicon nitride was deposited on the sample using PECVD. The laser stripes

were patterned using conventional photolithography steps. The silicon nitride was etched using a CF_4/O_2 plasma leaving silicon nitride bars as a hard mask for ridge etching. The ridge was etched using a Cl_2-N_2 ion-coupled plasma etch chemistry, to $\sim$100-150 nm from the waveguide region. Following the etch, the remaining silicon nitride was stripped off using a CF_4/O_2 plasma etch, leaving just the processed III-V material. A new 400-nm silicon nitride layer was deposited to protect the exposed aluminum ridge sidewalls. A second conventional photolithography step was used to pattern the ridge contact windows. The contact windows were opened in the silicon nitride using a CF_4/O_2 plasma etch. A third conventional photolithography step was used to define the top metal contact. The top metal contact was deposited using an electron beam evaporator. The contact metal was Ti/Pt/Au (40/25/200 nm). Following top metalization the substrate was thinned down to $\sim$100 µm using mechanical lapping and polishing, to facilitate better facet cleaving. A bottom metal contact of Au/Sn/Ni/Au (30.3/20/12.5/200 nm) was deposited using an electron beam evaporator. The contacts were annealed to 350 °C for 1 minute using a rapid thermal annealer. Following annealing, a second metal layer of Ti/Au (10/200 nm) was deposited on the bottom metal contact.

The processed sample was cleaved into 2-mm long laser bars. The facets were left as-cleaved. Laser bars were mounted epi-side down onto a prepared gold-coated silicon wafer carrier. The contacts were wirebonded to gold-coated alumina stand-offs. The device and carrier were mounted on a cryostat cold finger with cryostat wire soldered between the bond pads and a electrical bulkhead on the cryostat. The cold finger was mounted in the cryostat, which was then put under vacuum. The cryostat was cooled using liquid nitrogen. A built-in oven was used to adjust the

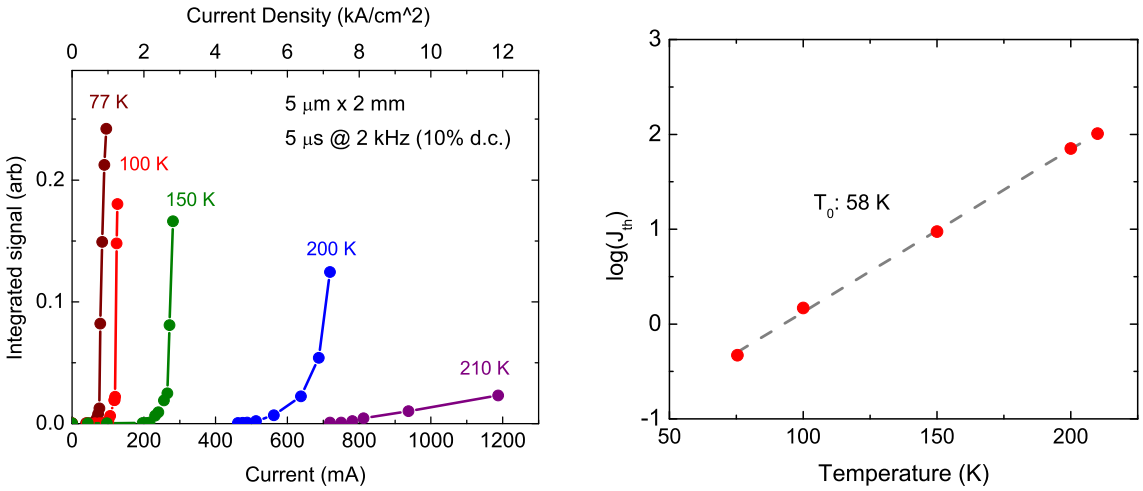

Figure 3.10: (a) L-I curves from a 5 μm×2 mm ridge waveguide laser operating in pulsed mode (5 μs/2 kHz) up to 210 K. (b) Natural logarithm of pulsed threshold current with device temperature. This laser exhibits a characteristic temperature of threshold current of 58 K, one of the highest reported values for a diode laser operating longer than 3 μm.

temperature between 77 K and room temperature via a temperature controller to facilitate device testing.

5 μm by 2 mm laser stripes were electrically driven in pulsed mode using 5 μs pulses at a 2 kHz pulse rate (10% duty cycle). L-I curves as a function of temperature are shown in Figure 3.10a. The high threshold current densities, particularly at temperatures above 100 K are indicative of the poor hole confinement in the QW active region. The calculated valence band offset for this active region is only 17 meV. Using $Al_{0.3}Ga_{0.7}As_{0.03}Sb_{0.97}$ barriers would add ~130 meV to the valence band offset making a sufficient well for carrier confinement, and reducing threshold current densities. The emission wavelength of 3.62 μm at 210 K is the longest emission wavelength from a type-I diode laser with an aluminum-free active region. Extrapolating

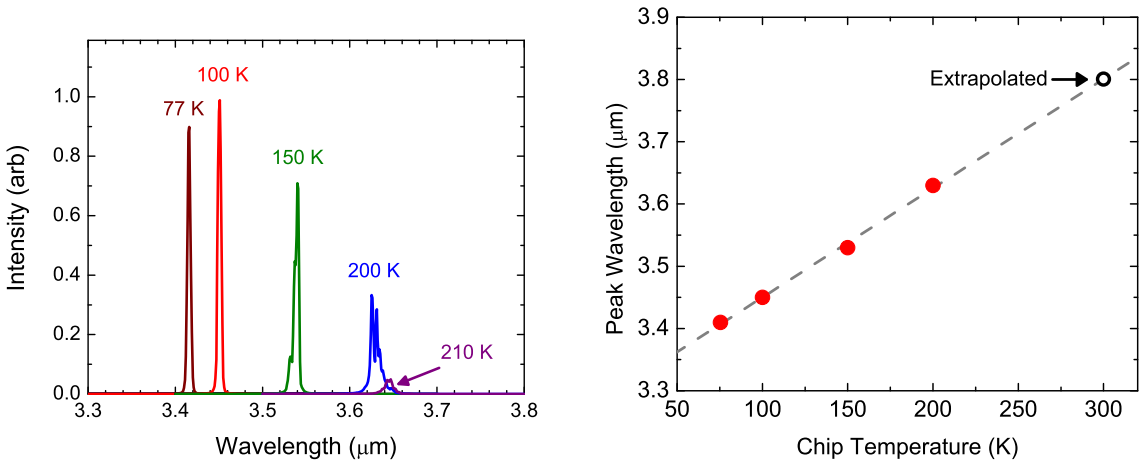

(a) (b)

Figure 3.11: (a) Measured laser emission spectra at select chip temperatures, spanning 3.4 µm to 3.62 µm. (b) Temperature dependence of the device emission wavelength. Extrapolating to room temperature results in an operating wavelength of 3.8 µm

the operating wavelength to room temperature results in an emission wavelength of 3.8 µm which would make this device the longest wavelength emission from any type-I diode laser. The characteristic temperature of threshold current, T_0, of this device was 58 K across the device operating temperature range, one of the highest reported for a diode laser operating in this wavelength range. It suggests that large splin-orbit splitting is maintained even if hole confinement is low.

3.4 Proposed type-I diode lasers for 4+ µmoperation

The laser structure design and calculated band diagram are shown in Figure 3.12 for a proposed laser diode device designed to operate ~4.1 µm. By switching from aluminum-free barriers to 30%-aluminum containing lattice matched QW barriers, an additional 130 meV can be added to the valence band edge of the barriers,

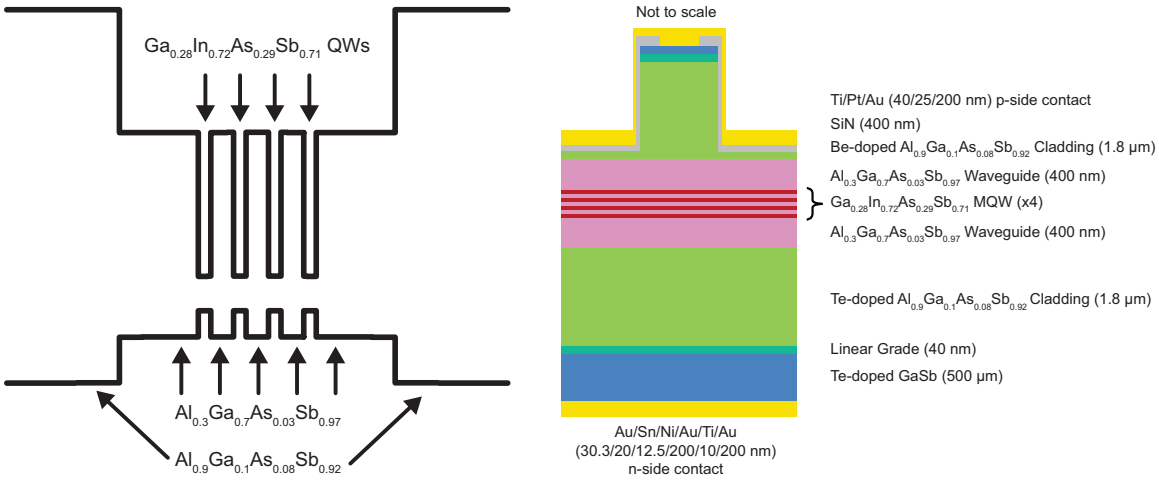

Figure 3.12: (a) Calculated band diagram and (b) cross section of proposed $Ga_{0.28}In_{0.72}As_{0.29}Sb_{0.71}$ multi-quantum well diode laser emitting at 4.1 μm with layers annotated.

providing sufficient offset for hole confinement in QWs operating up to 4.2 μm (Figure 3.8). By altering the design structure from a 0%-aluminum waveguide / 50%-aluminum cladding, to a 30%-aluminum waveguide / 90%-aluminum cladding, the necessary hole confinement can be obtained with minimal sacrifice to the index contrast and optical mode confinement.

Unfortunately, due to both indium and antimony source materials running out prior to the general laboratory shutdown earlier this year, device growth and fabrication were postponed past the scope of this dissertation. Future planned work includes pump-dependent PL studies of similar calibration quantum well structures to allay concerns about gain saturation in these long-wavelength operating type-I QWs, as well as growth and fabrication of the laser device structure depicted in Figure 3.12.

3.5 Summary

The work presented in this chapter dealt with pursuing highly-strained, high indium content materials in order to extend type-I laser emission up to and past 4 µm. By pushing the QW indium content up from 0.5 to past 0.7 and maintaining QW compressive strain ∼2.3%, type-I emission was pushed from 3 µm to 4 µm in QWs with GaSb barriers. Further attempts to increase the wavelength by pushing to 0.72 QW indium content resulted poorly performing QWs. To improve the luminescence efficiency as well as push to longer wavelengths, $Al_{0.3}Ga_{0.7}As_{0.03}Sb_{0.97}$ lattice-matched QW barriers were used, leading to restored type-I QW alignment and 3× greater peak PL and significantly narrowed spectral linewidth.

The work on highly-strained materials was leveraged to demonstrate a type-I diode laser emitting at 3.62 µm at 210 K. This is the longest wavelength emission from a type-I diode laser with GaSb barriers. A device design for room temperature operation at ∼4.1 µm was also proposed.

Chapter 4

Surfactant-aided Growth of Highly-strained Films

A key factor the growth of high quality materials is the growth mode of the film. The growth mode not only affects the quality of the growing layer, but also the quality of the interfaces. This is of particular concern for strained layer heterostructures such as lasers, where material and interface quality is of utmost importance. Strain due to the lattice mismatch of the film to the substrate causes a build up of energy as the film grows and can cause the growth mode to shift from 2D layer-by-layer (Frank–Van der Merwe) growth to 3D island formation (Volmer–Weber growth) and surface roughening which undesirably reduces interface and material quality. Consequently high strains limit the maximum thickness that epitaxial films can be grown while still maintaining high quality materials. One method for growing high quality highly-strained layers was discussed in Chapter 3. By lowering the substrate temperature during growth, the mobility of the impinging adatoms is kinetically limited, reducing the surface diffusion length and allowing for higher incorporated strains and indium fractions, while limiting indium segregation and outdiffusion from the strained layers. Another method of limiting the onset of island formation is to use an additional elemental species called a "surfactant" during growth that affects the adatom kinetics and promotes 2D layer growth. This chapter will discuss surfactant-aided growth in MBE, specifically focusing on the use of bismuth as a reactive surfactant to improve the growth of highly-strained III-V materials. By adding a bismuth flux during the growth of highly-strained GaIn(As)Sb materials, we were able to im-

prove the optical performance of these materials at layer thicknesses well beyond classical critical thickness limitations, indicating a potential method to improve optical performance of highly-strained materials and devices.

4.1 Surfactants in MBE

Surfactant-assisted MBE growth has become a useful tool in the growth of high quality epitaxial materials [110]. The term surfactant in the case of epitaxially grown materials refers to any species that does not readily incorporate into the growing film and instead segregates at the surface before desorbing. The presence of the surfactant modifies the surface free energies and alters the growth kinetics of adatoms, acting to either increase or decrease surface diffusion lengths. Massies and Grandjean proposed classifying surfactants into two catagories: nonreactive and reactive [111]. In their theory, nonreactive surfactants occupy interstitial surface sites and reduce the energy barrier for adatom hopping, causing an increase in surface diffusion lengths. This is the preferred surfactant mode for homoepitaxy. Examples of nonreactive surfactant species for III-V materials include group-IV elements such as tin and lead [112]. Reactive surfactants, on the other hand, sit on substitutional sites. Due to the segregating process an adatom exchange occurs where an impinging atom diffuses beneath the surface surfactant layer, preferentially taking the place of the surfactant atom on the substitutional site. The presence of the surfactant species above and the growing film around the diffused adatom limits further diffusion causing the surface diffusion length to decrease. This growth mode is preferred for heteroepitaxy of highly strained materials in order to suppress phase segregation and 3D island formation. Example reactive surfactants for III-V growth

are the larger group-V elements such as antimony and bismuth, as well as group-VI elements such as tellurium.

Surfactant-aided growth was first employed by Copel *et al.*, who added arsenic during the growth of strained Si/Ge films to change the surface kinetics of adatoms in order to suppress 3D island formation and promote layer-by-layer growth [113]. Germanium initially wets to the silicon (100) surface and grows in 2D layer-by-layer mode. After a few monolayers the strain energy from the lattice mismatch between germanium and silicon causes further germanium growth to happen in 3D island mode. This hybrid 2D-3D growth mode is called Stranski-Krastinov. The growth of silicon on germanium or silicon on germanium/silicon happens completely in 3D islanding mode from the start, as silicon does not wet to the germanium surface. By adding one monolayer of arsenic on the growth surface, the surface free energy is lowered by the arsenic adatoms donating one electron per surface arsenic atom in order to passivate the surface dangling bonds. This change to the surface energies alters the growth kinetics such to suppress 3D island growth, allowing for higher quality and thicker germanium-on-silicon films and silicon-on-germanium/silicon films [113], [114].

Turning to III-V materials, the group-V element antimony has been used as a reactive surfactant for growing highly-strained GaInAs [115] and to increase nitrogen incorporation in GaInNAs [116] and GaInNAsSb [117]–[122] for quantum well lasers on GaAs. Under typical III-V growth conditions, however antimony does not always remain surface segregated, particularly for GaSb-based materials, making it not a suitable option here.

4.2 Bismuth as a surfactant

Bismuth, the next larger group-V element, has proven to be quite versatile as a surfactant species. Owing to its large size and low electronegativity, incorporation of bismuth has proven difficult across most growth conditions [123]–[125]. Bismuth has been employed as a surfactant to maintain smooth epitaxial surfaces [124], [126], [127], increase substitutional nitrogen incorporation in dilute nitride materials [123], [128], and improve material quality of highly-strained layers [8], [129].

As a reactive surfactant, bismuth has the effect of reducing adatom mobility and reducing the surface diffusion length. In the case of highly-strained layers, this can promote layer-by-layer growth in metastable III-V alloys by kinetically limiting the growth process and delaying epitaxial quality issues imposed by thermodynamic constraints such as strain relaxation [110], [123], [128], [129].

4.3 Growth enhancement of highly-strained mid-infrared emitters using bismuth as a surfactant

As previously discussed, highly-strained heterostructures have several properties that make them advantageous for mid-infrared optical emitters,including improved valence band offset, better valence band structure, and increased split-off bands. The latter feature decreases parasitic Auger effects, which is especially problematic in low-band gap materials where the radiative transition energy is on the same order as the gap between the valence band edge and the split off band. Compressive strain has the effect of breaking the light-hole and heavy-hole valence band degeneracy, pushing the heavy hole band up. This can improve the overall valence

alignment of strained QWs with the barrier material, improving valence band offset and hole confinement toward type-I emitters.

As noted in Chapter 3, there are limitations to how much strain can be incorporated into a heterostructure before defect formation and relaxation sets in. A key hurdle to growing highly-strained GaInAsSb materials of good optical quality is the strain-driven surface segregation of indium [109]. This process can cause roughening at the QW/barrier interface and leads to the inevitable formation of defects that degrade optical quality. Cold substrate growth temperatures help some by promoting better indium incorporation during crystal growth. With a look toward mitigating this issue, we investigated bismuth as a surfactant species in the growth of GaIn(As)Sb materials, namely by exploring if bismuth as a reactive surfactant could promote layer-by-layer growth in highly strained metastable III-V material systems by kinetically-limiting the growth process. Using bismuth as a reactive surfactant agent can also suppress indium segregation by limiting the surface diffusion length and promoting indium incorporation, leading to improved structural and optical quality at higher compressive strains [129]. For this study, samples were grown after the fashion discussed in Chapter 3. Following thermal deoxidation at 550 °C, growth was initiated with a 100-nm GaSb buffer layer was grown at 475 °C. A 100-nm GaSb buffer layer was grown as the substrate temperature was ramped down to an actual temperature of 350 °C and stabilized prior to growth of the strained layers. Strained test layers were grown with thicknesses near to and exceeding the critical thickness limit as calculated using the method of Matthews and Blakeslee [130]–[132]. These strained layers were covered with a 100-nm GaSb capping layer, also grown at 350 °C. The next two sections detail the results of our investigations on

the effects of a bismuth flux on the material and optical quality of strained GaInSb and GaInAsSb layers.

4.3.1 GaInSb

In order to study the effects of bismuth as a surfactant on highly strained materials we first grew $Ga_{0.53}In_{0.47}Sb$ samples at several thicknesses, both with and without a 0.05 ML/s bismuth flux applied during the growth of the GaInSb layer. We chose this alloy to be able to investigate the effects of the surfactant on material quality while limiting the potential interaction effects due to multiple anions, such as the As-for-Sb exchange rate, which could be altered by the presence of the surfactant species and alter the strain measurements.

GaInSb strained layers (2.95% compressive strain) were grown on (001)-oriented GaSb substrates at 350 °C with thicknesses of 6, 7, and 10 nm. The 6-nm and 7-nm samples were just below and above the Matthews–Blakeslee (M–B) critical thickness, while the 10-nm samples were $\sim$1.6$\times$ the M–B limit. Both sets of samples, grown with and without the bismuth flux, showed monotonically decreasing PL efficiency as the ternary layer thickness was increased (Figure 4.1). GaInSb layers grown close to the critical thickness limit also showed a noticeable decrease in PL intensity between samples grown without and with a bismuth flux, suggestive of a adverse effect on growth quality due to the surfactant species. However, the 10-nm wide GaInSb layers exhibited less PL degradation when grown with the surfactant bismuth compared to the bismuth-free sample. Thus while perhaps the bismuth surfactant does not inhibit material degradation near the critical thickness limit, and in fact appears to cause additional optical quality degradation, it appears that perhaps for thicker strained layers the presence of the surfactant does inhibit material

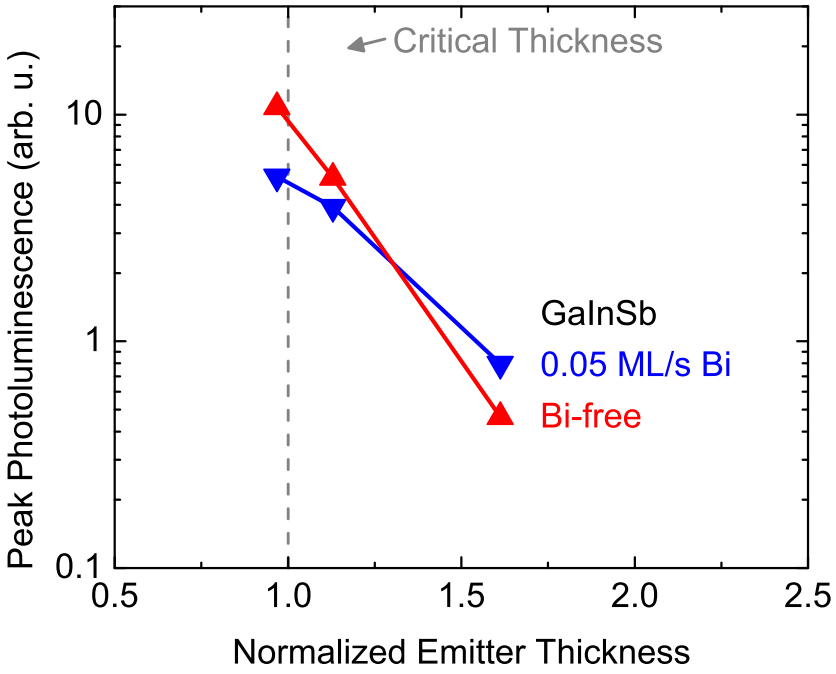

Figure 4.1: Peak room-temperature photoluminescence emission from strained GaInSb layers as the layer thickness is increased. Near the Matthews-Blakeslee critical thickness limit, the control samples grown without a bismuth flux exhibited brighter photoluminescence. The rate of photoluminescence decay was less for layers grown with a 0.05 ML/s bismuth flux, resulting in the samples with the thickest layers emitting more brightly than the bismuth-free layers beyond the critical thickness limit.

degradation somewhat. Of note, the slope of the PL degradation for those samples grown with a bismuth flux is nearly half that of the bismuth-free growths, pointing to the inhibited material quality decay due to the presence of the bismuth flux.

4.3.2 GaInAsSb

We also examined the effect of a bismuth flux on strained GaInAsSb layer quality as critical thickness is reached and exceeded. GaInAsSb epitaxial layers were grown with thicknesses at and above the M–B critical thickness limits. The Ga:In ratio

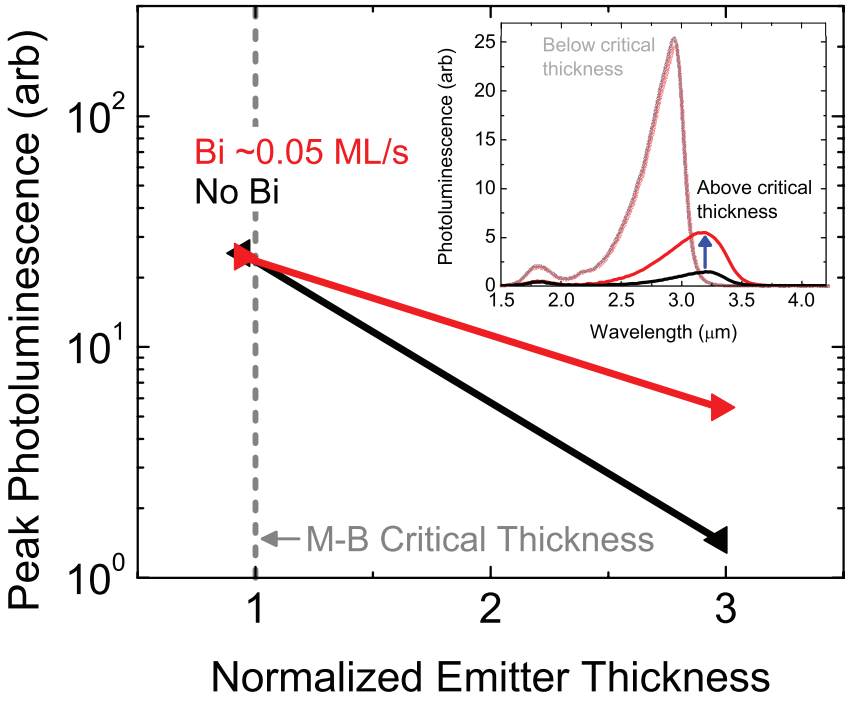

Figure 4.2: Peak room-temperature PL intensity of strained GaInAsSb QW structures, with thicknesses at and above Matthews–Blakeslee critical thickness limit, decayed overall as the critical thickness limit was exceeded. However the rate of decay was less for layers grown with a 0.05 ML/s incident bismuth flux, allowing thicker bismuth-enhanced material to emit 3.75× more brightly than comparable non-bismuth affected material. The peak emission wavelength shift observed in the PL spectra (inset) is attributed to the change in quantum confinement energy with layer thickness.

of the quaternary alloy was set to be ∼1, and the overall alloy was designed for a 10-nm QW to have a PL peak at a wavelength of ∼3 µm. The strained layers were grown at 350 °C, at 1 ML/s, at thicknesses of 10 and 31.5-nm (∼1× and ∼3× M–B critical thickness), and had a compressive strain of 1.9%. For samples grown with a bismuth flux, bismuth was supplied at a rate of 0.05 ML/s, about 5% of the overall incident group-III flux.

For GaInAsSb layers grown close to the critical thickness limit, the bismuth flux applied during crystal growth did not affect the optical quality of the grown materials. There was no significant difference in PL emission spectra (Figure 4.2, inset) when comparing samples with and without bismuth. As the strained layer thickness was increased, exceeding the critical thickness, a general degradation of the optical quality was observed, as evidenced by reduced PL emission. However, the use of bismuth during growth of thicker layers inhibited the PL decay, allowing the layers grown in the presence of bismuth to emit more brightly than the layers grown without bismuth. At 3× the M–B critical thickness limit, the resulting peak PL intensity for GaInAsSb material grown with a bismuth flux was 3.75× brighter than material grown without bismuth.

Atomic force microscopy (Figure 4.3) and HR-XRD (Figure 4.4) measurements showed good crystal and interface morphology. Reciprocal space mapping about the GaSb (224) diffraction peak, shown in Figure 4.5, confirmed that both of the thick epitaxial layers were coherently strained to the substrate, as evidenced by the alignment of substrate and layer peaks at the same in-plane reciprocal lattice axis. Transmission electron microscopy (TEM) measurements showed no detectable misfit dislocations in samples less than the critical thickness. For the thicker samples TEM showed only occasional misfit dislocations that were not dense enough to obtain reliable statistics on their occurrence or formation. Electron channeling contrast imaging (ECCI) was employed with these samples in order to obtain a better measure of the crystal structure, as it affords a wider scan area than TEM. Figure 4.6 shows ECCI of the 3× critical thickness samples. Primary and secondary slip were observed in both samples. Adding bismuth to the incident flux led to a drop in the misfit dislocation density in both the in-plane (1.5×10^3 cm^{-3} to 1.3×10^3 cm^3)

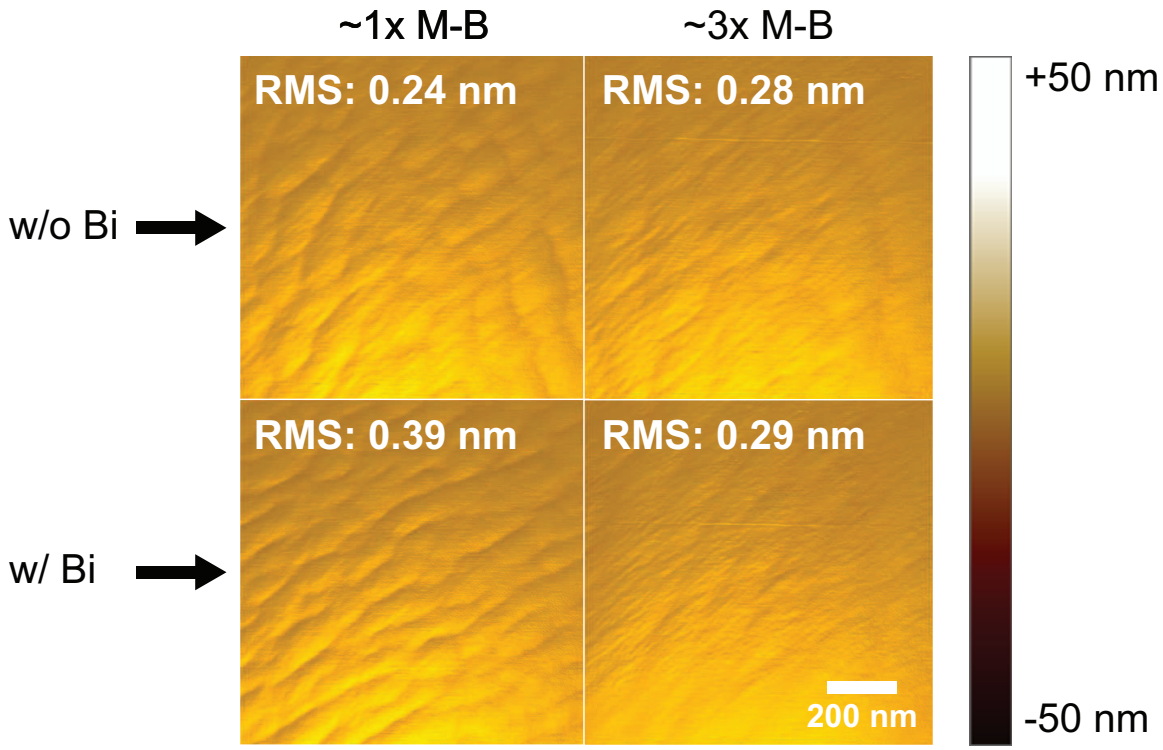

Figure 4.3: Atomic force microscopy scans of strained GaInAsSb QW structures grown either without or with a bismuth flux exhibit very little surface roughness even when grown well beyond the critical thickness.

and out-of-plane (6.0×10^3 cm^3 to 2.3×10^3 cm^3) directions. The plastic relaxation was reduced by half in the bismuth-aided sample, dropping from 0.015% to 0.007%. These results point to improved crystalline structure when bismuth is used during growth of strained GaInAsSb layers and are consistent with the higher measured PL from the bismuth-enhanced material, indicative of overall higher optical quality

4.4 Summary

In this chapter we explored the use of bismuth as a reactive surfactant in the growth of highly strained GaIn(As)Sb materials. Specifically, we attempted to use the surfactant species to promote higher quality 2D layer-by-layer growth in these

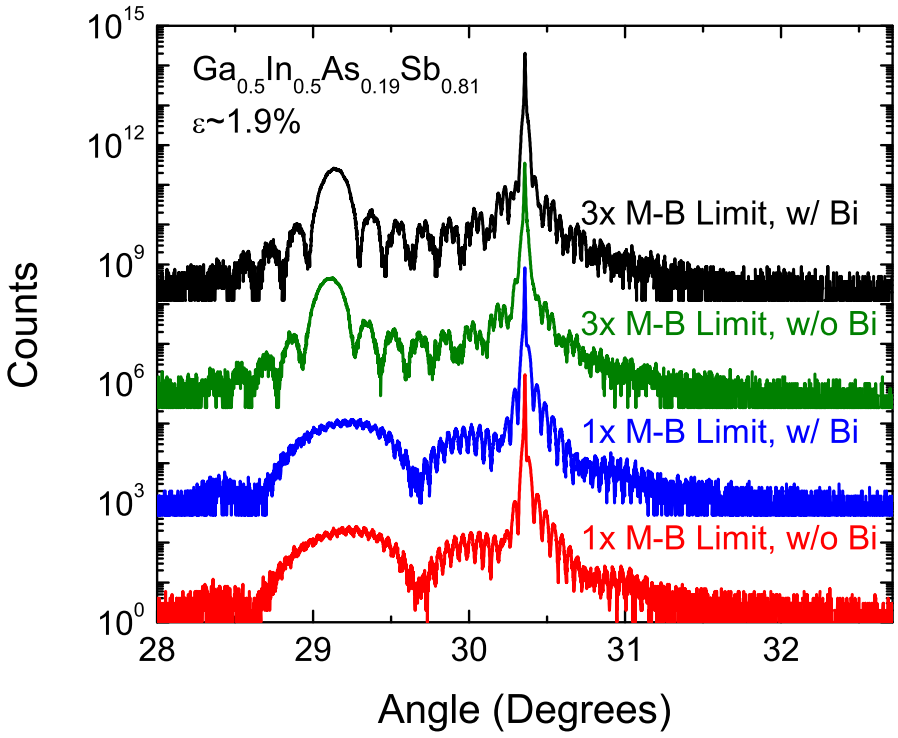

Figure 4.4: Well-formed layer fringes in HR-XRD ω-2θ scans about the GaSb (004) diffraction peak are indicative of well-formed layers and unrelaxed heterointerfaces.

materials in order to circumvent limitations due to strain and critical thickness. The ability to grow quality thicker strained layers opens up an additional avenue to push optical emission in these materials to longer wavelengths. In the case of laser active regions, highly-strained multi-QWs could be leveraged for improved active region confinement factors and higher differential gain. While overall optical quality declined for all samples as the critical thickness was exceeded, those samples grown with a bismuth flux applied during growth of the highly-strained layers exhibited noticeably less degradation of optical performance. While these results are preliminary, they demonstrate a potential path whereby the addition of a surfactant bismuth flux can reduce the formation of defects and dislocations during the growth of strained

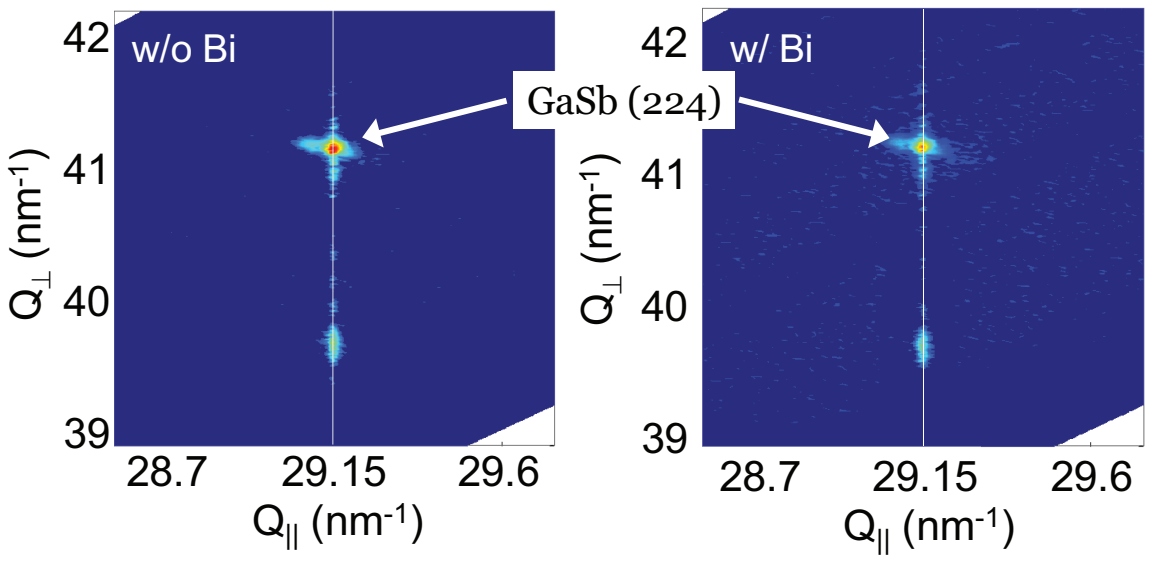

Figure 4.5: Reciprocal space maps about the GaSb (224) peak show that the 31-nm strained GaInAsSb layer is coherently strained to the substrate with and without using the bismuth surfactant. The thin white lines through the substrate and layer peaks are guides to indicate the level of strain coherence.

III-V materials grown beyond conventional critical thickness limits, leading to higher quality optical materials with thicker strained regions. Further studies are necessary to better understand the defect changes due to the surfactant as well as to better explore the growth space for surfactant-assisted growth of highly-strained materials, such as the amount of surfactant surface coverage necessary.

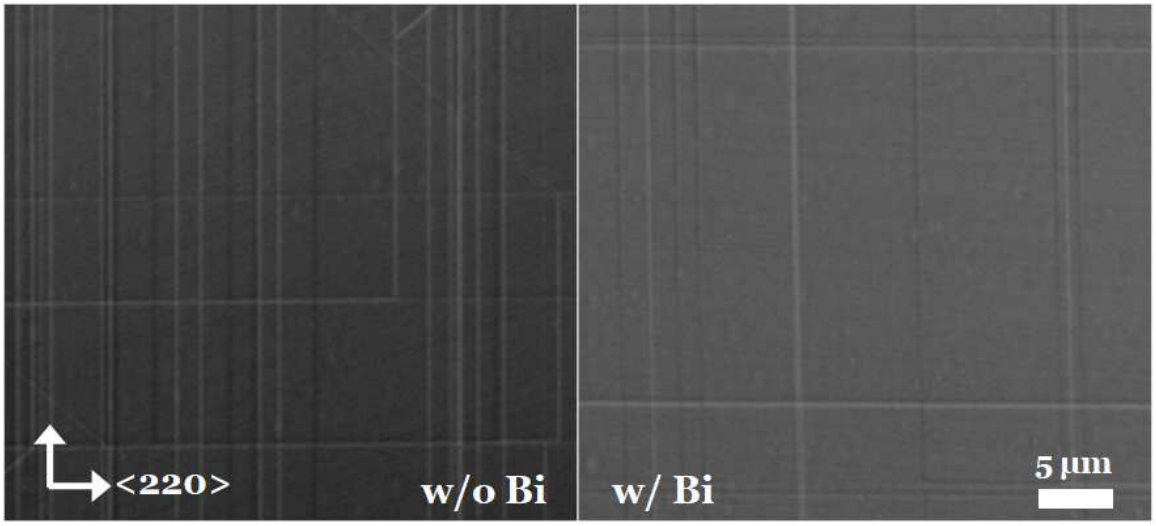

Figure 4.6: Electron channeling contrast images of GaInAsSb samples at 3× the M–B critical thickness grown without (left) and with (right) bismuth. The sample grown with bismuth exhibited comparatively reduced misfit dislocation density in both the in-plane and out-of-plane directions, and the plastic relaxation was reduced by half with respect to the sample grown without bismuth.

Chapter 5

Dilute Bismide Alloys for Mid-infrared Optical Materials

In Chapter 4, we explored the use of bismuth as a reactive surfactant species during the growth of highly-strained mid-infrared III-V materials in order to improve the optical quality of these materials. While there was no observable effect to the optical quality of GaInAsSb/GaSb samples grown near to the Matthews-Blakeslee critical thickness limit, with and without a bismuth flux, for samples grown beyond the Matthews-Blakeslee critical thickness limit, the presence of a bismuth flux during growth resulted in improved material quality compared with samples grown without a bismuth flux. However, despite comparative improved performance we still observed overall degradation in material quality as the critical thickness limits were exceeded.

The low growth temperatures we employ in order to grow high quality highly strained materials, as discussed in Chapter 3, also opens a pathway to the potential to incorporate bismuth as a constituent material in our mid-infrared alloys. Combining bismuth with III-V alloys results in interesting effects to the material properties that can be utilized for applications in the mid-infrared. The following sections give an overview of dilute bismide materials and their properties, and presents our work on bismuth incorporation in III-V-Bi materials, specifically GaSbBi and GaInAsSbBi.

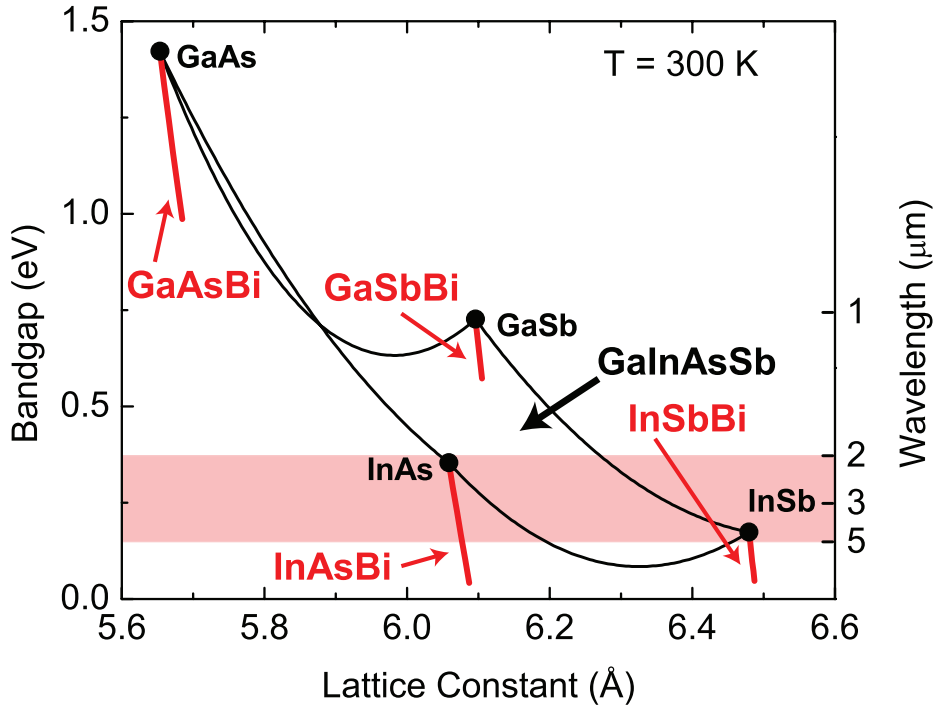

Figure 5.1: Room-temperature band gap energy as a function of lattice parameter for III-V-Bi ternary materials containing up to 5% bismuth. The dilute bismide ternaries exhibit much stronger band gap reduction as a function of lattice parameter expansion compared with (GaIn)(AsSb)-based ternaries.

5.1 III-V-Bi semiconductor alloys

The dilute bismides constitutes a class of III-V materials with small concentrations of bismuth atoms in the III-V alloy. There has been considerable interest in the dilute bismides due to their interesting and useful properties [133]. Like the dilute nitrides, the dilute bismides exhibit abnormally large band gap reduction for small concentrations of bismuth but with only a slight shift in lattice constant [134]. This is illustrated in Figure 5.1. Two other advantages of the dilute bismides over the dilute nitrides are a relatively temperature-independent band gap [135] and much less electron mobility degradation [136], [137]. The former is appealing as a potential path toward more temperature-insensitive emission from laser diodes. Due to the

large band gap reductions, up to 1.2 eV per 1% of compressive strain, dilute amounts of bismuth alloyed within the (GaIn)(AsSb) material system provides the potential of further mid-infrared device development apart from highly-strained materials.

5.2 Valence-band anti-crossing model

For many III-V alloys the electronic properties are determined using the virtual crystal approximation (VCA) by linearly interpolating between the constituent endpoint materials. Slight deviations due to alloy disorder effects are accounted for with an experimentally determined bowing parameter. This model holds well for "well-matched " alloys whose endpoint materials have only small differences in their properties. For other so-called highly-mismatched alloys the band anticrossing model was developed to describe the variant behavior observed in these material systems [138]. Two such highly-mismatched alloy systems are the dilute nitrides and the dilute bismides. While both exhibit large band gap narrowing and band bowing, the two systems are in a sense opposites in how the band gap narrowing comes about. Elements that sit on anion sites with large electronegativties, such as nitrogen, introduce a localized defect state that interacts with the conduction band edge of the III-V host matrix and splits the conduction band, with one split band trending downward lowering the conduction band edge [139]. Bismuth, on the other hand, having both a larger atomic radius and being less electronegative, forms its impurity level in the valence band of the III-V host matrix, which ultimately pushes the valence band edge up [140]. The large band bowing can be utilized to access smaller band gaps for comparably less strain mismatch in conventional GaInAsSb alloys, reducing the need for QW arsenic content to mitigate high strains. The interaction of the bismuth atom with the spin-orbital states also moves the split-off band down in

energy, which when tied with the large upward push of the valence band edge leads to large spin-orbit splitting that can aid in the suppression of Auger processes involving the split-off band [133], [141]–[144]. In fact, both GaAsBi/GaAs [145] and GaInAsBi/InP [146] exhibits spin-orbit splittings that exceed the transition energy.

5.3 MBE growth of dilute bismide III-V alloys

Incorporation of bismuth into III-V materials is difficult due to its large atomic size. Bismuth tends to surface segregate instead of incorporate into the growing film. At typical III-V growth temperatures, the segregated bismuth ultimately desorbs from the surface. This feature is useful for growths where bismuth is employed as a surfactant, as discussed in Chapter 4. Reducing the substrate temperature to inhibit desorption unfortunately often results in the formation of bismuth droplets on the semiconductor surface, reducing material quality. Droplet-free epitaxy can be realized by reducing the V:III ratio to near-stoichiometry [147]–[149]. Using these growth conditions, GaSbBi alloys with bismuth content up to 14% and room-temperature photoluminescence out to 3.8 μm have been reported [149], as well as GaSbBi/GaSb laser diodes operating in cw at 2.5 μm at 80 K and pulsed at 2.7 μm at room temperature [150].

The next two sections will detail our work on bismuth incorporation into GaSbBi alloys and GaInAsSbBi alloys. The former was used as a test bed for growth parameters of dilute bismide growth, while the quinary system was targeted for potential laser active region development at ∼4 μm.

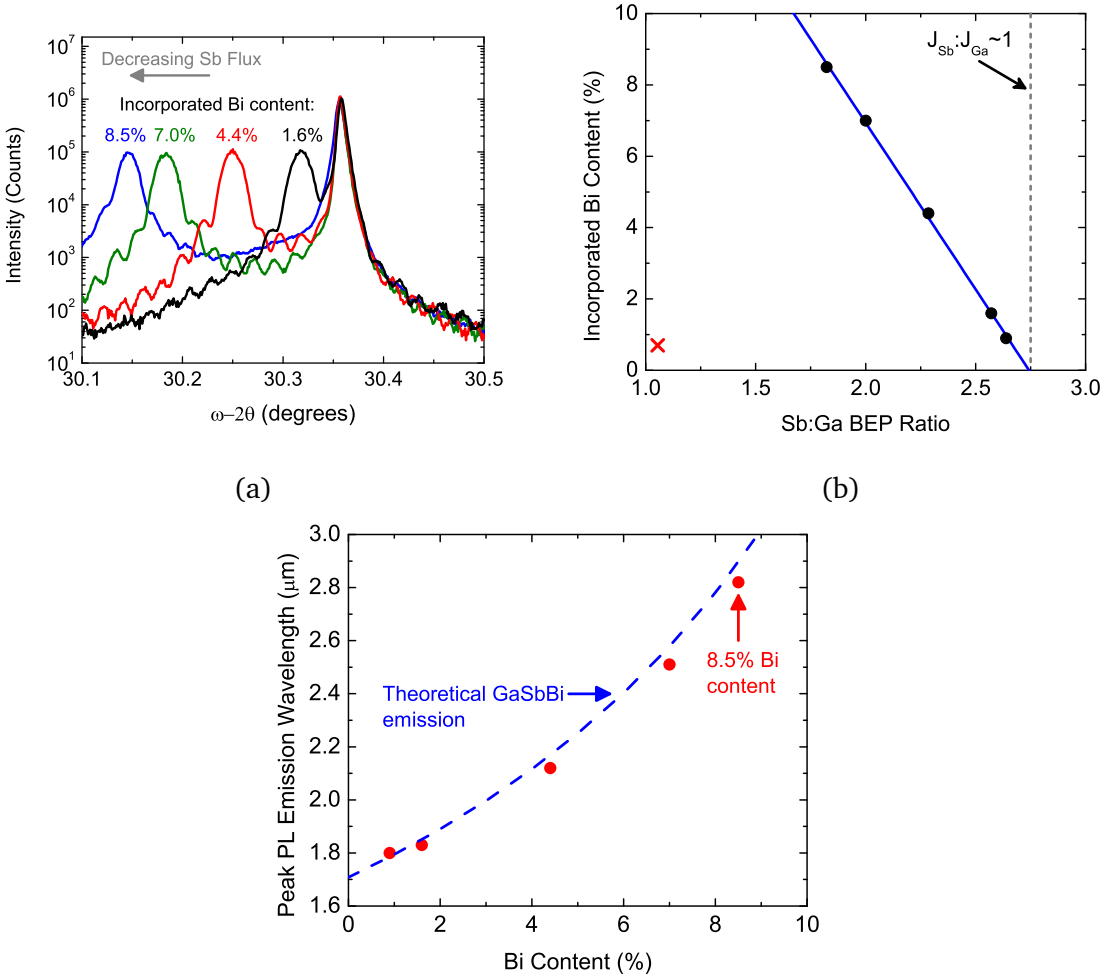

Figure 5.2: Summary of results of bismuth incorporation into GaSbBi films. (a) HR-XRD of 250-nm GaSbBi films with bismuth content up to 8.5%. (b) Bismuth incorporation increased inversely with the Sb:Ga BEP ratio as the ratio was dropped below the 1:1 flux ratio, as determined from Sb-limited RHEED oscillations. Samples up to 8.5% bismuth content were droplet-free. The sample indicated by the red 'x' had droplet formation. (c) Peak PL emission wavelength follows the theoretical emission given by [98].

5.3.1 GaSbBi

GaSbBi has been successfully grown with up to 14% bismuth [149]. In fact, GaSbBi/GaSb lasers with 12% bismuth content have been demonstrated emitting at 2.7 µm [150]. For other dilute bismide-antimonide materials, the amount of bismuth incorporation is very small: only 2.4% bismuth in InSbBi [151], up to 10.5% bismuth in GaInSbBi [152], and only one report for bismuth incorporation in GaInAsSbBi alloys [153].

For this work, GaSbBi presented the most straightforward alloy system to pursue with the goal of incorporating bismuth into mid-infrared emitters targeting 4 µm. GaSb is used as the substrate for the other materials and device development in this dissertation, and by only trying to add bismuth to the binary it presented the least variables to control for in the experiment. Using similar growth parameters to those used for the highly-strained, high indium content quantum wells discussed in Chapter 3, 250-nm thick GaSbBi layers were grown by MBE on UID GaSb (001) substrates. However, just growing at low substrate temperatures was not sufficient for bismuth incorporation. In addition to low substrate growth temperatures, the key to successful bismuth incorporation for this material was reducing the Sb:Ga flux ratio below 1. Using this growth parameter space, bismuth was successfully incorporated into GaSbBi films with measured bismuth contents up to 8.5%.

The GaSb growth rate was set to 0.5 ML/s, while the Bi:Ga flux ratio was set to ∼1:10. As depicted in Figure 5.2b, bismuth incorporation was promoted by reducing the Sb:Ga flux ratio, as measured by Sb-limited RHEED oscillations on GaSb, below 1. This points to a potential antimony-for-bismuth exchange reaction happening, akin to the arsenic-for-antimony exchange reaction [74], [75]. If antimony was supplied at a rate at least equal to the gallium flux, bismuth was not incorporated. Bis-

muth incorporation happened when the growth was antimony-starved. The amount of bismuth increased proportionally to decrease of the incident Sb flux. All the samples save one, indicated by the red 'x' in Figure 5.2b, were droplet free. The outlier sample was grown with a very low antimony flux, and did not have enough incident group-V flux to maintain stoichiometry and became gallium-rich. The bismuth content of the GaSbBi layers was determined by fitting to HR-XRD measurements (Figure 5.2a), assuming a GaBi lattice constant of 6.272 Å [154]. The strain for the highest bismuth content was only 0.25%. The peak room temperature photoluminescence emission wavelength from these GaSbBi films (Figure 5.2c) also tracked the predicted bandgap for $GaSb_xBi_{1-x}$ as given by [98]. At the highest bismuth content (8.5%), the emission peak wavelength had red-shifted from the GaSb emission peak wavelength by over 50%.

5.3.2 GaInAsSbBi

Studies of bismuth incorporation were also performed on candidate mid-infrared laser active regions emitting between 3.6 and 4 microns. These materials have high indium contents between 66 and 71 percent and are compressively strained between 2.3 to 2.5%. Following the low-temperature growth parameters developed, 10- and 11-nm QWs with GaSb barriers were grown by MBE at 350 °C (Figure 5.3a). Bismuth was supplied during select growths up to 0.15 ML/s. For moderate levels of bismuth flux, the QWs showed PL enhancement up to 34% in materials emitting at 3.6 µm (Figure 5.3b). A similar 25% PL enhancement was seen for QWs emitting at 3.9 µm, albeit at a lower Bi flux. The enhancement observed in the bismuth-affected rolled off at lower bismuth applications for quantum wells with higher indium content, operating at longer wavelengths. This may be due

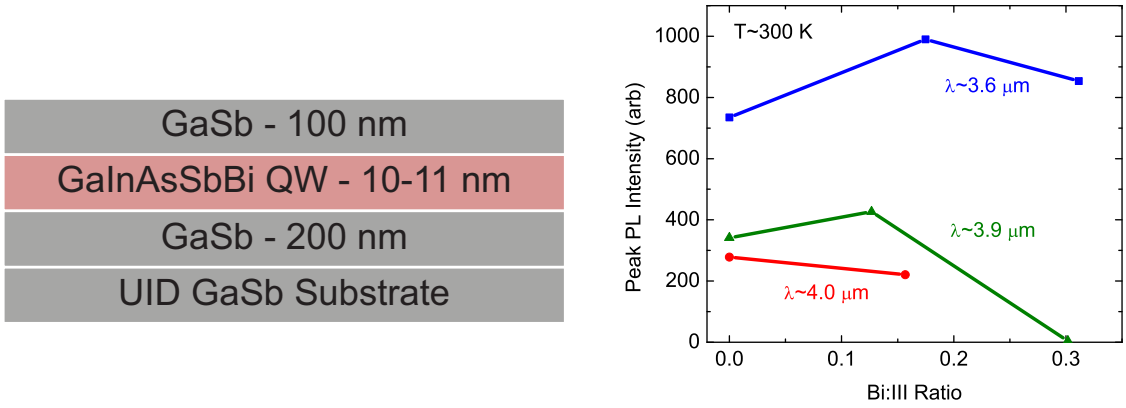

(a) (b)

Figure 5.3: (a) Epitaxial layer stack of GaInAsSb(Bi) samples reported. (b) Peak photoluminescence from mid-infrared quantum wells exhibiting changes to emission due to bismuth incorporation in quinary GaInAsSbBi alloys For moderate bismuth fluxes applied during growth, the photoluminescence is enhanced. Higher incident bismuth flux resulted in decreased photoluminescence emission, likely due to the onset of bismuth droplet formation [153].

to a bismuth solubility limit in materials with higher indium content, as has been observed in GaInSbBi alloys [152]. The QW alloys for the bismuth-free materials were determined from fitting to HR-XRD measurements. These measurements show well-resolved QW peaks and strong Pendellösung fringes indicative of well-formed heterointerfaces, as well as non-negligible shifts in the QW compressive strain toward lower strains for the bismuth-affected growths.

QWs with peak PL emision at 3.6 μm and containing indium concentrations of 0.66 were grown at 350 °C with GaSb barriers. The bismuth-free control alloy ($Ga_{0.34}In_{0.66}As_{0.24}Sb_{0.76}$) had 2.51% compressive strain. Bismuth employed during QW growth enhanced PL emission compared to the bismuth-free control. For a higher bismuth flux, the enhancement diminished indicating a window within which

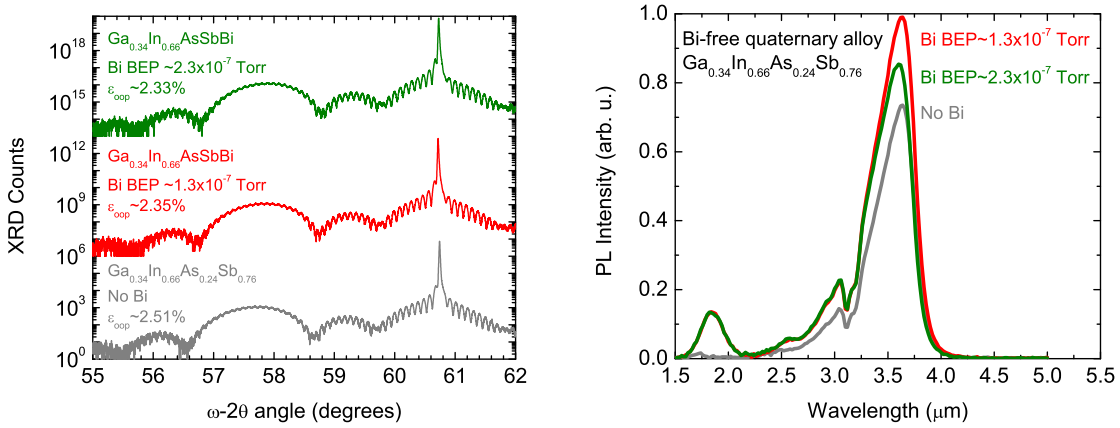

(a) (b)

Figure 5.4: (a) For QWs with 66% indium emitting at 3.6 microns, bismuth incorporation resulted in a decrease in compressive strain for samples with bismuth content up to 3%, as indicated by the shift of the QW layer peak in HR-XRD ω-2θ scans about the GaSb (004) peak. (b) Peak photoluminescence was enhanced up to 34%. Despite the observed strain shift, the photoluminescence emission peak wavelength did not appreciably shift.

bismuth provides a positive enhancement. Peak PL improved by >34% (Figure 5.4b) while QW compressive strain was reduced by 6% (Figure 5.4a). Photoreflectance measurements (Figure 5.5a) showed strengthening of the 11H transition resonance indicative of improved hole confinement due to enhanced valence band offset. Several steps were used to determine the elemental fractions of the quinary GaInAsSbBi alloy. First, the gallium and indium fractions were assumed to be unchanged from the 0% bismuth control, as the group-III atoms have unity sticking coefficients. Using dynamic fitting of the HR-XRD measurements, and varying bismuth content as a input variable, the arsenic and antimony fractions were adjusted to match the diffraction scan. Then following the procedure given in [155], the QW transition energies are calculated as a function of QW bismuth content using the set of As:Sb:Bi

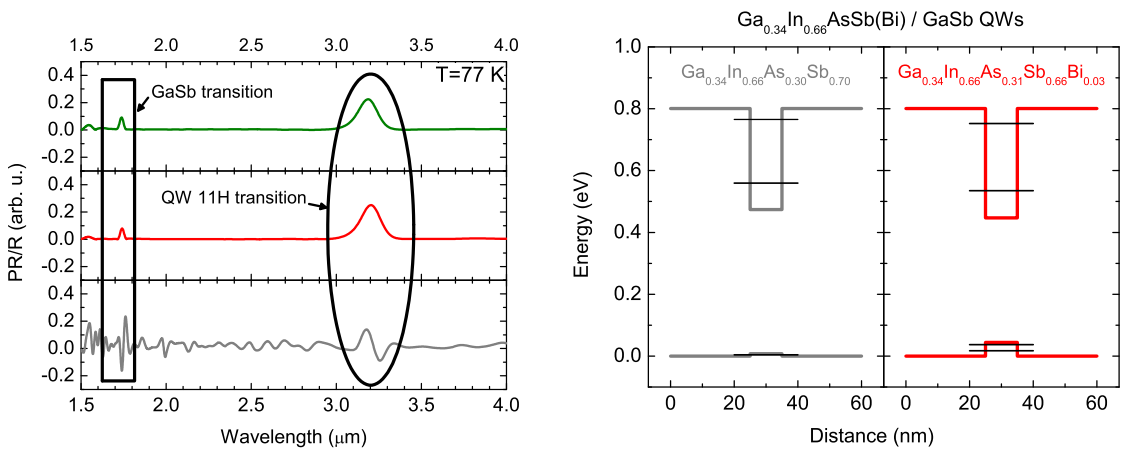

(a) (b)

Figure 5.5: (a) Photoreflectance measurements of $Ga_{0.34}In_{0.66}AsSb(Bi)$ materials emitting at 3.6 microns, showing the 11H transition strengthening in the samples that incorporate bismuth. (b) Calculated band diagrams of bismuth-free and bismuth-enhanced $Ga_{0.34}In_{0.66}AsSb(Bi)/GaSb$ quantum wells with peak photoluminescence at 3.6 μm, illustrating the valence band offset enhancement due to bismuth incorporation.

ratios derived from XRD fitting. Matching these calculated energies to those energies measured from photoreflectance yields the incorporated bismuth content, as well as the proportions of incorporated As and Sb. A bismuth content of ∼3% was obtained using this method, resulting in a net increase of the valence band offset by 36 meV to 44 meV (Figure 5.5b). The calculation also yielded an increase in the incorporated As fraction of ∼1%, pointing to the possibility of the As-for-Sb exchange ratio [156], [157] being augmented by Bi during growth. Finally, using the extracted energy levels and semiconductor alloy, possible band diagrams were calculated that matched the derived confinement energies using a finite particle-in-a-box model (Figure 5.5b). Of note, the QW treated with the higher bismuth flux that showed reduced enhancement also was fitted to have ∼3% bismuth content.

As its strain and PL emission are similar, the reduced efficiency may point to non-substitutional bismuth clusters forming in the semiconductor.

At 3.9 µm, bismuth enhancement resulted in a 25% increase in peak PL. Highly-strained 11-nm QW structures were grown on (001)-oriented GaSb substrates at a substrate temperature of 350 °C. Samples containing varying numbers of QWs (ranging from one to seven) with a maximum compressive strain of 2.5% were grown both with and without bismuth. The bismuth flux was swept from 0 to 0.12 ML/s, up to nearly 10% of the overall quaternary III-V flux. As shown in Figure 5.6a, a moderate bismuth flux of ∼0.05 ML/s improved the peak PL efficiency of multi-QW structures by 25% compared to samples grown without bismuth. Equivalent single-QW structures did not exhibit the marked difference in PL as the multi-QW structures. The bismuth-containing material maintained the higher performance across the swept temperature range. The structures exhibited well-resolved peaks and Pendellösung fringes in HR-XRD ω-2θ scans, shown in Figure 5.6c, indicative of high-quality interfaces. However, nominally-identical structures grown with higher bismuth fluxes (0.12 ML/s) exhibited no PL (see Figure 5.6a) and had significantly degraded structural quality (see Figure 5.6c). Comparison of reciprocal space maps (Figure 5.7) of the control sample grown without bismuth and the sample grown with 0.05 ML/s bismuth shows the onset of relaxation in the bismuth-free structure, while the material grown with bismuth maintains coherence to the substrate, leading to improved material and optical quality.

Atomic force microscopy (AFM) measurements of the surface roughness, in the left pane of Figure 5.8a, show very smooth epitaxial surfaces for the bismuth-free and the bismuth-enhanced samples. For the degraded sample, AFM measurements show surface droplets approximately 0.1 µm wide. In the right pane of Figure 5.8a,

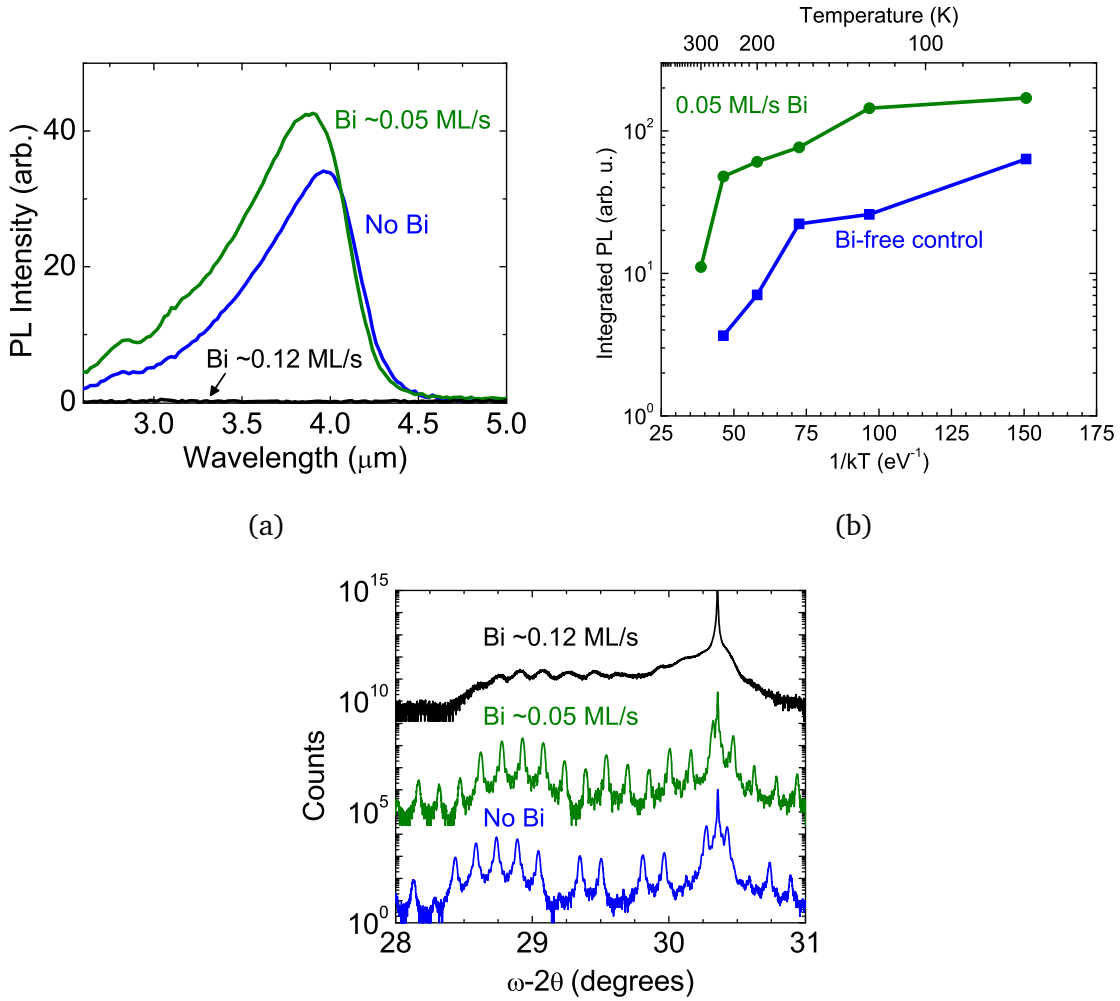

Figure 5.6: (a) For low levels of bismuth flux (∼0.05 ML/s) during QW growth, the peak room-temperature PL emission intensity increased by 25%. Emission degraded rapidly with increased bismuth flux (∼0.12 ML/s) during growth. (b) Temperature-dependent integrated PL shows reduced quenching in the dilute-bismide sample, consistent with improved hole confinement in the quantum wells. (c) HR-XRD ω-2θ scans of multi-QW structures show well-defined layer interfaces and QW superlattice peaks for lower fluxes of bismuth. Samples grown with higher bismuth fluxes exhibited significantly degraded QW interfaces.

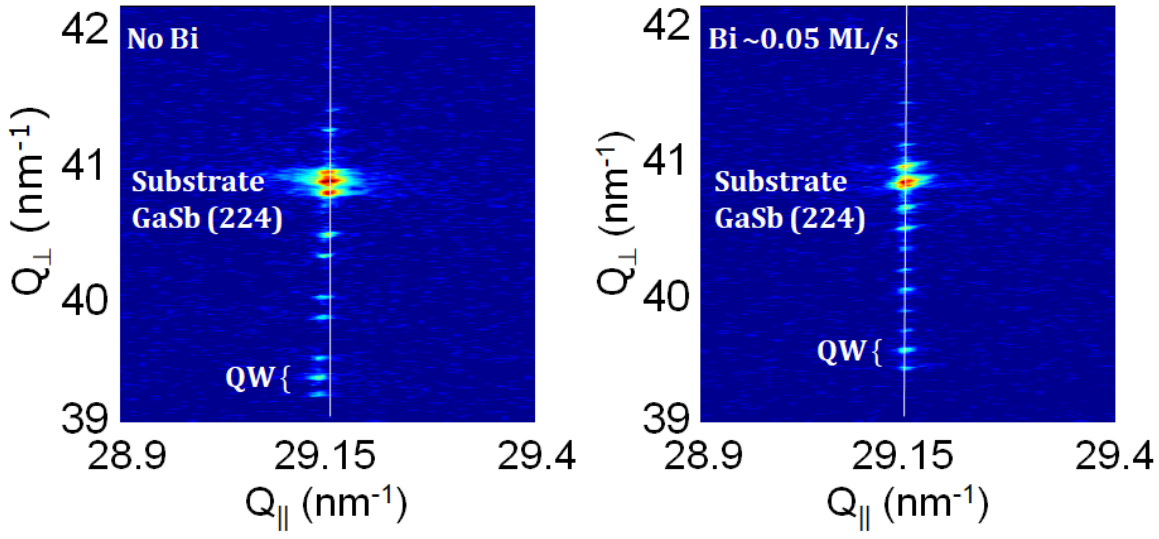

Figure 5.7: Reciprocal space mapping, about the GaSb (224) diffraction peak, of multi-QW structures grown without (left) and with (right) bismuth. The vertical thin white lines are a guide to the eye. The diffraction peaks in the sample grown without bismuth exhibit slight tilt from the vertical guide, indicative of a slight strain relaxation. The peaks of the sample grown with bismuth, on the other hand, shows no observable deviation from vertical, indicative of good coherence with the substrate.

secondary ion mass spectroscopy (SIMS) analysis of the superficial layers of these samples revealed high concentrations of bismuth compounds at the surface and in the capping layer of the roughened sample, while the smooth samples did not. SIMS was performed on the QW regions of the bismuth-free control and the bismuth-enhanced emitter, Figure 5.8. Here, bismuth-containing compounds were evident in the QW of the enhanced material but not in the control.

Photoreflectance measurements (Figure 5.9a) indicated only one confined state in the bismuth-free 3.9 µm emitter. For the bismuth-enhanced QW, three resonances were measured in photoreflectance, indicating strong valence band enhancement. Following the same procedure for alloy determination as before for the 3.6

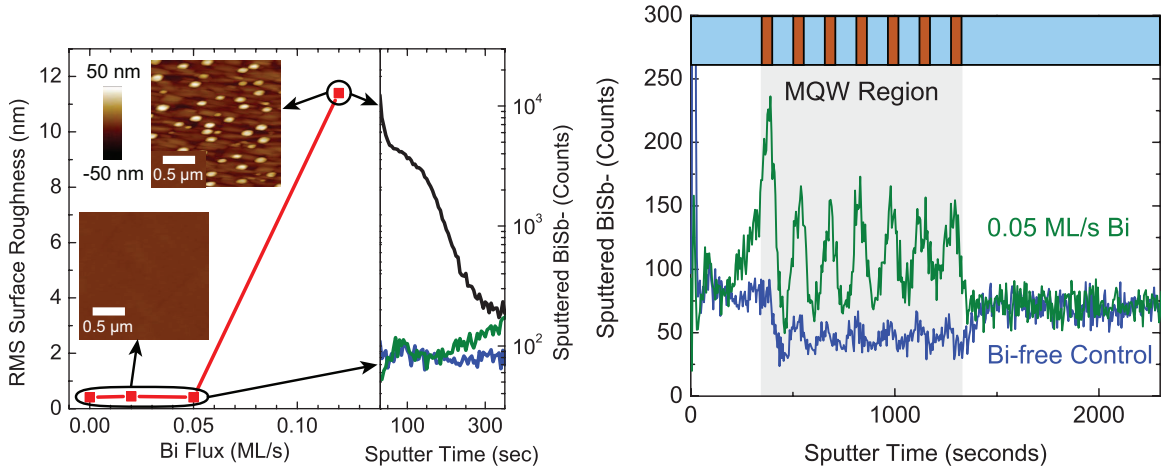

(a) (b)

Figure 5.8: (a) (left) RMS surface roughness as measured using AFM was between 0.41 and 0.45 nm for the strong emitters. At 0.12 ML/s bismuth deposition the surface roughness was 11.4 nm and bismuth droplets had formed. (right) SIMS measurements of the superficial 120-nm GaSb layer, showing significant bismuth content in the roughened sample. (b) SIMS measurements showing counts of BiSb- in a multi-QW structure grown with a 0.05 ML/s bismuth flux during the QW growth, along with an otherwise identical bismuth-free control. Bismuth concentrations well above the noise floor were observed in the sample with the applied bismuth flux.

μm emitters, the bismuth fraction in the enhanced QW was found to be ∼3%. The arsenic fraction also increased, this time ∼2% more to a concentration of 0.31. Finite particle-in-a box calculations (Figure 5.9b) based on the measured PR energy levels yielded an enhanced quantum well with a valence band offset of 56 meV.

5.4 Summary

As a constituent, bismuth has the potential to both reduce the material band gap and enhance the valence band offset. Leveraging the growth conditions developed for high-strain, high indium-containing QWs, we successfully grew droplet-free dilute bismide materials. Bismuth content up to 8.5% was incorporated into GaSbBi

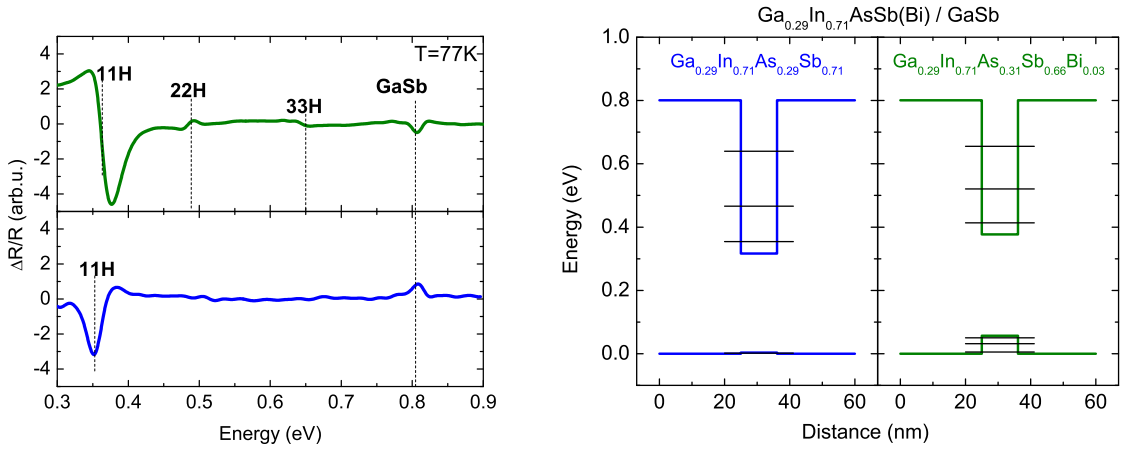

(a) (b)

Figure 5.9: (a) Comparative photoreflectance spectra of multi-QW samples measured at 77 K. The measured photoreflectance from $Ga_{0.29}In_{0.71}As_{0.21}Sb_{0.79}$/GaSb QWs (bottom), grown without bismuth, exhibited a single confined resonance. Photoreflectance of $Ga_{0.4}In_{0.6}As_{0.2}Sb_{0.77}Bi_{0.03}$/GaSb QWs (top), grown with a 0.05 ML/s bismuth flux, on the other hand exhibited three confined resonances. (b) Calculated electronic band structures and quantum confinement profiles for $Ga_{0.29}In_{0.71}AsSb$/GaSb (left panel) and $Ga_{0.29}In_{0.71}AsSbBi_{0.03}$/GaSb QWs (right panel), showing increased hole confinement for the bismuth-enhanced material, with the additional confined states evident in the bismuth-enhanced valence band.

films. The peak PL wavelength red-shifted with the additional bismuth by 50% out to 2.8 µm. Meanwhile, the compressive strain increased to only 0.25%. Bismuth incorporated inversely linear with the antimony flux, as the Sb:Ga flux ratio was reduced below 1.

In the GaInAsSbBi materials reported here, PL enhancement was observed in QWs grown with a moderate bismuth flux, up to 34% at 3.6 µm and 25% at 3.9 µm. An expected wavelength shift due to band gap narrowing was not observed, which, along with the observed shifts in XRD to lower strains, points to a change in the incorporation ratio of the anion species. Measured PR spectra showed enhanced res-

onance features related to interband transitions, indicating improved valence band confinement. For the alloy emitting at 3.9 μm, the enhancement was strong enough to confine two higher level states in the valence band. Calculations of the transition energies as a function of bismuth content show that these materials incorporated up to 3% bismuth, significantly improving carrier confinement in the valence band. Future work will try to leverage the strong enhancement from these very small bismuth quantities to enhance hole confinement of highly-strained emitters at 4 μm with a view toward improved laser active regions.

Chapter 6

Conclusions

The work presented in this dissertation describes two avenues explored toward extending the emission of GaSb-based type-I mid-infrared quantum wells to longer wavelengths. The first expanded on the work of Nair in utilizing low substrate temperatures to grow highly-strained GaInAsSb QWs via MBE [81] with increased indium fractions. The second examined using a bismuth flux during the growth of highly-strained QWs to enhance the optical and structural properties of these mid-infrared materials.

By adjusting the QW indium content up to 70%, while maintaining coherent compressive strain of ∼2.3%, GaInAsSb/Gasb QWs exhibited type-I emission with peak room-temperature photoluminescence out to 4 µm. Further increasing the indium content of GaInAsSb/GaSb QWs to 72% at 2.4% strain extended peak room-temperature photoluminescence emission to ∼4.2 µm, albeit with a severe penalty to emission intensity and linewidth. Despite the high strain used, the valence band offset of these QWs continues to be low at the highest QW indium fractions, significantly impacting the confinement of holes to the QW region.

Our work with bismuth investigated its application for improved III-V materials for mid-infrared lasers by using a bismuth flux during growth to enhance the highly-strained QWs. Bismuth was employed as a reactive surfactant during QW growth to improve the optical quality of these materials and alleviate limitations due to critical thickness concerns. GaIn(As)Sb/GaSb QWs were grown, with a bismuth

flux used during select strained QW regions. Those samples grown with a bismuth flux exhibited less optical degradation than non-bismuth-aided samples when grown at thicknesses well past the Matthews–Blakeslee critical thickness limit, offering a potential avenue toward improved material quality of highly-strained layers grown past classical critical thickness limitations.

A more interesting material enhancement was the droplet-free incorporation of dilute amounts of bismuth, up to 3%, as a constituent of quinary GaInAsSbBi alloys. Due to its large atomic radius, bismuth tends to segregate at the surface instead of incorporating into the growing III-V semiconductor. At typical MBE growth temperatures the bismuth present at the surface will ultimately desorb, leaving a bismuth-free surface. However, at lower growth temperatures, such as we used to grow the highly-strained GaInAsSb QWs, bismuth does not desorb as readily and often forms metallic bismuth droplets at the surface, marring material optical quality. In the materials we investigated, droplet formation was mitigated by maintaining V:III flux ratios near unity. We observed droplet-free substitutional bismuth incorporation for moderate bismuth surface coverages, leading to enhanced QW emission performance. Bismuth-related energy levels interact with the valence band states of the GaInAsSb host matrix, and perturb the band structure to improve the QW valence band offset by pushing the valence band up. We observed peak room-temperature photoluminescence enhancement due to bismuth incorporation in candidate QWs emitting at 3.6 µm and at 3.9 µm. This was accompanied by a reduction in QW strain but no appreciable shift in peak emission wavelength, suggesting that bismuth alters the incorporation ratio of the group-V elements As, Sb and Bi. Photoreflectance measurements confirmed type-I band alignments for these materials. Calculated band alignments of these GaInAsSbBi materials were presented, illustrating the enhanced

hole confinement offered by dilute bismide QWs. Future work on this material system will look at the development of dilute bismide active regions for mid-infrared lasers at 4 µm. The improved valence band offsets afforded by dilute bismide materials, enhanced luminescence efficiency, along with the reduced strain make this alloy an exciting material system to continue to develop.

Highly-strained, high indium-content QWs containing 66% indium and strained to 2.2% were used in the active region of an electrically-injected GaInAsSb/GaSb diode laser. The device operated in pulsed mode out to 3.62 µm at 210 K. This is the longest reported wavelength operation of a type-I diode laser with an aluminum-free active region. However, the small valence band offset restricted operation at higher temperatures as the weakly-confined holes are able to readily thermalize out of the QW region and into the barriers, prohibitively increasing the threshold conditions for lasing.

While utilizing high QW strains, high QW indium fractions, and incorporating bismuth all incrementally extended the peak wavelength and improved QW emission, ultimately wavelength extension and device performance is inhibited by the small valence band offsets the exist for smaller band gap mid-infrared materials. However, the enhancements afforded by these methods allows for the delayed utilization of barrier modifications used for mid-infrared lasers at shorter emission wavelengths. Other reported devices use AlGaAsSb barriers up to emission wavelengths of 3.1 µm and QW indium concentrations of 50%, and AlGaInAsSb barriers for devices operating out to 3.73 µm. By employing lattice-matched $Al_{0.3}Ga_{0.7}As_{0.026}Sb_{0.974}$ barriers, type-I QW alignment is restored for highly-strained QWs with indium concentrations up to 72% emitting at 4.2 µm. The improved valence band carrier confinement resulted in peak photoluminescence intensity of these QWs be-

ing improved 3× and the emission linewidth narrowing >30%. In this work we proposed a laser diode device designed to operate at ∼4.1 μm using highly-strained, high indium-content GaInAsSb/AlGaAsSb QW emitters in an edge-emitting ridge waveguide laser structure. In addition to the growth and fabrication of this laser device structure, other future planned work includes pump-dependent PL studies of similar calibration QW structures to allay concerns about gain saturation in these long-wavelength operating type-I QWs.

Appendix

Appendix A

Laser Fabrication Process

The following steps describe the fabrication process for edge-emitting laser devices used in this dissertation.

A.1 Process sample preparation

In order to maintain process consistency, reasonable wafer consumption rates, and good device yield, the process sample size was standardized to 1 cm $\times$ 1 cm. The 1-cm^2 size allowed for up to 17 samples to be taken from one as-grown 2-inch wafer, as well as yielded 3 to 4 bars of test devices per fabricated sample at the end of fabrication.

A.1.1 Process sample cleaving

Laser material was epitaxially grown on 2-inch n-doped GaSb substrates. The major diameter of the nGaSb substrates is 50.8 mm and the major flat $\sim$16 mm. The total wafer area is $\sim$20.3 cm^2, and up to 17 square centimeter samples can be cleaved from one wafer, as shown in Figure A.1. The following steps detail how to cleave out 17 1$\times$1 square centimeter samples from one 2-inch wafer.

Align a ruler along the major flat ($\sim$16 mm). Cleave the middle centimeter strip starting from the major flat (leaving 3 mm on either side.). Cleave the strip into centimeter squares starting from major flat. Up to 5 samples can be obtained from

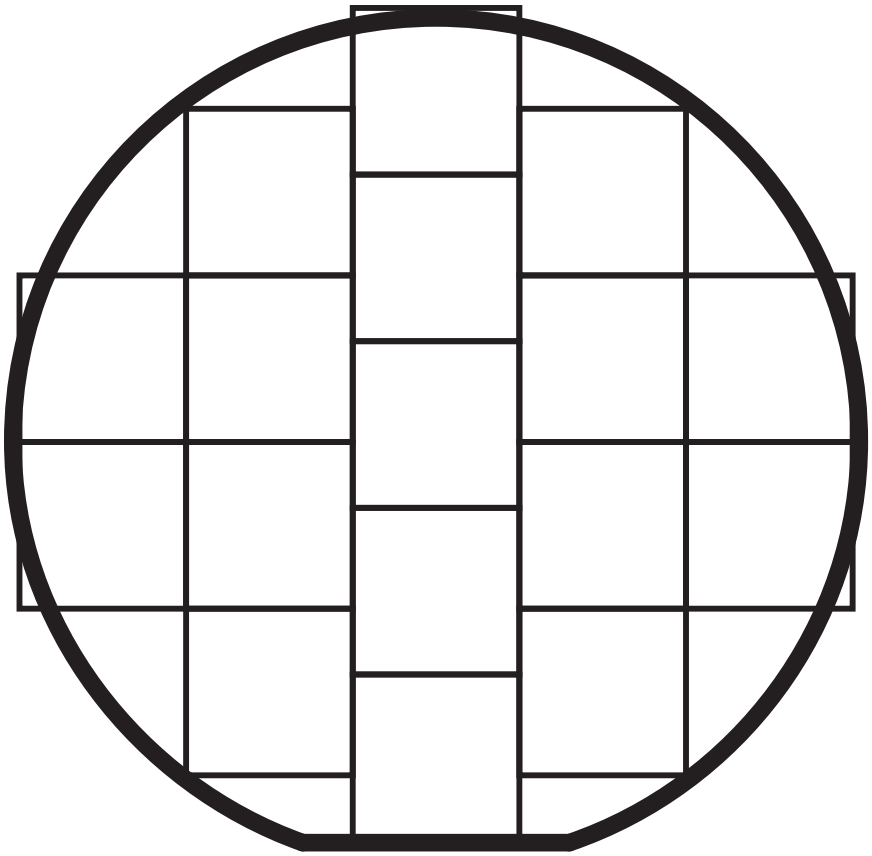

Figure A.1: Arrangement of 1-cm × 1-cm process samples across a 2-inch wafer. Lines indicate where to scribe and cleave samples.

the center strip, although the last sample at the rounded edge will not be exactly 1 square centimeter.

Cleave each of the remaining side pieces 25 mm from the edge opposite the major flat. Cleave again to yield 1-cm strips starting from the just-cleaved edge. Two strips from each side can be made, with a small wafer scrap left over on each side.

From the shorter strips, one square centimeter sample each can be taken. From the longer, up to two can be taken, although the samples at wafer edge may be slightly non-square.

The larger scrap pieces can be used for I-V and XRD quality control checks of the epi growth, as well as etched to remove the upper cladding to inspect the as-grown quantum well quality.

A.1.2 SiNx deposition

SiNx is used as a hard mask during ridge etching for the ridge waveguide process flow detailed in A.2.1. The SiNx also etches during the ridge etch, but at a much slower rate, about one-tenth, than the III-V material. A 400-nm SiNx layer is thick enough to last through the ridge etch step. For the gain-guided waveguide process flow described in A.2.4, the top contact window is etched into the SiNx layer. The SiNx layer is deposited using PECVD on Plasmatherm #1 as detailed in the following steps.

1. Run a 30-minute O2 plasma clean of the PECVD chamber at 250 °C.
2. Run the SiNx recipe AMC_SIN for 3 minutes to "prime" the chamber. The chamber vents at the end of this step.
3. Load sample(s). The SiNx deposition rate is ∼20 nm/min. For 400 nm, do a 20 minute run.
4. Run a 40 minute (2×the deposition time or 30 minutes, whichever is longer) post-deposition O2 plasma clean. Standard is 30 minutes.

A.2 Top-side processing

The top-side fabrication process follows one of two separate processes, depending on whether or not laser ridges to improve current confinement were etched. For ridge-waveguide devices, follow the procedure starting in Section A.2.1. For gain-guided devices, follow the procedure starting in Section A.2.4.

A.2.1 Ridge Waveguide Laser Stripe Steps

Photolithography and reactive ion etching are used to pattern the SiNx layer deposited previously to create the hard mask for the ridge etching step.

A.2.1.1 Photolithography Mask 1

Use Laser 2013 Mask 1. The photoresist AZ 5214 E is used in positive tone. The steps for this recipe come from Sukrith Dev and were updated by Andrew Briggs. The spinner in Hood J23 works best. The MJB4 can be used for broad area devices. Use the MA6 for narrow ridge devices.

1. Solvent clean: acetone for 2 minutes, isopropyl alcohol for 2 minutes, deionized water for 2 minutes. Following the solvent clean, leave the samples in isopropyl alcohol until ready to begin processing.
2. Blow dry sample with N2 gun.
3. Spin on photoresist at 45 krpm for 1 minute.
4. Prebake at 110 °C on hot plate for 50 seconds.
5. Let the sample rest for 2 minutes following bake.
6. Expose with 365-nm UV light at 7.5 mW/cm^2 for 13 seconds. Make sure to align the mask features with the wafer edge for future facet cleaving.
   6.1. MJB4 parameters: Soft contact
   6.2. MA6 parameters: High vac contact, 20 µm gap, 6-15-6
7. Develop in AZ-26A developer for 45 seconds (sensitive) with no agitation.
8. Rinse 30 seconds in deionized water and for an additional 30 seconds in a second deionized water rinse.
9. Inspect features.

A.2.1.2 SiNx Patterning

Prep the Plasmatherm 2 RIE chamber by running a 30-minute O2 plasma clean. The etch recipe is /zheng/si02low. The recipe etch rate of SiNx is about 135 nm/min. For 400 nm, etch for 3 minutes. The etch is very selective against the III-V, so it is also okay to over etch this step.

A.2.1.3 Photoresist Strip and Clean

Remove photoresist in a Kwikstrip bath at 90 degrees C for 30 minutes (MBE workroom hot plate setting of 120 degrees).

Descum using Plasmatherm 2 RIE. Use Zheng descum (uses turbo to baseline) with the following parameters:

- 20 sccm O2
- 100 W
- 50 mTorr
- 5 minutes

A.2.2 Laser Ridge Etching

A.2.2.1 Ion-coupled plasma etch

Prep the Oxford ICP Chamber with a 30-minute O2 plasma clean. Use either the KV Chamber Clean or the O2 Chamber Clean recipe. Make sure there is a carrier wafer in the load lock before starting the recipe!!

Run the SDS CL-N2 etch recipe. The etch rate is $\sim$10 nm/s, and the III-V:SiN selectivity is $\sim$10. The etch should leave about 100-150 nm of cladding above the laser waveguide. Run a dummy sample for 3 minutes to get the starting etch rate for the day. Target the first laser run to etch $\sim$90% of the ridge. Dektak to find III-V plus SiN ridge depth and SiN depth. The difference is the III-V ridge depth. Calculate the

etch rate and the remaining etch time to get to the target depth. Etch for 90% of that time. The ridge should be very close to done.

A.2.2.2 SiNx hardmask stripping

Strip the residual SiNx hardmask using RIE on Plasmatherm 2. /Zheng/SIO2LOW for 3 minutes.

A.2.2.3 SiNx Ridge Conformal Coat

Coat with 400 nm of PECVD SiNx in Plasmatherm 1 as in Section A.1.2.

A.2.3 Ridge Contact Window Patterning

Use Laser 2013 Mask 1.5. The photoresist AZ 5214 E s used in image-reversal mode.

1. Solvent clean: acetone for 2 minutes, isopropyl alcohol for 2 minutes, deionized water for 2 minutes. Following the solvent clean, leave the samples in isopropyl alcohol until ready to begin processing.
2. Blow dry sample with N2 gun.
3. Spin on photoresist at 4.5 krpm for 1 minute. Use enough photoresist to flow off of the wafer. 5-7 drops for 1 cm^2.
4. Prebake at 100 °C on hot plate for 1 minute.
5. Let sample rest on side for 2 minutes.
   5.1. MJB4 parameters: Soft contact
   5.2. MA6 parameters: High vac contact, 20 µm gap, 6-15-6
6. Expose on MA6 (7.5 mW/cm^2) for 2 seconds. Make sure to align the mask features previous mask alignment marks.
7. Postbake at 110 °C on hot plate for 2 minutes.

8. Let sample rest on side for 2 minutes.
9. Flood expose (no mask) on MJB4 for 60 seconds.
10. Develop in AZ-26A developer for up to 3 minutes (not sensitive) with no agitation.
11. Rinse 30 seconds in deionized water and for an additional 30 seconds in a second deionized water rinse.
12. Inspect features under a microscope.

    Proceed to Section A.2.5.

A.2.4 Gain-guided Laser Stripe Steps

Use Laser 2013 Mask 1. The photoresist AZ 5214 E is used in image reversal mode. The MJB4 can be used for broad area devices. Use the MA6 for narrow ridge devices.

1. Solvent clean: acetone for 2 minutes, isopropyl alcohol for 2 minutes, deionized water for 2 minutes. Following the solvent clean, leave the samples in isopropyl alcohol until ready to begin processing.
2. Blow dry sample with N2 gun.
3. Spin on photoresist at 4.5 krpm for 1 minute. Use enough photoresist to flow off of the wafer. 5-7 drops for 1 cm^2.
4. Prebake at 100 °C on hot plate for 1 minute.
5. Let sample rest on side for 2 minutes.

    5.1. MJB4 parameters: Soft contact

    5.2. MA6 parameters: High vac contact, 20 μm gap, 6-15-6
6. Expose at 7.5 mW/cm^2 for 2 seconds. Make sure to align the mask features previous mask alignment marks.

7. Postbake at 110 °C on hot plate for 2 minutes.
8. Let sample rest on side for 2 minutes.
9. Flood expose (no mask) on MJB4 for 60 seconds.
10. Develop in AZ-26A developer for up to 3 minutes (not sensitive) with no agitation.
11. Rinse 30 seconds in deionized water and for an additional 30 seconds in a second deionized water rinse.
12. Inspect features under a microscope.

    Proceed to Section A.2.5.

A.2.5 Common Top-side steps

A.2.5.1 Contact Window Etch

Prep the Plasmatherm 2 RIE chamber by running a 30-minute O2 plasma clean. The etch recipe is /zheng/si02low. The recipe etch rate of SiNx is about 135 nm/min. For 400 nm, etch for 3 minutes. The etch is very selective against the III-V, so it is also okay to over etch this step.

A.2.5.2 PR Strip and Clean

Remove photoresist in a Kwikstrip bath at 90 degrees C for 30 minutes (MBE workroom hot plate setting of 120 degrees).

Descum using Plasmatherm 2 RIE. Use Zheng descum (uses turbo to baseline) with the following parameters:

- 20 sccm O2
- 100 W
- 50 mTorr
- 5 minutes

A.2.5.3 Laser Metal Mask Patterning

Use Laser 2013 Mask 2. The photoresist AZ 5214 E is used in image reversal mode. The MJB4 can be used for broad area devices. Use the MA6 for narrow ridge devices.

1. Solvent clean: acetone for 2 minutes, isopropyl alcohol for 2 minutes, deionized water for 2 minutes. Following the solvent clean, leave the samples in isopropyl alcohol until ready to begin processing.
2. Blow dry sample with N2 gun.
3. Spin on photoresist at 4.5 krpm for 1 minute. Use enough photoresist to flow off of the wafer. 5-7 drops for 1 cm^2.
4. Prebake at 100 °C on hot plate for 1 minute.
5. Let sample rest on side for 2 minutes.
   5.1. MJB4 parameters: Soft contact
   5.2. MA6 parameters: High vac contact, 20 µm gap, 6-15-6
6. Expose at 7.5 mW/cm^2 for 2 seconds. Make sure to align the mask features previous mask alignment marks.
7. Postbake at 110 °C on hot plate for 2 minutes.
8. Let sample rest on side for 2 minutes.
9. Flood expose (no mask) on MJB4 for 60 seconds.
10. Develop in AZ-26A developer for up to 3 minutes (not sensitive) with no agitation.
11. Rinse 30 seconds in deionized water and for an additional 30 seconds in a second deionized water rinse.
12. Inspect features under a microscope.

A.2.5.4 Sample preparation for top-side metalization

Use double-sided kapton tape to adhere samples to glass slide. The slide can be clipped to the top of the CHA chamber to avoid shadowing the sample during metal evaporation.

Prior to metal deposition, etch the native oxide from contact windows by dipping in HCl:DI-H2O solution (1:10, MRC supplied HCl is 37%, so a 2:5 volume ratio (ex.: 40 mL:100 mL) of HCl to DI-H2O yields an acid solution of ∼10.6%). The oxide is hydrophillic (attracts water). The etch is finished when water beads and runs off the exposed contact window, ∼1-2 minutes. Rinse in deionized water for 30 seconds.

A.2.5.5 Top Metal Deposition

The top contact metal stack is Ti/Pt/Au. At a minimum deposit 40 nm, 25 nm, and 200 nm, respectively.

A.2.5.6 PR Strip and Metal Liftoff

Using kwikstrip heated to 90 C (about 120 C on the hot plate setting), the photoresists dissolves and metal lifts right off. Spraying the sample with an acetone squirt bottle can remove loose bits of metal. After liftoff, put the sample in hot acetone (70-80 C) to clean off kwikstrip residue and break down the adhesive on the kapton. The samples should pop right off the kapton. Then put the samples in an IPA bath to clean the acetone residue. Blow dry with N2 gun.

A.3 Backside processing

A.3.1 Sample Clean and Mounting

Following top-side processing, the laser processing sample is mounted top-side down onto a glass slide. Prepare the glass slide by scribing and breaking to yield a piece roughly 15 mm $\times$ 15 mm. Run the sample and glass slide through the 4-part solvent clean: acetone for 2 minutes, isopropyl alcohol for 2 minutes, deionized water for 2 minutes, return to isopropyl alcohol. Blow dry the glass and sample with N2 gun.

Spin on AZ 5214 onto the top side of the laser processing sample at 2 krpm for 1 minute. Place the sample substrate side down onto a hot plate at 90 °C for 1 minute. Remove the sample from the hot plate and let it cool.

Place small bits of Quickstick 135 onto the glass slide. Heat the slide on a hot plate to soften the Quickstick. Use a razor to make a thin smooth layer on the slide. Gently press the laser processing sample top-side down onto the Quickstick. Press gently all around to evenly adhere the sample onto slide. Remove the slide and sample from the hot plate and let it cool.

Place Quickstick 135 on the lapping chuck and heat it up to soften the Quick-stick. Once it is soft, place the glass slide onto the chuck and press firmly to adhere the slide onto the lapping chuck. Make sure to scrape any Quickstick away from the sides or substrate surface of the sample, as it is much harder than the substrate and will greatly extend thinning and polish time. The sample is now prepared for thinning and polishing.

A.3.2 Substrate Thinning and Polish

Assemble the lapping assembly: chuck, retaining ring, and lapping stop. Adjust the retaining ring so that ∼100 µm will remain once the lapping stop is bottomed out. Tape down the retaining ring to the chuck to prevent the chuck from shifting and changing the lapping depth.

During the lapping and polishing process, gently spray the sample with isopropyl alcohol to remove lapping debris. Spray over the lapping fume hood sink and collect all waste in a carboy below the drain.

The first lapping step thins the laser processing samples to ∼100 µm. Fully clean the lapping cup, platen, and chuck before lapping. Use 600 grit lapping paper on the Minimet lapping tool. Adjust the speed to 20 and the force to 0. Squirt water onto the lapping paper to roughly the diameter of a nickel. Thin the sample until it reaches the desired thickness, checking every 30 minutes until done. At each inspection, change the lapping paper, cleaning the lapping platen and cup as well. Prior to polishing, fully clean the chuck, work area, and lapping tool. Put away all lapping supplies including the paper, lapping cup and platen, and anything else that may be contaminated with 600 grit. Any residual 600 grit material will detract from the following polish steps.

Polishing is done in two steps. The first step uses a TriDent polishing cloth and 1-µm deagglomorated alumina polishing suspension. Place a new polishing cloth on the platen and squirt a generous amount of polishing suspension onto the cloth. Lower the chuck in the lapping assembly about 1/2 turn from the previous thinning step. Use the same tool settings as the previous step. Check the sample every 30 minutes. Keep going until the large lapping grooves from the previous step have

been polished out. Fully clean the supplies, tools, sample, chuck, and work area of any remnants from this step before proceeding to the final polish step.

The second polish step uses a MicroCloth polishing cloth and 0.3-µm deag-glmorated alumina polishing suspension. Follow the same settings as the previous step, checking the sample every 30 minutes until features remaining from the previous step are removed. Only change the pad if it has become saturated with polishing suspension and polishing is not progressing.

After all lapping and polish steps are completed, place the sample/lapping chuck on a hot plate. Heat up to the flow point of the Quickstick 135 (∼135 °C). Gently slide the glass slide off of chuck when the bonding agent flows. Place the glass slide with the sample in a dipper basket and do a 3-part solvent clean (acetone free) to remove any remaining polishing debris: isopropyl alcohol for 2 minutes, deionized water for 2 minutes, return to isopropyl alcohol. Blow dry the glass and sample with N2 gun. Leave the sample on the glass slide for backside metalization.

A.3.3 Backside Metal

Prior to metal deposition, etch the native oxide from contact windows by dipping in HCl:DI-H2O solution (1:10, MRC supplied HCl is 37%, so a 2:5 volume ratio (ex.: 40 mL:100 mL) of HCl to DI-H2O yields an acid solution of ∼10.6%). The oxide is hydrophillic (attracts water). The etch is finished when water beads and runs off the exposed contact window, ∼1-2 minutes. Rinse in deionized water for 30 seconds.

The bottom contact metal stack is Au/Sn/Ni/Au, with standard thicknesses of 15.1 nm, 10 nm, at least 12.5 nm, and at least 200 nm. Try for 200 nm Au if possible.

The Au/Sn thickness ratio is calibrated to form a eutectic at the anneal step. The Au-Sn eutectic is 80:20 Au:Sn by weight. The weight of a metal layer is its density multiplied by the volume, and the volume is the area of the deposited metal layer multiplied by its thickness. The metal densities are ρ_{Au}=19.32 g/mL and ρ_{Sn}=7.31 g/mL. The cross-sectional area A of both metal layers is equal, and thus cancels out of the ratio, leaving the ratio of 4 equal to the ratio of the density of Au:Sn multiplied by the ratio of the thickness of Au:Sn, or

$$4 = \frac{\rho_{Au}}{\rho_{Sn}} \times \frac{t_{Au}}{t_{Sn}}. \tag{A.1}$$

Solving for $\frac{t_{Au}}{t_{Sn}}$ yields 1.513. Thus 100 Å of Sn needs 151.3 Å of Au to form the right ratio of material for a eutectic after alloying.

The nickel layer forms a diffusion barrier for the thicker gold layer to prevent spiking into the semiconductor.

A.3.4 Sample Demounting

Place the still-mounted and now-metalized sample in hot acetone (∼60-70 °C hot plate) for 5-10 minutes until the photoresist is dissolved. The sample should slide off the glass slide easily. An acetone stream from the squeeze bottle can be used to check for sample liftoff. Replace the acetone and let the demounted sample sit for an additional 2 to 5 minutes to remove any residual residues.

Run a 3-part solvent clean (acetone free) : isopropyl alcohol for 2 minutes, deionized water for 2 minutes, return to isopropyl alcohol. Gently blow dry the sample with the N2 gun.

A.3.5 Contact Anneal

The contact anneal is done in the AW 610 RTA. Before annealing a process sample, do a dummy run to insure the setup works properly. In the RTA, place in order from bottom to top a Si backing wafer, the bottom GaSb RTA proximity cap, and the top GaSb RTA proximity cap. Run the LASE350S RTA recipe. If there are no faults, at the conclusion of the recipe (includes 5 minute cooldown step) remove the stack, and place the sample to be annealed between the GaSb proximity caps. Put the stack back into the RTA and run the same RTA recipe.

This same procedure can also be done on the AET tool.

A.3.6 Backside metal 2

Following contact annealing, the backside metal has a nickel finish. Remount the sample epi down on a glass slide with Quickstick 135. Quickstick 135 softens at 71 degrees C and flows at 135 degrees C.

Deposit 10-nm Ti and 200-nm Au onto the annealed backside contact. There is no need to acid dip prior to this metal step.

Demount the sample in acetone. Run the sample through the 4-part solvent clean once it is demounted: acetone for 2 minutes, isopropyl alcohol for 2 minutes, deionized water for 2 minutes, return to isopropyl alcohol. Blow dry the glass and sample with N2 gun.

A.4 Final Processing and Packaging

A.4.1 Facet Cleaving

Scribe an edge of the laser sample where the facet cleave will propogate from. Make sure to scribe on the top side. Put the laser sample between mylar discs, p/n

DX-207-01 (3.5”x0.001”) and glass slides. Make sure the scribe mark is up, and outside the edge of the glass slides. Press down on the mylar sheets near the glass slide edges until cleave happens. Check facet quality on the supplied SEM stub. It may be useful to put something on the stub to provide better contrast to sample, such as a cloth kimwipe.

A.4.2 Subcarrier Mounting

A.4.2.1 Mounting to a copper submount

Mount cleaved laser bars with InSn solder stripes to copper submounts that have been previously coated with 10 nm Ni and 100 nm Au. The copper submounts are 101 (oxygen-free) copper from McMaster. 1/16” thick x 1/2” x 1-3/8”. Holes are drilled for #8-32 screws. Use a #18 drill with holes on a 0.73” center, 0.3” from one side. Place InSn solder coupons on top of each laser bar.

Place InSn solder strips onto the copper submount. Scrape smooth, then cool. Place laser test sample on cold solder. Lightly tack the sample onto the cold solder. Make sure it does not come off when tilted. Place sample holder onto hot plate, melt solder, then press laser into melted solder. Remove from heat, cool, and make sure the sample is bonded. Place InSn solder strips on the top contacts of the laser bars

A.4.2.2 Mounting to a Si wafer

The laser bars can also be mounted to a prepared Si wafer. Coat a Si wafer with PECVD SiN. Evaporated Ti/Au on top of the SiN. 13 mm $\times$ 5 mm coupons are a good size to cleave from the wafer to make holders for cryostat mounting.

Gold contact sites can be made by scribing gold away to electrically isolate pads for the laser contacts. Gold-coated alumina headers can also be bonded to create electrically-isolated sites for wirebonding.

A.4.2.3 Wirebonding

To facilitate even current injection to the laser ridge when mounted epi-up, wirebond along the top of the ridge. Each wirebond can handle ~250 mA per wirebond. Thus 3 A will need at least 12 wirebonds.

Using the prepared silicon wafer, PECVD coated with SiN, with evaporated Ti/Au (10 nm/200 nm) on it, cleave into 0.5-in x 0.25-in coupons. Scratch off gold to make isolated pads. Indium solder paste the laser sample. Wirebond laser stripes to pads.

Make In blob or Gold ball on pad for probe tip, to reduce singeing the gold at the point of probe contact (from high field/current density)

Place In:Sn stripes on gold carrier. Place on hot plate to melt stripe. Use dummy piece to smear the In:Sn around. Let cool. Place laser die on top of In. Gently press down to tack in place. Put back on hot plate. Let In:Sn melt (about 1 minute). Press again gently but firmly. Slide die side to side to get good contact layer if In between device backside and gold pad. Remove from heat and let cool. Test for adherence.

Wire bond die to carrier pads. Ball bond to the carrier and wedge bond to the laser stripe.

Bibliography

[1] A. Bauer *et al.*, "Mid-infrared semiconductor heterostructure lasers for gas sensing applications," *Semiconductor Science and Technology*, vol. 26, no. 1, p. 014032, Dec. 2010.

[2] M.W. Sigrist, *Air Monitoring by Spectroscopic Techniques*, M.W. Sigrist, J.D. Winefordner, and I.M. Kolthoff, Eds. John Wiley & Sons, Mar. 8, 1994, 560 pp.

[3] I. Gordon *et al.*, "The HITRAN2016 molecular spectroscopic database," *Journal of Quantitative Spectroscopy and Radiative Transfer*, vol. 203, pp. 3–69, Dec. 2017.

[4] G. Wysocki, A.A. Kosterev, and F.K. Tittel, "Spectroscopic trace-gas sensor with rapidly scanned wavelengths of a pulsed quantum cascade laser for in situ NO monitoring of industrial exhaust systems," *Applied Physics B*, vol. 80, no. 4-5, pp. 617–625, Mar. 2005.

[5] F.K. Tittel, "Current status of midinfrared quantum and interband cascade lasers for clinical breath analysis," *Optical Engineering*, vol. 49, no. 11, p. 111123, Nov. 2010.

[6] L.E. Christensen, "Thermoelectrically cooled interband cascade laser for field measurements," *Optical Engineering*, vol. 49, no. 11, p. 111119, Nov. 2010.

[7] Avionics Department, "Electronic Warfare and Radar Systems Engineering Handbook," Naval Air Warfare Center Weapons Division, Tech. Rep., 2013.

[8] S.D. Sifferman *et al.*, "Highly strained mid-infrared type-I diode lasers on GaSb," *IEEE Journal of Selected Topics in Quantum Electronics*, vol. 21, no. 6, pp. 1–10, Nov. 2015.

[9] S. Simanowski *et al.*, "Growth and layer structure optimization of 2.26 µm (AlGaIn)(AsSb) diode lasers for room temperature operation," *Journal of Crystal Growth*, vol. 227-228, pp. 595–599, Jul. 2001.

[10] R.P. Leavitt *et al.*, "High performance interband cascade lasers at 3.8 microns," *Novel In-Plane Semiconductor Lasers XI*, SPIE, Feb. 2012.

[11] A. Lyakh, R. Maulini, A. Tsekoun, R. Go, and C.K.N. Patel, "Tapered 4.7 µm quantum cascade lasers with highly strained active region composition delivering over 4.5 watts of continuous wave optical power," *Optics Express*, vol. 20, no. 4, p. 4382, Feb. 2012.

[12] W.W. Bewley *et al.*, "High-power, high-brightness continuous-wave interband cascade lasers with tapered ridges," *Applied Physics Letters*, vol. 103, no. 11, p. 111111, Sep. 2013.

[13] C.L. Canedy *et al.*, "Pulsed and CW performance of 7-stage interband cascade lasers," *Optics Express*, vol. 22, no. 7, pp. 7702–7710, Mar. 2014.

[14] R. Liang *et al.*, "Distributed feedback 3.27 µm diode lasers with continuous-wave output power above 15 mW at room temperature," *Electronics Letters*, vol. 50, no. 19, pp. 1378–1380, Sep. 2014.

[15] C. Borgentun, C. Frez, R.M. Briggs, M. Fradet, and S. Forouhar, "Single-mode high-power interband cascade lasers for mid-infrared absorption spectroscopy," *Optics Express*, vol. 23, no. 3, pp. 2446–2450, Jan. 2015.

[16] M. Kim *et al.*, "High-power continuous-wave interband cascade lasers with 10 active stages," *Optics Express*, vol. 23, no. 8, pp. 9664–9672, Apr. 2015.

[17] L. Li *et al.*, "Low-threshold InAs-based interband cascade lasers operating at high temperatures," *Applied Physics Letters*, vol. 106, no. 25, p. 251102, Jun. 2015.

[18] I.E. Trofimov *et al.*, "Interband cascade lasers with long lifetimes," *Applied Optics*, vol. 54, no. 32, pp. 9441–9445, Nov. 2015.

[19] T. Hosoda, T. Feng, L. Shterengas, G. Kipshidze, and G. Belenky, "High power cascade diode lasers emitting near 2 µm," *Applied Physics Letters*, vol. 108, no. 13, p. 131109, Mar. 2016.

[20] A. Bismuto *et al.*, "High power and single mode quantum cascade lasers," *Optics Express*, vol. 24, no. 10, pp. 10694–10699, May 2016.

[21] L. Shterengas, G. Kipshidze, T. Hosoda, M. Wang, T. Feng, and G. Belenky, "Cascade type-I quantum well GaSb-based diode lasers," *Photonics*, vol. 3, no. 2, p. 27, May 2016.

[22] M. Wang *et al.*, "Narrow ridge cascade diode lasers with λ>3 µm," *Conference on Lasers and Electro-Optics*, OSA, Jun. 2016.

[23] S. Höfling, R. Weih, and M. Kamp, "Mid-infrared interband cascade lasers," *2016 IEEE Photonics Conference (IPC)*, pp. 80–81, IEEE, Oct. 2016.

[24] C.L. Canedy *et al.*, "Interband cascade lasers with longer wavelengths," *Quantum Sensing and Nano Electronics and Photonics XIV*, p. 10 111, SPIE, Jan. 2017.

[25] C.-W. Liu *et al.*, "Low power consumption substrate-emitting DFB quantum cascade lasers," *Nanoscale Research Letters*, vol. 12, no. 1, p. 517, Sep. 2017.

[26] C.K.N. Patel, M. Troccoli, and R. Barron-Jimenez, "Quantum cascade lasers: 25 years after the first demonstration," *Technologies for Optical Countermeasures XVI*, SPIE, Oct. 2019.

[27] Q. Lu, S. Slivken, D. Wu, and M. Razeghi, "High power continuous wave operation of single mode quantum cascade lasers up to 5 W spanning $\lambda\sim$3.8-8.3 µm," *Optics Express*, vol. 28, no. 10, p. 15181, May 2020.

[28] F. Wang, S. Slivken, D.H. Wu, and M. Razeghi, "Room temperature quantum cascade lasers with 22% wall plug efficiency in continuous-wave operation," *Optics Express*, vol. 28, no. 12, p. 17532, May 2020.

[29] F. Wang, S. Slivken, D.H. Wu, Q.Y. Lu, and M. Razeghi, "Continuous wave quantum cascade lasers with 5.6 W output power at room temperature and 41% wall-plug efficiency in cryogenic operation," *AIP Advances*, vol. 10, no. 5, p. 055120, May 2020.

[30] J. Faist, F. Capasso, D.L. Sivco, C. Sirtori, A.L. Hutchinson, and A.Y. Cho, "Quantum cascade laser," *Science*, vol. 264, no. 5158, pp. 553–556, Apr. 1994.

[31] M. Razeghi, "High-performance InP-based mid-IR quantum cascade lasers," *IEEE Journal of Selected Topics in Quantum Electronics*, vol. 15, no. 3, pp. 941–951, May 2009.

[32] O. Cathabard, R. Teissier, J. Devenson, and A. Baranov, "InAs-based distributed feedback quantum cascade lasers," *Electronics Letters*, vol. 45, no. 20, pp. 1028–1030, Sep. 2009.

[33] Y. Bai, S. Slivken, S. Kuboya, S.R. Darvish, and M. Razeghi, "Quantum cascade lasers that emit more light than heat," *Nature Photonics*, vol. 4, no. 2, pp. 99–102, Jan. 2010.

[34] O. Cathabard, R. Teissier, J. Devenson, J.C. Moreno, and A.N. Baranov, "Quantum cascade lasers emitting near 2.6 µm," *Applied Physics Letters*, vol. 96, no. 14, p. 141110, Apr. 2010.

[35] J.P. Commin, D.G. Revin, S.Y. Zhang, A.B. Krysa, K. Kennedy, and J.W. Cockburn, "High peak power $\lambda\sim$3.3 and 3.5 µm InGaAs/AlAs(Sb) quantum cascade lasers operating up to 400 K," *Applied Physics Letters*, vol. 97, no. 3, p. 031108, Jul. 2010.

[36] N. Bandyopadhyay *et al.*, "Watt level performance of quantum cascade lasers in room temperature continuous wave operation at $\lambda\sim$3.76 µm," *Applied Physics Letters*, vol. 97, no. 13, p. 131117, Oct. 2010.

[37] A. Bismuto, M. Beck, and J. Faist, "High power Sb-free quantum cascade laser emitting at 3.3 µm above 350 K," *Applied Physics Letters*, vol. 98, no. 19, p. 191104, May 2011.

[38] M. Razeghi, "High power, high wall-plug efficiency, high reliability, continuous-wave operation quantum cascade lasers at center for quantum devices," Feb. 2020.

[39] H.K. Choi, "Coherent semiconductor sources in the long-wavelength infrared spectrum," in *Long-Wavelength Infrared Semiconductor Lasers*, H.K. Choi, Ed., ser. Wiley Series in Lasers and Applications. Hoboken, NJ, USA: John Wiley & Sons, Inc., Mar. 2005, ch. 1, pp. 1–17.

[40] Y. Bai, S. Slivken, S.R. Darvish, A. Haddadi, B. Gokden, and M. Razeghi, "High power broad area quantum cascade lasers," *Applied Physics Letters*, vol. 95, no. 22, p. 221104, Dec. 2009.

[41] Y. Bai, N. Bandyopadhyay, S. Tsao, S. Slivken, and M. Razeghi, "Room temperature quantum cascade lasers with 27% wall plug efficiency," *Applied Physics Letters*, vol. 98, no. 18, p. 181102, May 2011.

[42] R.Q. Yang, "Infrared laser based on intersubband transitions in quantum wells," *Superlattices and Microstructures*, vol. 17, no. 1, pp. 77–83, Jan. 1995.

[43] J. Meyer, I. Vurgaftman, R. Yang, and L. Ram-Mohan, "Type-II and type-I interband cascade lasers," *Electronics Letters*, vol. 32, no. 1, pp. 45–46, Jan. 1996.

[44] W.W. Bewley *et al.*, "Lifetimes and Auger coefficients in type-II W interband cascade lasers," *Applied Physics Letters*, vol. 93, no. 4, p. 041118, Jul. 2008.

[45] W.W. Bewley *et al.*, "Interband cascade laser operating cw to 257 K at λ=3.7 µm," *Applied Physics Letters*, vol. 89, no. 16, p. 161106, Oct. 2006.

[46] I. Vurgaftman *et al.*, "Mid-infrared interband cascade lasers operating at ambient temperatures," *New Journal of Physics*, vol. 11, no. 12, p. 125015, Dec. 2009.

[47] I. Vurgaftman *et al.*, "Interband cascade lasers with low threshold powers and high output powers," *IEEE Journal of Selected Topics in Quantum Electronics*, vol. 19, no. 4, pp. 1200210–1200210, Jul. 2013.

[48] C.L. Canedy *et al.*, "High-power continuous-wave midinfrared type-II "W" diode lasers," *Applied Physics Letters*, vol. 86, no. 21, p. 211105, May 2005.

[49] W.W. Bewley *et al.*, "Mid-IR interband cascade lasers operating with < 30 mW of input power," *Next-Generation Spectroscopic Technologies V*, 83740H, SPIE, Apr. 2012.

[50] W.W. Bewley *et al.*, "Continuous-wave interband cascade lasers operating above room temperature at λ= 4.7–5.6 µm," *Optics Express*, vol. 20, no. 3, pp. 3235–3240, Jan. 2012.

[51] W.W. Bewley *et al.*, "High-power room-temperature continuous-wave mid-infrared interband cascade lasers," *Optics Express*, vol. 20, no. 19, pp. 20894–20901, Aug. 2012.

[52] R. Weih, A. Bauer, M. Kamp, and S. Höfling, "Interband cascade lasers with AlGaAsSb bulk cladding layers," *Optical Materials Express*, vol. 3, no. 10, pp. 1624–1631, Sep. 2013.

[53] S. Forouhar *et al.*, "Reliable mid-infrared laterally-coupled distributed-feedback interband cascade lasers," *Applied Physics Letters*, vol. 105, no. 5, p. 051110, Aug. 2014.

[54] J.G. Kim, L. Shterengas, R.U. Martinelli, G.L. Belenky, D.Z. Garbuzov, and W.K. Chan, "Room-temperature 2.5 µm InGaAsSb/AlGaAsSb diode lasers emitting 1 W continuous waves," *Applied Physics Letters*, vol. 81, no. 17, pp. 3146–3148, Oct. 2002.

[55] A. Garnache *et al.*, "2–2.7 µm single frequency tunable Sb-based lasers operating in CW at RT: microcavity and external cavity VCSELs, DFB," *Semiconductor Lasers and Laser Dynamics II*, 61840N, Strasbourg, France: SPIE, Apr. 2006.

[56] D. Donetsky, G. Kipshidze, L. Shterengas, T. Hosoda, and G. Belenky, "2.3 µm type-I quantum well GaInAsSb/AlGaAsSb/GaSb laser diodes with quasi-CW output power of 1.4 W," *Electronics Letters*, vol. 43, no. 15, pp. 810–811, Jul. 2007.

[57] M.T. Kelemen *et al.*, "Diode laser arrays for 1.8 to 2.3 µm wavelength range," *Technologies for Optical Countermeasures VI*, p. 74830C, SPIE, Sep. 2009.

[58] L. Shterengas, R. Liang, G. Kipshidze, T. Hosoda, S. Suchalkin, and G. Belenky, "Cascade pumping of GaSb-based type-I quantum well diode lasers," *Novel In-Plane Semiconductor Lasers XIII*, p. 900 213, SPIE, Feb. 2014.

[59] G.W. Turner, H.K. Choi, and M.J. Manfra, "Ultralow-threshold (50 A/cm^2) strained single-quantum-well GaInAsSb/AlGaAsSb lasers emitting at 2.05 µm," *Applied Physics Letters*, vol. 72, no. 8, pp. 876–878, Dec. 1998.

[60] A. Salhi, Y. Rouillard, J. Angellier, P. Grech, and A. Vicet, "2.61 µm GaInAsSb-/AlGaAsSb type I quantum well laser diodes with low threshold," *Electronics Letters*, vol. 40, no. 7, pp. 424–425, Apr. 2004.

[61] C. Lin, M. Grau, O. Dier, and M.-C. Amann, "Low threshold room-temperature continuous-wave operation of 2.24–3.04 µm GaInAsSb/AlGaAsSb quantum-well lasers," *Applied Physics Letters*, vol. 84, no. 25, pp. 5088–5090, Jun. 2004.

[62] Y. Rouillard, J. Angellier, A. Salhi, P. Grech, and F. Chevrier, "GaInAsSb/AlGaAsSb laser diodes for the 2- to 3-µm range," *Novel In-Plane Semiconductor Lasers IV*, p. 5738, San Jose, California, United States: SPIE, Apr. 2005.

[63] A.R. Adams, "Band-structure engineering for low-threshold high-efficiency semiconductor lasers," *Electronics Letters*, vol. 22, no. 5, pp. 249–250, Feb. 1986.

[64] E. Yablonovitch and E. Kane, "Reduction of lasing threshold current density by the lowering of valence band effective mass," *Journal of Lightwave Technology*, vol. 4, no. 5, pp. 504–506, May 1986.

[65] A.R. Adams, M. Asada, Y. Suematsu, and S. Arai, "The temperature dependence of the efficiency and threshold current of $In_{1-x}Ga_xAs_yP_{1-y}$ lasers related to intervalence band absorption," *Japanese Journal of Applied Physics*, vol. 19, no. 10, pp. L621–L624, Oct. 1980.

[66] A. Chandola, R. Pino, and P.S. Dutta, "Below bandgap optical absorption in tellurium-doped GaSb," *Semiconductor Science and Technology*, vol. 20, no. 8, pp. 886–893, Jul. 2005.

[67] L. Shterengas, G. Belenky, G. Kipshidze, and T. Hosoda, "Room temperature operated 3.1 μm type-I GaSb-based diode lasers with 80 mW continuous-wave output power," *Applied Physics Letters*, vol. 92, no. 17, p. 171111, Apr. 2008.

[68] G. Belenky, L. Shterengas, G. Kipshidze, and T. Hosoda, "Type-I diode lasers for spectral region above 3 μm," *IEEE Journal of Selected Topics in Quantum Electronics*, vol. 17, no. 5, pp. 1426–1434, Sep. 2011.

[69] K. Vizbaras and M.-C. Amann, "Room-temperature 3.73 μm GaSb-based type-I quantum-well lasers with quinternary barriers," *Semiconductor Science and Technology*, vol. 27, no. 3, p. 032001, Jan. 2012.

[70] A.Y. Cho, "Film deposition by molecular-beam techniques," *Journal of Vacuum Science and Technology*, vol. 8, no. 5, S31–S38, Sep. 1971.

[71] A. Cho and J. Arthur, "Molecular beam epitaxy," *Progress in Solid State Chemistry*, vol. 10, pp. 157–191, Jan. 1975.

[72] J.R. Arthur, "Interaction of Ga and As_2 molecular beams with GaAs surfaces," *Journal of Applied Physics*, vol. 39, no. 8, pp. 4032–4034, Jul. 1968.

[73] J.R. Arthur and J.J. LePore, "GaAs, GaP, and $GaAs_xP_{1-x}$ epitaxial films grown by molecular beam deposition," *Journal of Vacuum Science and Technology*, vol. 6, no. 4, pp. 545–548, Jul. 1969.

[74] M.W. Wang, "Study of interface asymmetry in InAs–GaSb heterojunctions," *Journal of Vacuum Science & Technology B: Microelectronics and Nanometer Structures*, vol. 13, no. 4, p. 1689, Jul. 1995.

[75] Q. Xie, J.E.V. Nostrand, J.L. Brown, and C.E. Stutz, "Arsenic for antimony exchange on GaSb, its impacts on surface morphology, and interface structure," *Journal of Applied Physics*, vol. 86, no. 1, pp. 329–337, Jul. 1999.

[76] S. Subbanna, "Reflection high-energy electron diffraction oscillations during molecular-beam epitaxy growth of gallium antimonide, aluminum antimonide, and indium arsenide," *Journal of Vacuum Science & Technology B: Microelectronics and Nanometer Structures*, vol. 7, no. 2, p. 289, Mar. 1989.

[77] A. Bracker, M. Yang, B. Bennett, J. Culbertson, and W. Moore, "Surface reconstruction phase diagrams for InAs, AlSb, and GaSb," *Journal of Crystal Growth*, vol. 220, no. 4, pp. 384–392, Dec. 2000.

[78] J. Harris, B.A. Joyce, and P. Dobson, "Oscillations in the surface structure of sn-doped GaAs during growth by MBE," *Surface Science*, vol. 103, no. 1, pp. L90–L96, Feb. 1981.

[79] J.H. Neave, B.A. Joyce, P.J. Dobson, and N. Norton, "Dynamics of film growth of GaAs by MBE from RHEED observations," *Applied Physics A Solids and Surfaces*, vol. 31, no. 1, pp. 1–8, May 1983.

[80] B.F. Lewis, "Reflection high energy electron diffraction intensity behavior during homoepitaxial molecular beam epitaxy growth of GaAs and implications for growth kinetics and mechanisms," *Journal of Vacuum Science & Technology B: Microelectronics and Nanometer Structures*, vol. 3, no. 5, p. 1317, Sep. 1985.

[81] H.P. Nair, "MBE growth of GaSb-based alloys for mid-infrared semiconductor diode lasers," Ph.D. dissertation, The University of Texas at Austin, Austin, TX, May 2013.

[82] T.H. Gfroerer, "Photoluminescence in analysis of surfaces and interfaces," in *Encyclopedia of Analytical Chemistry*. American Cancer Society, 2006.

[83] R. Kudrawiec and J. Misiewicz, "Photoreflectance and contactless electroreflectance measurements of semiconductor structures by using bright and dark configurations," *Review of Scientific Instruments*, vol. 80, no. 9, p. 096103, Sep. 2009.

[84] R.N. Hall, G.E. Fenner, J.D. Kingsley, T.J. Soltys, and R.O. Carlson, "Coherent light emission from GaAs junctions," *Phys. Rev. Lett.*, vol. 9, pp. 366–368, 9 1962.

[85] M.I. Nathan, W.P. Dumke, G. Burns, F.H. Dill, and G. Lasher, "Stimulated emission of radiation from GaAs p-n junctions," *Applied Physics Letters*, vol. 1, no. 3, pp. 62–64, 1962.

[86] H. Kroemer, "A proposed class of hetero-junction injection lasers," *Proceedings of the IEEE*, vol. 51, no. 12, pp. 1782–1783, Dec. 1963.

[87] Z.I. Alferov and R.F. Kazarinov, "Semiconductor laser with electric pumping," Inventor's Certificate No. 181737 [in Russian], Application No. 950840, Mar. 30, 1963.

[88] Z.I. Alferov *et al.*, "Injection luminescence of epitaxial heterojunctions in the GaP-GaAs system," *Sov. Phys. Solid State*, vol. 9, p. 208, 1967.

[89] Z. Alferov, V. Andreev, V. Korolkov, E. Portnoi, and D. Tretyakov, "Coherent radiation of epitaxial heterojunction structures in the AlAs-GaAs system," *Sov. Phys. Semicond.*, vol. 2, pp. 1289–1291, Jan. 1969.

[90] J.P. van der Ziel, R. Dingle, R.C. Miller, W. Wiegmann, and W.A. Nordland, "Laser oscillation from quantum states in very thin GaAs–$Al_{0.2}Ga_{0.8}As$ multilayer structures," *Applied Physics Letters*, vol. 26, no. 8, pp. 463–465, Apr. 1975.

[91] W.T. Tsang, "Extremely low threshold (AlGa)As graded-index waveguide separate-confinement heterostructure lasers grown by molecular beam epitaxy," *Applied Physics Letters*, vol. 40, no. 3, pp. 217–219, Feb. 1982.

[92] A.R. Adams, "Strained-layer quantum-well lasers," *IEEE Journal of Selected Topics in Quantum Electronics*, vol. 17, no. 5, pp. 1364–1373, Sep. 2011.

[93] P.J.A. Thijs, L.F. Tiemeijer, P.I. Kuindersma, J.J.M. Binsma, and T. Van Dongen, "High-performance 1.5 μm wavelength InGaAs-InGaAsP strained quantum well lasers and amplifiers," *IEEE Journal of Quantum Electronics*, vol. 27, no. 6, pp. 1426–1439, 1991.

[94] L. Shterengas, G. Belenky, M.V. Kisin, and D. Donetsky, "High power 2.4 μm heavily strained type-I quantum well GaSb-based diode lasers with more than 1 W of continuous wave output power and a maximum power-conversion efficiency of 17.5%," *Applied Physics Letters*, vol. 90, no. 1, p. 011119, Jan. 2007.

[95] J. Chen *et al.*, "2.7-μm GaSb-based diode lasers with quinary waveguide," *IEEE Photonics Technology Letters*, vol. 21, no. 16, pp. 1112–1114, Aug. 2009.

[96] T. Hosoda, "GaSb-based type-I diode lasers operating at 3 μm and above," Ph.D. dissertation, Stony Brook University, Stony Brook, NY, USA, Dec. 2011.

[97] T. Lehnhardt, M. Hümmer, K. Rößner, M. Müller, S. Höfling, and A. Forchel, "Continuous wave single mode operation of GaInAsSb/GaSb quantum well lasers emitting beyond 3 μm," *Applied Physics Letters*, vol. 92, no. 18, p. 183508, Jun. 2008.

[98] M. Gladysiewicz, R. Kudrawiec, and M.S. Wartak, "Electronic band structure and material gain of III-V-Bi quantum wells grown on GaSb substrate and dedicated for mid-infrared spectral range," *Journal of Applied Physics*, vol. 119, no. 7, p. 075701, Feb. 2016.

[99] M. Grau, C. Lin, O. Dier, C. Lauer, and M.-C. Amann, "Room-temperature operation of 3.26 μm GaSb-based type-I lasers with quinternary AlGaInAsSb barriers," *Applied Physics Letters*, vol. 87, no. 24, p. 241104, Dec. 2005.

[100] T. Lehnhardt, A. Herrmann, M. Kamp, S. Hofling, L. Worschech, and A. Forchel, "Influence of GaSb and AlGaInAsSb as barrier material on ∼2.8-μm GaSb-based diode laser properties," *IEEE Photonics Technology Letters*, vol. 23, no. 6, pp. 371–373, Mar. 2011.

[101] H. Choi, G. Turner, and S. Eglash, "High-power GaInAsSb-AlGaAsSb multiple-quantum-well diode lasers emitting at 1.9 μm," *IEEE Photonics Technology Letters*, vol. 6, no. 1, pp. 7–9, Jan. 1994.

[102] D. Garbuzov, H. Lee, V. Khalfin, R. Martinelli, J. Connolly, and G. Belenky, "2.3-2.7-μm room temperature CW operation of InGaAsSb-AlGaAsSb broad waveguide SCH-QW diode lasers," *IEEE Photonics Technology Letters*, vol. 11, no. 7, pp. 794–796, Jul. 1999.

[103] J.G. Kim, L. Shterengas, R.U. Martinelli, and G.L. Belenky, "High-power room-temperature continuous wave operation of 2.7 and 2.8 μm In(Al)GaAsSb/GaSb diode lasers," *Applied Physics Letters*, vol. 83, no. 10, pp. 1926–1928, Sep. 2003.

[104] L. Shterengas, G. Belenky, T. Hosoda, G. Kipshidze, and S. Suchalkin, "Continuous wave operation of diode lasers at 3.36 μm at 12 °C," *Applied Physics Letters*, vol. 93, no. 1, p. 011103, Jul. 2008.

[105] T. Hosoda, G. Belenky, L. Shterengas, G. Kipshidze, and M.V. Kisin, "Continuous-wave room temperature operated 3.0 μm type I GaSb-based lasers with quinternary AlInGaAsSb barriers," *Applied Physics Letters*, vol. 92, no. 9, p. 091106, Mar. 2008.

[106] T. Hosoda, G. Kipshidze, L. Shterengas, and G. Belenky, "Diode lasers emitting near 3.44 μm in continuous-wave regime at 300K," *Electronics Letters*, vol. 46, no. 21, p. 1455, 2010.

[107] H.P. Nair, R. Salas, N.T. Sheehan, S.J. Maddox, and S.R. Bank, "3.4 μm diode lasers employing Al-free GaInAsSb/GaSb MQW active regions at 20 °C," *71st Device Research Conference*, IEEE, Jun. 2013.

[108] K. Vizbaras and M.-C. Amann, "3.6 µm GaSb-based type-I lasers with quinternary barriers, operating at room temperature," *Electronics Letters*, vol. 47, no. 17, p. 980, 2011.

[109] J.M. Moison, C. Guille, F. Houzay, F. Barthe, and M.V. Rompay, "Surface segregation of third-column atoms in group III-V arsenide compounds: ternary alloys and heterostructures," *Physical Review B*, vol. 40, no. 9, pp. 6149–6162, Sep. 1989.

[110] E. Tournié and K.H. Ploog, "Surfactant-mediated molecular beam epitaxy of strained layer semiconductor heterostructures," *Thin Solid Films*, vol. 231, no. 1-2, pp. 43–60, Aug. 1993.

[111] J. Massies and N. Grandjean, "Surfactant effect on the surface diffusion length in epitaxial growth," *Physical Review B*, vol. 48, no. 11, pp. 8502–8505, Sep. 1993.

[112] E. Tournié, N. Grandjean, A. Trampert, J. Massies, and K. Ploog, "Surfactant-mediated molecular-beam epitaxy of III–V strained-layer heterostructures," *Journal of Crystal Growth*, vol. 150, pp. 460–466, May 1995.

[113] M. Copel, M.C. Reuter, E. Kaxiras, and R.M. Tromp, "Surfactants in epitaxial growth," *Physical Review Letters*, vol. 63, no. 6, pp. 632–635, Aug. 1989.

[114] M. Copel, M.C. Reuter, M.H. Hoegen, and R.M. Tromp, "Influence of surfactants in Ge and Si epitaxy on Si(001)," *Physical Review B*, vol. 42, no. 18, pp. 11682–11689, Dec. 1990.

[115] H. Shimizu, K. Kumada, S. Uchiyama, and A. Kasukawa, "1.2 μm range GaInAs SQW lasers using Sb as surfactant," *Electronics Letters*, vol. 36, no. 16, p. 1379, 2000.

[116] X. Yang, M.J. Jurkovic, J.B. Heroux, and W.I. Wang, "Molecular beam epitaxial growth of InGaAsN:Sb/GaAs quantum wells for long-wavelength semiconductor lasers," *Applied Physics Letters*, vol. 75, no. 2, pp. 178–180, Jul. 1999.

[117] W. Ha *et al.*, "Long wavelength GaInNAsSb/GaNAsSb multiple quantum well lasers," *Electronics Letters*, vol. 38, no. 6, p. 277, 2002.

[118] V. Gambin *et al.*, "GaInNAsSb for 1.3-1.6-μm-long wavelength lasers grown by molecular beam epitaxy," *IEEE Journal of Selected Topics in Quantum Electronics*, vol. 8, no. 4, pp. 795–800, Jul. 2002.

[119] K. Volz *et al.*, "The role of Sb in the MBE growth of (GaIn)(NAsSb)," *Journal of Crystal Growth*, vol. 251, no. 1-4, pp. 360–366, Apr. 2003.

[120] S. Bank, M. Wistey, L. Goddard, H. Yuen, V. Lordi, and J. Harris, "Low-threshold continuous-wave 1.5-μm GaInNAsSb lasers grown on GaAs," *IEEE Journal of Quantum Electronics*, vol. 40, no. 6, pp. 656–664, Jun. 2004.

[121] S.R. Bank *et al.*, "Recent progress on 1.55-μm dilute-nitride lasers," *IEEE Journal of Quantum Electronics*, vol. 43, no. 9, pp. 773–785, Sep. 2007.

[122] J.S. Harris *et al.*, "Development of GaInNAsSb alloys: growth, band structure, optical properties and applications," *physica status solidi (b)*, vol. 244, no. 8, pp. 2707–2729, Aug. 2007.

[123] S. Tixier, M. Adamcyk, E. Young, J. Schmid, and T. Tiedje, "Surfactant enhanced growth of GaNAs and InGaNAs using bismuth," *Journal of Crystal Growth*, vol. 251, no. 1-4, pp. 449–454, Apr. 2003.

[124] G. Feng, K. Oe, and M. Yoshimoto, "Temperature dependence of Bi behavior in MBE growth of InGaAs/InP," *Journal of Crystal Growth*, vol. 301-302, pp. 121–124, Apr. 2007.

[125] G. Vardar, S.W. Paleg, M.V. Warren, M. Kang, S. Jeon, and R.S. Goldman, "Mechanisms of droplet formation and Bi incorporation during molecular beam epitaxy of GaAsBi," *Applied Physics Letters*, vol. 102, no. 4, p. 042106, Jan. 2013.

[126] K. Sakamoto, K. Kyoya, K. Miki, H. Matsuhata, and T. Sakamoto, "Which surfactant shall we choose for the heteroepitaxy of Ge/Si(001)? —Bi as a surfactant with small self-incorporation—," *Japanese Journal of Applied Physics*, vol. 32, no. Part 2, No. 2A, pp. L204–L206, Feb. 1993.

[127] R. Salas *et al.*, "Surfactant-assisted growth and properties of rare-earth arsenide InGaAs nanocomposites for terahertz generation," *Applied Physics Letters*, vol. 108, no. 18, p. 182102, May 2016.

[128] E. Young, S. Tixier, and T. Tiedje, "Bismuth surfactant growth of the dilute nitride GaN_xAs_{1-x}," *Journal of Crystal Growth*, vol. 279, no. 3-4, pp. 316–320, Jun. 2005.

[129] M.R. Pillai, S.-S. Kim, S.T. Ho, and S.A. Barnett, "Growth of $In_xGa_{1-x}As$/GaAs heterostructures using Bi as a surfactant," *Journal of Vacuum Science & Technology B: Microelectronics and Nanometer Structures*, vol. 18, no. 3, pp. 1232–1236, Mar. 2000.

[130] J. Matthews and A. Blakeslee, "Defects in epitaxial multilayers: I. misfit dislocations," *Journal of Crystal Growth*, vol. 27, pp. 118–125, Dec. 1974.

[131] J. Matthews and A. Blakeslee, "Defects in epitaxial multilayers: II. dislocation pile-ups, threading dislocations, slip lines and cracks," *Journal of Crystal Growth*, vol. 29, no. 3, pp. 273–280, Jul. 1975.

[132] J. Matthews and A. Blakeslee, "Defects in epitaxial multilayers: III. preparation of almost perfect multilayers," *Journal of Crystal Growth*, vol. 32, no. 2, pp. 265–273, Feb. 1976.

[133] H. Li and Z.M. Wang, Eds., *Bismuth-Containing Compounds*. Springer New York, 2013.

[134] M. Henini, *Dilute Nitride Semiconductors*. Elsevier, 2005.

[135] J. Yoshida, T. Kita, O. Wada, and K. Oe, "Temperature dependence of $GaAs_{1-x}Bi_x$ band gap studied by photoreflectance spectroscopy," *Japanese Journal of Applied Physics*, vol. 42, no. Part 1, No. 2A, pp. 371–374, Feb. 2003.

[136] R.N. Kini, L. Bhusal, A.J. Ptak, R. France, and A. Mascarenhas, "Electron hall mobility in GaAsBi," *Journal of Applied Physics*, vol. 106, no. 4, p. 043705, Aug. 2009.

[137] D.G. Cooke, F.A. Hegmann, E.C. Young, and T. Tiedje, "Electron mobility in dilute GaAs bismide and nitride alloys measured by time-resolved terahertz spectroscopy," *Applied Physics Letters*, vol. 89, no. 12, p. 122103, Sep. 2006.

[138] J. Wu, W. Shan, and W. Walukiewicz, "Band anticrossing in highly mismatched III-V semiconductor alloys," *Semiconductor Science and Technology*, vol. 17, no. 8, pp. 860–869, Jul. 2002.

[139] Y. Zhang, A. Mascarenhas, H.P. Xin, and C.W. Tu, "Scaling of band-gap reduction in heavily nitrogen doped GaAs," *Physical Review B*, vol. 63, no. 16 Apr. 2001.

[140] R.N. Kini, A. Mascarenhas, R. France, and A.J. Ptak, "Low temperature photoluminescence from dilute bismides," *Journal of Applied Physics*, vol. 104, no. 11, p. 113534, Dec. 2008.

[141] K. Oe, S. Ando, and K. Sugiyama, "$InSb_{1-x}Bi_x$ films grown by molecular beam epitaxy," *Japanese Journal of Applied Physics*, vol. 20, no. 4, pp. L303–L306, Apr. 2013.

[142] K. Alberi *et al.*, "Valence-band anticrossing in mismatched III-V semiconductor alloys," *Physical Review B*, vol. 75, no. 4 Jan. 2007.

[143] K. Alberi, O.D. Dubon, W. Walukiewicz, K.M. Yu, K. Bertulis, and A. Krotkus, "Valence band anticrossing in $GaBi_xAs_{1-x}$," *Applied Physics Letters*, vol. 91, no. 5, p. 051909, Jul. 2007.

[144] I.P. Marko and S.J. Sweeney, "Progress toward III–V bismide alloys for near- and midinfrared laser diodes," *IEEE Journal of Selected Topics in Quantum Electronics*, vol. 23, no. 6, pp. 1–12, Nov. 2017.

[145] Z. Batool, K. Hild, T.J.C. Hosea, X. Lu, T. Tiedje, and S.J. Sweeney, "The electronic band structure of GaBiAs/GaAs layers: influence of strain and band anticrossing," *Journal of Applied Physics*, vol. 111, no. 11, p. 113108, Jun. 2012.

[146] I.P. Marko *et al.*, "Temperature and Bi-concentration dependence of the bandgap and spin-orbit splitting in InGaBiAs/InP semiconductors for mid-infrared applications," *Applied Physics Letters*, vol. 101, no. 22, p. 221108, Nov. 2012.

[147] M.K. Rajpalke *et al.*, "Growth and properties of GaSbBi alloys," *Applied Physics Letters*, vol. 103, no. 14, p. 142106, Sep. 2013.

[148] M.K. Rajpalke *et al.*, "High Bi content GaSbBi alloys," *Journal of Applied Physics*, vol. 116, no. 4, p. 043511, Jul. 2014.

[149] O. Delorme, L. Cerutti, E. Tournié, and J.-B. Rodriguez, "Molecular beam epitaxy and characterization of high Bi content GaSbBi alloys," *Journal of Crystal Growth*, vol. 477, pp. 144–148, Nov. 2017.

[150] O. Delorme *et al.*, "GaSbBi/GaSb quantum well laser diodes," *Applied Physics Letters*, vol. 110, no. 22, p. 222106, May 2017.

[151] M.K. Rajpalke *et al.*, "Bi-induced band gap reduction in epitaxial InSbBi alloys," *Applied Physics Letters*, vol. 105, no. 21, p. 212101, Nov. 2014.

[152] O. Delorme, L. Cerutti, E. Luna, A. Trampert, E. Tournié, and J.-B. Rodriguez, "Molecular-beam epitaxy of GaInSbBi alloys," *Journal of Applied Physics*, vol. 126, no. 15, p. 155304, Oct. 2019.

[153] S.D. Sifferman *et al.*, "Dilute-bismide alloys for GaSb-based mid-infrared semiconductor lasers," *Conference on Lasers and Electro-Optics*, OSA, 2018.

[154] M. Ferhat and A. Zaoui, "Structural and electronic properties of III-V bismuth compounds," *Physical Review B*, vol. 73, no. 11 Mar. 2006.

[155] R. Kudrawiec *et al.*, "Experimental and theoretical studies of band gap alignment in $GaAs_{1-x}Bi_x$/GaAs quantum wells," *Journal of Applied Physics*, vol. 116, no. 23, p. 233508, Dec. 2014.

[156] M. Yano, H. Yokose, Y. Iwai, and M. Inoue, "Surface reaction of III–V compound semiconductors irradiated by As and Sb molecular beams," *Journal of Crystal Growth*, vol. 111, no. 1-4, pp. 609–613, May 1991.

[157] M. Losurdo, P. Capezzuto, G. Bruno, A.S. Brown, T. Brown, and G. May, "Fundamental reactions controlling anion exchange during mixed anion heterojunction formation: chemistry of As-for-Sb and Sb-for-As exchange reactions," *Journal of Applied Physics*, vol. 100, no. 1, p. 013531, Jul. 2006.